

BEARINGS-ONLY QUADROTOR GUIDANCE IN GAP TRAVERSAL SCENARIOS

A THESIS
SUBMITTED FOR THE DEGREE OF
Doctor of Philosophy
IN THE FACULTY OF ENGINEERING

by
Midhun E K



Department of Aerospace Engineering
Indian Institute of Science
Bengaluru-560012, India
March 2024

© Midhun E K
March 2024
All rights reserved

*Dedicated to
My Beloved Family, Friends and Teachers*

DECLARATION

I, Midhun E K, declare that the thesis entitled "**Bearings-Only Quadro rotor Guidance in Gap Traversal Scenarios**" submitted by me for the Ph.D. degree of the Indian Institute of Science did not form the subject matter of any other thesis submitted by me for any outside degree. The work incorporated in this thesis is original and carried out by me at the Indian Institute of Science, Bengaluru, India.

Bengaluru 560012

March 2024



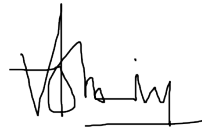
Midhun E K

Signature of the Student:



.....
Midhun E K
Department of Aerospace Engineering
Indian Institute of Science, Bengaluru

Signature of the Thesis Supervisor:



.....
Ashwini Ratnoo
Associate Professor
Department of Aerospace Engineering
Indian Institute of Science, Bengaluru

Acknowledgment

I would like to express my sincere gratitude to Prof. Ashwini Ratnoo, my supervisor, for his invaluable guidance, unwavering support, helpful discussions, and insightful feedback. He always helped me to find the correct direction towards my research topics and also provided the atmosphere and facilities for an ideal work environment.

I am sincerely thankful to Prof. Debasish Ghose and Prof. Suresh Sundaram for their valuable advice and continuous support throughout the academic journey. I am also grateful to Professors Dr. Vittal Rao, Dr. G R Jayanth, Dr. Raghu Krishnapuram, and Dr. Joseph Mathew for their lectures and contributions during the coursework.

My heartfelt appreciation goes to my lab-mates in the Autonomous Vehicles Laboratory, Amit Shivam, Gautam Kumar, Ravi Khandelwal, and Mohit Malhotra, for their assistance, encouragement, and valuable suggestions. I really appreciate their valuable advice and insightful discussions. I express my gratitude to Dr. Vinay Reddy for his support during experimental flight trials in the MoCap laboratory.

I express my thanks to Ms. Sreeja for her help on several academic official works and to Ms. Lalitha for providing the arrangements for our weekly research presentations. I am indebted to the scholarship department of IISc Bengaluru for their financial assistance, enabling me to pursue my academic endeavors.

I am thankful to my friends Josy John, Meenu Jayamohan, Neethu M, Litson P Thambi, and Sparsh Yadav for their unwavering support, love, and companionship throughout this journey. I want to thank my sister and parents for supporting me throughout my Ph.D. journey and throughout my life. Special gratitude is extended to Dr. K Sundareswaran for his invaluable advice and care throughout my career. Lastly, I express my gratitude to all those who directly

or indirectly contributed to this thesis. Their support and encouragement have been invaluable, and I am deeply grateful for their contributions.

Publications from the Thesis

Journals

1. E. K. Midhun and A. Ratnoo, "Local Information-based Guidance for Lane Transition in Air Corridors," *Journal of Guidance, Control, and Dynamics*, Vol. 47, No. 3, pp. 564-572, 2024. <https://doi.org/10.2514/1.G007752>
2. E. K. Midhun and A. Ratnoo, "Gap Traversal Guidance Using Bearing Information," *Journal of Guidance, Control, and Dynamics*, Vol. 45, No. 12, pp. 2360-2368, 2022. <https://doi.org/10.2514/1.G006898>
3. E. K. Midhun and A. Ratnoo, "Quadrotor Guidance for Window Traversal: A Bearings-Only Approach," (Manuscript under preparation).

Conferences

1. E. K. Midhun and A. Ratnoo, "Bearing Information-based Trajectory Planning for Window Traversal," in *2023 9th International Conference on Control, Decision and Information Technologies (CoDIT)*, pp. 1291-1295, 2023. <https://doi.org/10.1109/CoDIT58514.2023.10284194>
2. E. K. Midhun and A. Ratnoo, "Quadrotor Guidance for Traversal Through Moving Gaps Using Bearing-Only Information", in *AIAA Scitech 2022 Forum*, AIAA Paper 2022-0539, 2022. <https://doi.org/10.2514/6.2022-0539>
3. E. K. Midhun and A. Ratnoo, "Safe Traversal Guidance for Quadrotors Using Gap Bearing Information", in *2021 International Conference on Unmanned Aircraft Systems (ICUAS)*, pp. 482-487, 2021. <https://doi.org/10.1109/ICUAS51884.2021.9476785>

Abstract

In autonomous missions, quadrotors are often required to safely fly through gaps or openings. Designing traversal guidance strategies becomes crucial in such scenarios, especially when the quadrotor relies on the information obtained through onboard sensors. Lightweight and passive vision-based sensors can readily provide bearing information of the gaps using image features. This thesis addresses the quadrotor guidance problem of traversing gaps using only the relative bearing information. Specifically, the work considers three scenarios: planar flight through gaps, window traversal, and moving gap traversal for lane transition in air corridors.

The first part of the thesis presents a planar gap traversal guidance law using bearings-only information. The main contribution in this part is a novel guidance method governing quadrotor heading direction using bearing information of the gap opening. The proposed heading direction is designed using an elliptic shaping angle derived from the angular bisector orientation of the gap-bearing angles. The stability of the resulting closed-loop kinematics is ascertained using Lyapunov's direct method. Additionally, a phase plane analysis is carried out to visualize the safe traversal characteristics of the proposed method considering all possible initial conditions around the gap. Combined with a tracking controller, the proposed guidance strategy is applied to a six-degree-of-freedom (6-DOF) quadrotor model, ensuring convergence towards the prescribed trajectory. The effectiveness of the proposed guidance method is validated with numerical simulations considering several initial conditions, noisy bearing measurements, and dynamic vehicle constraints.

Moving beyond planar scenarios, a three-dimensional window traversal problem is considered in the next part of the thesis and a guidance solution is proposed using bearing information of window extremities. The guidance logic governs the commanded flight path angle and

heading angle of the vehicle. Again, these commands comprise an angular bisector component with a shaping angle, facilitating traversal along a direction normal to the window plane and passing through the centroid. A detailed stability analysis ascertains the convergence of vehicle trajectories to the desired traversal path. Simulation studies consider a 6-DOF quadrotor model, dynamic attitude constraints, and noise in bearing information. The robustness of the proposed method is demonstrated through a Monte-Carlo simulation study, considering various initial conditions and noisy measurements.

Next, a new lane transition guidance method for a quadrotor flying in an air corridor system is introduced. Utilizing the bearing information of the neighboring vehicles, the guidance method directs the quadrotor for a safe transition between two lanes. Comprising three sequential guidance phases, the method includes discerning guidance for determining neighboring vehicle velocity, longitudinal guidance to identify suitable gaps in the destination lane, and transit guidance to maneuver the quadrotor into the desired gap. A detailed analysis deduces, in closed-form, the time duration for each of the three guidance phases. Additionally, local asymptotic stability is ascertained for the proposed guidance phases. Simulation results and Monte-Carlo studies demonstrate the feasibility, effectiveness, and robustness of the proposed method towards safe autonomous lane transition.

Overall, the proposed guidance methods present simple, easily computable and closed-form analytic guidance inputs using only the passive bearing information. Further, deterministic performance guarantees provide a sound theoretical foundation for the novel guidance solutions. The thesis also includes representative experimental studies using an indoor motion capture system and Crazyflie quadrotor platform.

Contents

Acknowledgment	vii
Publications from the Thesis	ix
Abstract	xi
Contents	xiii
List of Figures	xvii
List of Tables	xxi
1 Introduction	1
1.1 Background	2
1.1.1 Bearing information-based guidance methods	2
1.1.2 Quadrotor guidance for flying through gaps	2
1.1.3 Lane transition in air corridors	4
1.2 Contribution and Organization of the Thesis	6
2 Planar Guidance for Flying Through Gaps	9
2.1 Problem Description	9
2.2 Proposed Guidance Method	11
2.3 Stability Characteristics	13
2.3.1 Phase portrait analysis	16
2.4 Quadrotor Dynamic Model and Control	17

2.4.1	Quadrotor dynamic model	17
2.4.2	Tracking control	20
2.5	Simulation Results	22
2.5.1	Case 1. Sample scenario with noise free gap bearing angles	24
2.5.2	Case 2. Effect of noise in bearing angle information	24
2.5.3	Case 3. Various initial conditions and noisy measurements	25
2.6	Summary	28
3	Three-Dimensional Guidance for Window Traversal	31
3.1	Problem Description	31
3.2	Proposed Guidance Method	32
3.2.1	Desired flight path angle	34
3.2.2	Desired heading angle	38
3.3	Stability Characteristics	39
3.3.1	Phase plane analysis	46
3.4	Trajectory Generation and Control	49
3.5	Qualitative Comparison with Existing Works	50
3.6	Numerical Simulation Results	52
3.6.1	Case 1. Sample window traversal scenario with noise-free bearing in- formation	52
3.6.2	Case 2. Effect of noise in bearing information	53
3.6.3	Case 3: Various initial conditions and noisy measurements	56
3.7	Summary	59
4	Guidance Framework for Lane Transition in Air Corridors	61
4.1	Problem Formulation	61
4.2	Proposed Lane Transition Guidance Method	62
4.2.1	Discerning guidance phase	63
4.2.2	Longitudinal guidance phase	66

4.2.3	Transit guidance phase	69
4.2.4	Discussion	72
4.3	Guided Trajectory Generation and Control	73
4.4	Numerical Simulation Results	75
4.4.1	Case I: Sample lane transition scenario with noise free bearing infor- mation	76
4.4.2	Case 2. Effect of noise in bearing information	78
4.5	Summary	79
5	Experimental Results	81
5.1	Experimental Setup	82
5.1.1	Crazyflie 2.0 Quadrotor	82
5.1.2	Motion Capture System	83
5.1.3	Command and Communication System	85
5.1.4	Guidance and Control Architecture	88
5.2	Flight Experiment Results	89
5.2.1	Gap Traversal Guidance Method	89
5.2.2	Guidance Method for Window Traversal	93
5.3	Summary	97
6	Conclusions and Future Work	99
	Bibliography	103

List of Figures

2.1	Quadrotor approaching a gap	10
2.2	Elliptic shaping angle profile, $\frac{\theta_1+\theta_2}{2} \in [-\pi, \pi)$	11
2.3	Instantaneous desired heading along the guided trajectory	12
2.4	Instantaneous geometry	14
2.5	Phase portrait in θ_1 - θ_2 plane	17
2.6	Coordinate frames and forces acting on the vehicle.	18
2.7	Guidance and tracking control architecture.	20
2.8	Results for Case 1.	23
2.9	Velocity and altitude response for Case 1.	25
2.10	Results for Case 2.	26
2.11	Results for Case 3.	27
3.1	Quadrotor approaching a window.	32
3.2	Relative geometry between quadrotor and E_i	33
3.3	Elliptic shaping angle profile for γ_{des}	35
3.4	Instantaneous desired flight path angle along the guided trajectory	37
3.5	Elliptic shaping angle profile for χ_{des}	39
3.6	Instantaneous geometry of quadrotor moving towards the window	41
3.7	Relative geometries with respect to the window extremities	43
3.8	Phase plane analysis in $\alpha_1 - \alpha_4$ and $\beta_1 - \beta_2$ planes	47
3.9	Phase plane analysis in $\alpha_2 - \alpha_3$ and $\beta_4 - \beta_3$ planes.	48
3.10	Guided trajectory generation and control architecture	49

3.11	Quadrotor trajectory of Case 1	53
3.12	Results for Case 1	54
3.13	Results for Case 1	55
3.14	Quadrotor trajectory for Case 2	56
3.15	Results for Case 2	57
3.16	Quadrotor trajectories of Case 3	58
4.1	Lane transition scenario in an air corridor	62
4.2	Instantaneous geometry.	63
4.3	An instantaneous geometry during the longitudinal guidance phase.	66
4.4	Instantaneous geometry during transit phase	70
4.5	Control architecture.	74
4.6	Results for Case 1.	77
4.7	Attitude angles and altitude response for Case 1.	78
5.1	System architecture	81
5.2	Crazyflie 2.0 quadrotor	82
5.3	Room specification and camera placement	84
5.4	OptiTrack Prime-13 camera and marker	84
5.5	Visualization of rigid bodies on Motive software interface	86
5.6	ROS communication with various systems	87
5.7	Crazyradio	87
5.8	Simulink diagram	88
5.9	Crazyflie maneuvering towards the gap	90
5.10	Top view of the Crazyflie hovering at commencing waypoint and the gap . . .	90
5.11	Crazyflie trajectory	91
5.12	Top view of Crazyflie trajectory	91
5.13	Trajectory components	92
5.14	Angles for guidance computation	93
5.15	Crazyflie maneuvering towards the window	94

5.16	Crazyflie trajectory	95
5.17	Trajectory components	95
5.18	Angles for guidance computation	96

List of Tables

2.1	Initial conditions for Case 3.	28
3.1	Qualitative comparison study	51
3.2	Statistical results of Case 3	58
4.1	Effect of noise in bearing information	79

Chapter 1

Introduction

With autonomous capabilities, small size, maneuver agility, and low cost, quadrotor Unmanned Aerial Vehicles (UAVs) are increasingly used for a wide range of applications. These applications include logistics, aerial photography, surveillance, agriculture, inspection, and rescue in densely populated areas [1]. To accomplish these missions, quadrotors often need to traverse through gaps or openings when moving in cluttered environments characterized by obstacles, physical boundaries, and confining spaces [2]. Feasible guidance methods are desired to execute gap traversal in such scenarios. While designing such guidance logic, it is important to consider the nature of local information available through the onboard sensors.

Due to the inherent payload limitations of flying vehicles, a popular choice is to use passive, lightweight, and inexpensive vision-based sensors. Vision-based quadrotor systems have gained significant attention due to their potential applications in obstacle avoidance, target tracking, autonomous landing, and drone racing competitions [3–6]. Vision-based sensors can readily provide bearing or direction information of the gap boundaries, which is vital for developing traversal guidance solutions. For obtaining bearing information, vision sensors use edge detection and corner detection algorithms on image features [7]. Accordingly, traversal guidance algorithms are desired to be based on bearings-only information of the gap. This forms the basic motivation for the research carried out in this work. The thesis addresses three specific problem scenarios: planar flight through gaps, three-dimensional window traversal, and a moving gap traversal logic for lane transition in air corridor systems.

1.1 Background

This section first reviews the developments in bearing information-based guidance design. This is followed by a review of the existing literature on quadrotor gap traversal guidance methods.

1.1.1 Bearing information-based guidance methods

Conventionally, line-of-sight bearing information-based guidance laws have been widely researched in the context of interceptor-target engagement scenarios [8–12]. Therein, the typical guidance objective is to intercept a stationary or a moving target. Bearings-only guidance laws have received some attention in the context of small UAVs. In [13, 14], the authors introduce a proportional navigation-based guidance method for UAV collision avoidance. Therein, line-of-sight bearing angle rates obtained from a monocular vision sensor are used to identify collision threats. Further, guided maneuvers increase the magnitude of the line-of-sight rate to avoid collisions. In [15], the authors present a guidance strategy to maneuver a vehicle to any desired goal position inside a triangular region using line-of-sight bearing information from three noncollinear stationary beacons. That guidance method is extended in Ref. [16] to make the entire plane reachable by the vehicle. In [17], a gain adaptive proportional navigation guidance method is developed based on relative bearing information of multiple beacons placed along a path. Bearing-based formation control of quadrotors is addressed in [18, 19], wherein inter-agent bearing information is used for achieving desired formation geometry of quadrotors. Another work considers a pursuer quadrotor using a helical trajectory for following a target quadrotor by maintaining a specified relative distance [20]. That work utilizes three-dimensional bearing measurements of the target quadrotor to estimate its position and velocity. These measurements are resolved as elevation and azimuth angles, which are subsequently used for controlling vehicle motion through lateral acceleration and longitudinal acceleration guidance commands.

1.1.2 Quadrotor guidance for flying through gaps

Several methods have discussed guidance of a quadrotor flying through gaps which are characterized by stationary physical boundaries. In doing so, the quadrotor must maintain a safe

distance from the gap boundaries. In [21], the authors develop a sequence of desired trajectories and associated controllers that guide a quadrotor to a goal position by passing through a stationary gap. The sequence of trajectories include hovering to a desired starting position, a three-dimensional trajectory through the window, and finally a hover approach to the desired goal position. The three-dimensional trajectory and velocity components are computed with backward integration of equation of motion considering known final goal point and arrival time. Reference [22] proposes a traversal algorithm to generate optimal trajectories passing through a series of waypoints, guaranteeing safe traversal through a predetermined gap. The quadrotor trajectory therein is represented by piecewise time-parameterized polynomials, the coefficients of which are determined by the optimizing integral of the squared norm of the snap (second derivative of acceleration). A four-parameter logistic curve-based safe trajectory method is proposed in [23, 24] for three-dimensional traversal through a window. The quadrotor trajectories are represented by a four-parameter logistic time-parameterized polynomial, where computation of six coefficients is needed for defining the instantaneous desired position in three-dimensional space. It is noteworthy that, Refs. [21–24] rely on prior known information about the dimensions of the gap in the world frame, which may not be available in all realistic scenarios.

Based specifically on vision-based guidance, several studies discuss quadrotor gap traversal problems [25–31]. In [25], the authors address the problem of quadrotor traversal through a stationary window using data obtained from a vision-based onboard sensor and an inertial measurement unit. The trajectory is generated in a fashion similar to the minimum snap approach in [22]. The position and orientation of the window with respect to the quadrotor’s starting location are assumed to be known apriori. Additionally, the methods in [21–25] generate the complete traversal trajectory at once with inflexibility of using revised or updated information of the gap. With such an approach, errors in gap information can significantly affect the safety of the proposed trajectory. Reference [26] considers quadrotor position profile as a quadratic function of time for passing through the geometric center of a gap. The geometric center of the gap is computed using feature points from the image and additional image depth information. The traversal trajectory maximizes the distance between the quadrotor

and the gap edges.

References [27, 28] rely on complete gap-image information-based trajectory generation, requiring the original complete image of the window to be available beforehand. A polynomial trajectory generation in terms of invariant features defined in a image space is considered in [27] for achieving the location where the original image is taken. That work minimizes the snap in translation between the camera image and the reference image. Therein, the centroid of all detected image feature points is kept in the middle of the sensor field-of-view by controlling the heading angle of the vehicle. Upon reaching the location where the original image is taken, a gap traversal trajectory is generated similar to the one in [26]. Using a model predictive control framework for quadrotor guidance, window traversal is discussed in [28]. That work utilizes an image matching algorithm [29] to identify the target window within the current image. It is noteworthy that, the methods [27, 28] require depth information of the four window extremities by decomposition of homography matrix, leading to higher computational demand and possible loss of information.

In the context of quadrotor racing missions, Refs. [30, 31] present learning-based solutions for traversal guidance. In [30], a convolution network is used to estimate the gap pose, and the quadrotor trajectory is generated by interpolating two waypoints—one prior to the gap and the other beyond it. Another study [31] utilizes convolution neural network to estimate the gap center and a guidance law that uses the line-of-sight bearing angle of the gap center for traversal. Learning-based methods often require a large amount of data for training. The performance of the traversal model is heavily reliant on the quantity and quality of the training data, which may not be readily available in many possible scenarios. Further, learning methods can be computationally expensive during training and deployment, and they may lack safety and performance guarantees.

1.1.3 Lane transition in air corridors

Unmanned Aircraft Systems Traffic Management (UTM) is envisaged to support potentially thousands of Unmanned Aerial Vehicles flying safely in prescribed airspace. Utilization of designated airspace is a key component in effective implementation of UTM, which significantly

influence the airspace safety, efficiency, and capacity [32]. Air corridor is a robust framework for providing safe, structured, and collision-free paths for quadrotors in available airspace [33–36]. These corridors use geofencing by creating virtual boundaries and partitioning the airspace into lanes, which enables efficient and safe movement of multiple quadrotors [37]. Feasible guidance methods are desired to execute overtaking and lane-changing maneuvers in such corridors.

Lane-changing guidance can be viewed as a form of gap traversal guidance within multi-lane air corridor systems. Lane-changing involves finding a suitable dynamic gap formed by the vehicles in the adjacent lane and traversing into it while ensuring a smooth and collision-free transition. It is important to consider the reliable information available for designing such a guidance strategy. Vision-based sensors provide bearing or direction information of neighboring vehicles around the ego vehicle, and it is desired that guidance methods be designed utilizing this local bearing information.

Autonomous lane-changing is widely discussed in the context of ground vehicles [38]. Typically a suitable geometric interpolation function is utilized to generate a smooth trajectory connecting two lanes. These include Bézier curve [39, 40], four-parameter logistic curve [41, 42], polynomial variation [43], sinusoidal function [44], and sigmoid function [45]. The ground-based lane-changing logic used in [45] is extended for quadrotor traversal through consecutive window gaps that are placed along two lanes [46]. Reference [46] assumes complete position information of the windows to be known prior to the execution of the quadrotor maneuver. The lane-changing methods in [39–46] use the relative position information of the neighboring vehicles or slots, which may not be readily available from a monocular vision sensor.

There is a scarcity of literature addressing the lane changing framework within air corridors. A lane-changing algorithm in an air corridor system is introduced in [47], where inter-UAV distance information and the waypoint information are assumed to be known for generating collision-free lane transition trajectory using Bézier or B-spline curves. The lane-changing problem in [47] is further extended to address conflict-free traversal scenarios for quadrotors at lane intersections within air corridors in [48]. Here, quadrotors use a pure pursuit guidance

law for the desired traversal. The lane transition trajectory generation requires line-of-sight information with respect to the endpoint within the destination lane and the inter-UAV distance information. Methods in [47, 48] rely on the inter-UAV distances and the position information of desired traversal points in the destination lane. In contrast to these methods, this thesis focuses on developing lane transition guidance method based on bearings-only information of neighboring vehicles.

1.2 Contribution and Organization of the Thesis

This section presents the major contributions and organization of the thesis.

Chapter 2 presents a planar gap traversal guidance law using bearings-only information. The main contribution of this work is a novel guidance method governing quadrotor heading direction using bearing information of the gap opening. The proposed heading direction is designed using an elliptic shaping angle derived from the angular bisector orientation of the gap-bearing angles. The stability of the proposed guidance law is analyzed using Lyapunov's direct method. Additionally, a phase plane analysis is carried out to emphasize the safe traversal characteristics of the proposed method, considering all possible initial conditions around the gap. Realistic simulation results considering six-degree-of-freedom quadrotor model establish the effectiveness of the proposed approach.

Chapter 3 further develops the guidance method introduced in Chapter 2 a three-dimensional window traversal scenario. Using three-dimensional bearing angles of the window extremities, a desired flight path angle and a modified version of desired heading angle are introduced. Stability analysis of the resulting kinematics establishes asymptotic convergence of quadrotor trajectories to lateral traversal through the window centroid. A phase plane analysis presents a complete description of state variation spanning entire domain of interest. Furthermore, a detailed qualitative comparison study with existing methods is carried out to show superiority of the guidance methods introduced in Chapter 2 and Chapter 3. Realistic simulation studies and Monte-Carlo results validate the effectiveness, accuracy, and robustness of the proposed guidance algorithm.

Chapter 4 introduces a guidance strategy for lane transition in air corridors. The main

contribution of this work is a lane transition guidance method that governs quadrotor longitudinal and lateral motion using the bearing information of the neighboring vehicles in the destination lane. A three-phased guidance method is proposed: a discerning guidance phase for determining velocity of the neighboring vehicles, a longitudinal guidance phase for identifying appropriate gaps in the destination lane, and a transit guidance phase for maneuvering to the desired gap. The vehicle is shown to asymptotically attain desired speed during the discerning guidance phase, and the preferred bearing orientation for identifying gaps in the subsequent longitudinal guidance phase. A purely lateral maneuver in the last phase guides the vehicle to the desired location in the destination lane. Further, closed-form analytic expressions for the time duration of the three guidance phases are derived. Simulation studies highlight the performance of the proposed lane transition method as implemented on a six-degree-of-freedom quadrotor model with dynamic limits on attitude angles and uncertainty in sensor information.

Chapter 5 presents some flight experimental validation results for the guidance methods presented in Chapters 2 and 3.

Chapter 6 concludes the thesis and provides directions for the future research.

Chapter 2

Planar Guidance for Flying Through Gaps

This chapter introduces a guidance method for quadrotor traversal through a gap opening between two obstacles. A bearing-only information-based quadrotor heading guidance command is proposed and analyzed. Stability characteristics and a phase plane analysis of resulting engagement kinematics are presented. The chapter also discusses the quadrotor dynamic model and its guidance and control architecture. Extensive simulation case studies are presented to show the effectiveness of the proposed guidance method.

2.1 Problem Description

Consider a point-object quadrotor vehicle flying through two stationary obstacles in a two-dimensional (2-D) space, as depicted in Fig. 2.1. The objective is the safe quadrotor traversal through the gap between stationary obstacles considering the bearing information of the obstacle edges E_1 and E_2 , which are θ_1 and θ_2 , respectively. A fixed frame of reference is considered without loss of generality with its X -axis parallel to the line joining the edges E_1 and E_2 . Let $[x(t), y(t)]^T$ represent the quadrotor's position at any time t . The kinematic equations of vehicle motion can be expressed as

$$\dot{x}(t) = V \cos \chi(t) \tag{2.1}$$

$$\dot{y}(t) = V \sin \chi(t) \tag{2.2}$$

Here, V and χ represent quadrotor speed, and heading angle, respectively. The distance of

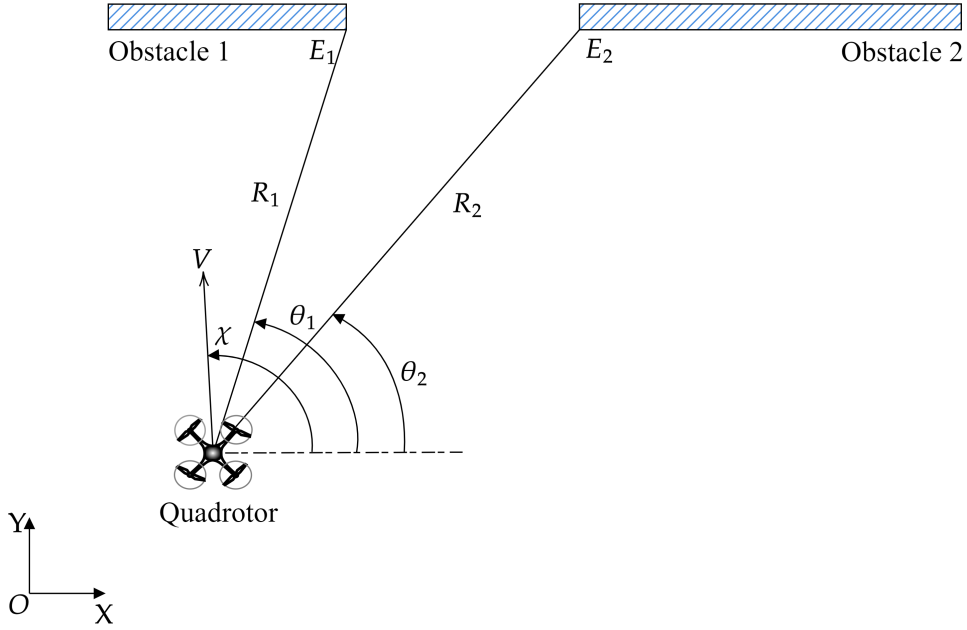


Figure 2.1: Quadrotor approaching a gap

separation between quadrotor vehicle and gap extremities is referred to as line-of-sight separation. Here, R_1 and R_2 indicate line-of-sight separation of vehicle from E_1 and E_2 , respectively. The angular orientation of line-of-sight with respect to a fixed reference frame defines the line-of-sight or the bearing angle. Accordingly, θ_1 and θ_2 are line-of-sight angles with respect to E_1 and E_2 , respectively.

The relative motion between the vehicle and the gap can be described by the following equation.

$$\dot{R}_1 = -V \cos(\chi - \theta_1) \quad (2.3)$$

$$R_1 \dot{\theta}_1 = -V \sin(\chi - \theta_1) \quad (2.4)$$

$$\dot{R}_2 = -V \cos(\chi - \theta_2) \quad (2.5)$$

$$R_2 \dot{\theta}_2 = -V \sin(\chi - \theta_2) \quad (2.6)$$

The guidance objective here is safe traversal through the gap between the obstacles using desired heading angle as the guidance command input, that is, to achieve

$$\theta_1 - \theta_2 = \pm 180 \text{ deg. with } R_1, R_2 > 0 \quad (2.7)$$

The considered bearing information can be potentially obtained using gap border or edge detection algorithms [26, 49]. Further, using projection of the edges in the image plane the three-dimensional bearing information of the gap can be obtained and subsequently resolved in horizontal and vertical planes [14].

2.2 Proposed Guidance Method

The proposed guidance method is based on the idea of moving the quadrotor vehicle through the gap laterally while keeping a safe clearance from the obstacle edges. With θ_1 and θ_2 as the edge bearing angles, desired heading angle for the vehicle is proposed as

$$\begin{aligned}\chi_{des} &= F(\theta_1, \theta_2) \\ &= \frac{\theta_1 + \theta_2}{2} + S(\theta_1, \theta_2)\end{aligned}\tag{2.8}$$

The first term on right hand side in Eq. (2.8), corresponds to the angular bisector of the two line-of-sight angles, that is, $\frac{\theta_1 + \theta_2}{2}$. The second term is a function defining a trajectory shaping bias angle that facilitates lateral traversal through the opening and is described subsequently. Consider the elliptic trajectory-shaping angle profile shown in red in Fig. 2.2 which is expressed as

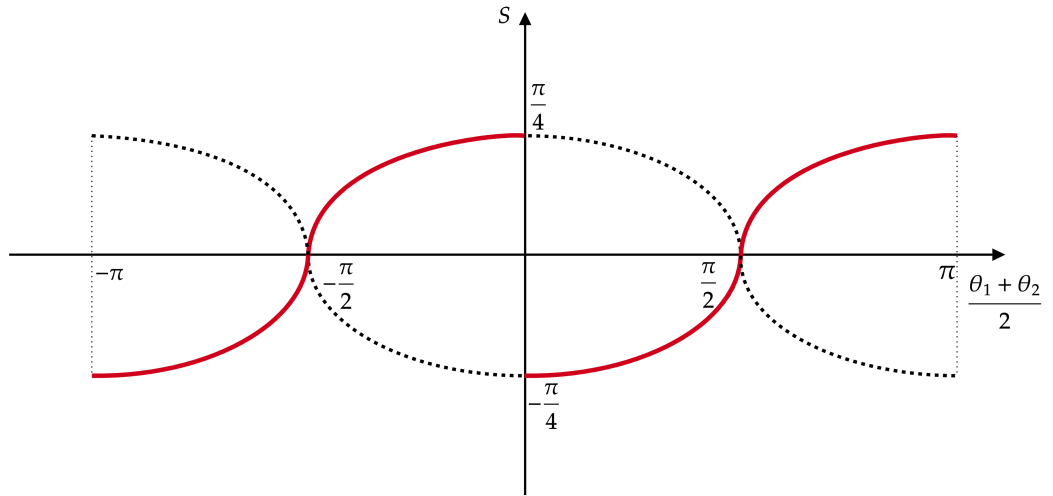


Figure 2.2: Elliptic shaping angle profile, $\frac{\theta_1 + \theta_2}{2} \in [-\pi, \pi)$

$$S(\theta_1, \theta_2) = \begin{cases} \operatorname{sgn}\left(\frac{\theta_1 + \theta_2}{2} + \frac{\pi}{2}\right) \frac{|\pi^2 - (\theta_1 + \theta_2)^2|^{\frac{1}{2}}}{4}, & \text{for } \theta_1(t), \theta_2(t) \in [-\pi, 0] \\ \operatorname{sgn}\left(\frac{\theta_1 + \theta_2}{2} - \frac{\pi}{2}\right) \frac{|\pi^2 - (\theta_1 + \theta_2)^2|^{\frac{1}{2}}}{4}, & \text{for } \theta_1(t), \theta_2(t) \in (0, \pi) \end{cases} \quad (2.9)$$

The signum function used in Eq. (2.9) can be expressed as

$$\operatorname{sgn}\left(\frac{\theta_1 + \theta_2}{2} - \frac{\pi}{2}\right) = \begin{cases} +1, & \text{for } \frac{\theta_1 + \theta_2}{2} > \frac{\pi}{2} \\ 0, & \text{for } \frac{\theta_1 + \theta_2}{2} = \frac{\pi}{2} \\ -1, & \text{for } \frac{\theta_1 + \theta_2}{2} < \frac{\pi}{2} \end{cases} \quad (2.10)$$

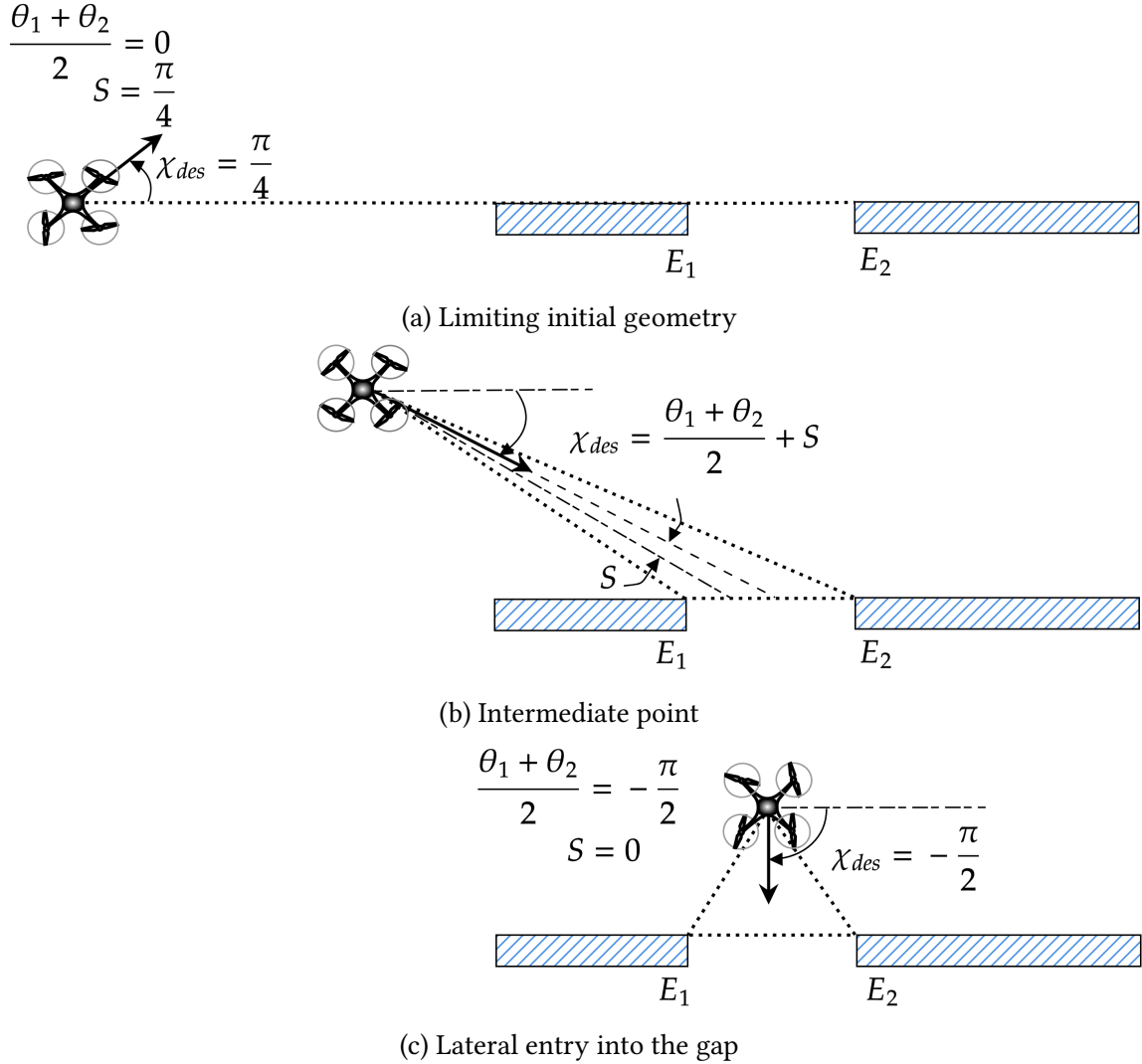


Figure 2.3: Instantaneous desired heading along the guided trajectory

As can be seen in Fig. 2.2, the key idea here is to vary the shaping angle as a function of the offset of the line-of-sight bisector angle $\frac{\theta_1+\theta_2}{2}$ with respect to the desired approach angle entering the gap opening, that is, an entry heading angle of $\pm\frac{\pi}{2}$. Figure 2.3 considers three specific instantaneous geometries and shows the instantaneous bias angle values and the desired heading directions. Consider Fig. 2.3a, which corresponds to the limiting case, where the quadrotor position is collinear with the edges E_1 and E_2 with $\theta_1, \theta_2 = 0$. Using that in Eq. (2.9), the bias angle is obtained as $S = \frac{\pi}{4}$ which provides necessary lateral clearance while taking the quadrotor closer to the gap. Consider Fig. 2.3b; a positive bias angle is still added to the bisector angle to shape the desired heading direction, which facilitates a lateral approach towards the gap opening. The line-of-sight bisector angle guides along the required entry angle into the gap opening for the instantaneous geometries illustrated in Fig. 2.3c and, as a result, the bias angle S is zero using Eq. (2.9).

2.3 Stability Characteristics

This section discusses the stability characteristics of the proposed guidance method followed by a phase portrait analysis.

Theorem 2.1 *Following the guidance command of Eq. (2.8) and subject to Eqs. (2.1)-(2.6), the vehicle motion is asymptotically stable about the gap center line.*

Proof: Consider an instantaneous geometry of a quadrotor approaching a gap as shown in Fig. (2.4). Let $2l$ be the width of the gap. The instantaneous lateral displacement d of the vehicle from the gap center line can be expressed as

$$d = -(R_2 \cos \theta_2 - l) \quad (2.11)$$

From Fig. (2.4), the gap width can also be expressed as

$$2l = R_2 \cos \theta_2 - R_1 \cos \theta_1 \quad (2.12)$$

Using Eq. (2.12) in Eq. (2.11),

$$d = -\left(\frac{R_2 \cos \theta_2 + R_1 \cos \theta_1}{2}\right) \quad (2.13)$$

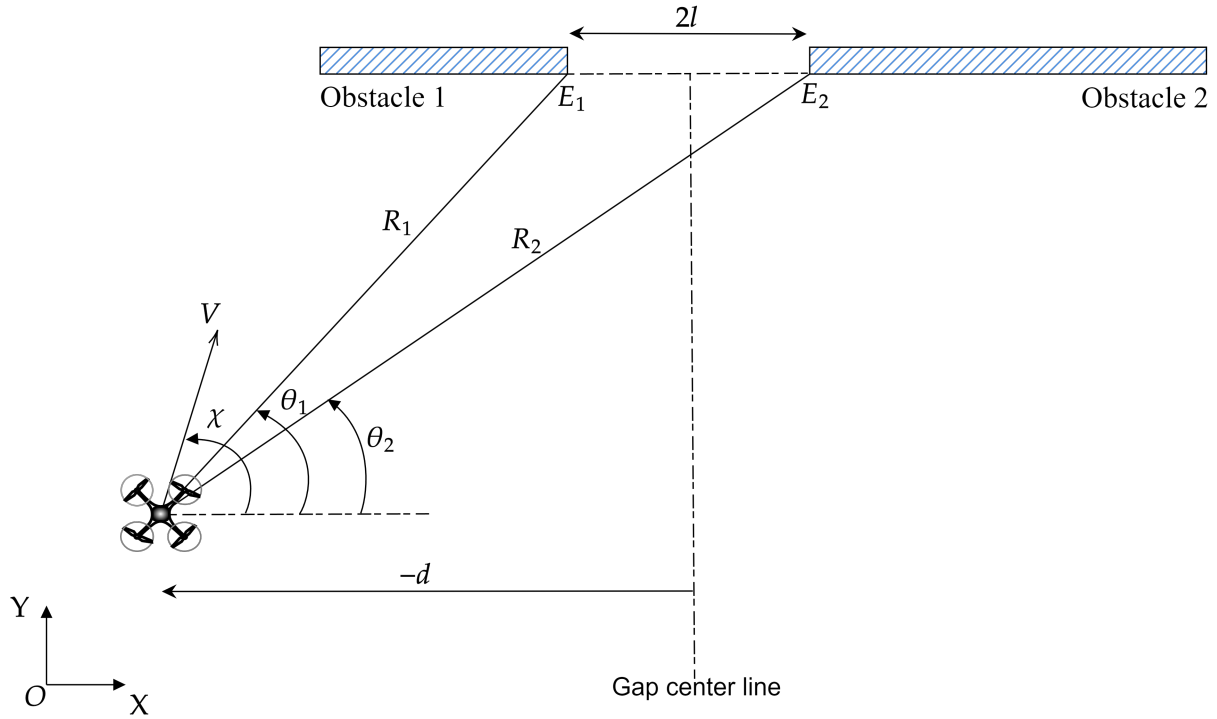


Figure 2.4: Instantaneous geometry

Consider a Lyapunov candidate function,

$$W = d^2 \quad (2.14)$$

Here, $W > 0$ for all $d \in \mathbb{R}_{\neq 0}$, and $W = 0$ at $d = 0$. Taking the time derivatives of the Lyapunov function in Eq. (2.14),

$$\dot{W} = 2d\dot{d} \quad (2.15)$$

Differentiating Eq. (2.13) with respect to time,

$$\dot{d} = -\frac{1}{2} \left(-R_2 \sin \theta_2 \dot{\theta}_2 + \cos \theta_2 \dot{R}_2 - R_1 \sin \theta_1 \dot{\theta}_1 + \cos \theta_1 \dot{R}_1 \right) \quad (2.16)$$

Using Eqs. (2.3)-(2.6) and $\chi = \chi_{des}$ in Eq. (2.16),

$$\dot{d} = V \cos \chi_{des} \quad (2.17)$$

Using Eq. (2.17) in Eq. (2.15),

$$\dot{W} = 2dV \cos \chi_{des} \quad (2.18)$$

From Fig. 2.4, it can be noted that

$$\frac{\sin \theta_1}{\sin \theta_2} = \frac{R_2}{R_1} \quad (2.19)$$

Rest of the analysis is divided into two cases:

1. Case 1: $d < 0$

From Eq. (2.13), when $d < 0$

$$R_2 \cos \theta_2 + R_1 \cos \theta_1 > 0 \quad (2.20)$$

which implies

$$\frac{R_2}{R_1} \cos \theta_2 + \cos \theta_1 > 0 \quad (2.21)$$

Using Eq. (2.19) and Eq. (2.21) with $d < 0$,

$$\begin{aligned} &\implies \frac{\sin \theta_1}{\sin \theta_2} \cos \theta_2 + \cos \theta_1 > 0 \\ &\implies \sin \theta_1 \cos \theta_2 + \cos \theta_1 \sin \theta_2 > 0 \\ &\implies \sin(\theta_1 + \theta_2) > 0 \end{aligned}$$

which implies

$$\frac{\theta_1 + \theta_2}{2} \in \left(0, \frac{\pi}{2}\right) \quad \forall d < 0 \quad (2.22)$$

From the proposed guidance command in Eq. (2.8), it can be deduced that

$$\chi_{des} \in \left(-\frac{\pi}{4}, \frac{\pi}{2}\right) \quad \forall \frac{\theta_1 + \theta_2}{2} \in \left(0, \frac{\pi}{2}\right) \quad (2.23)$$

Using Eq. (2.23) in Eq. (2.18) implies

$$\dot{W} < 0 \quad \forall d < 0 \quad (2.24)$$

2. Case 2: $d > 0$

From Eq. (2.13), for all $d > 0$

$$R_2 \cos \theta_2 + R_1 \cos \theta_1 < 0 \quad (2.25)$$

which implies

$$\frac{R_2}{R_1} \cos \theta_2 + \cos \theta_1 < 0 \quad (2.26)$$

From Eq. (2.19) and Eq. (2.26), when $d > 0$

$$\begin{aligned} &\implies \frac{\sin \theta_1}{\sin \theta_2} \cos \theta_2 + \cos \theta_1 < 0 \\ &\implies \sin \theta_1 \cos \theta_2 + \cos \theta_1 \sin \theta_2 < 0 \\ &\implies \sin(\theta_1 + \theta_2) < 0 \end{aligned}$$

which implies

$$\implies \frac{\theta_1 + \theta_2}{2} \in \left(\frac{\pi}{2}, \pi\right) \quad \forall d > 0 \quad (2.27)$$

From the guidance command in Eq. (2.8),

$$\chi_{des} \in \left(\frac{\pi}{2}, \frac{5\pi}{4}\right) \quad \forall \frac{\theta_1 + \theta_2}{2} \in \left(\frac{\pi}{2}, \pi\right) \quad (2.28)$$

Using Eq. (2.28) in Eq. (2.18) implies

$$\dot{W} < 0 \quad \forall d > 0 \quad (2.29)$$

From Eqs. (2.18), (2.24) and (2.29), It can be deduced that

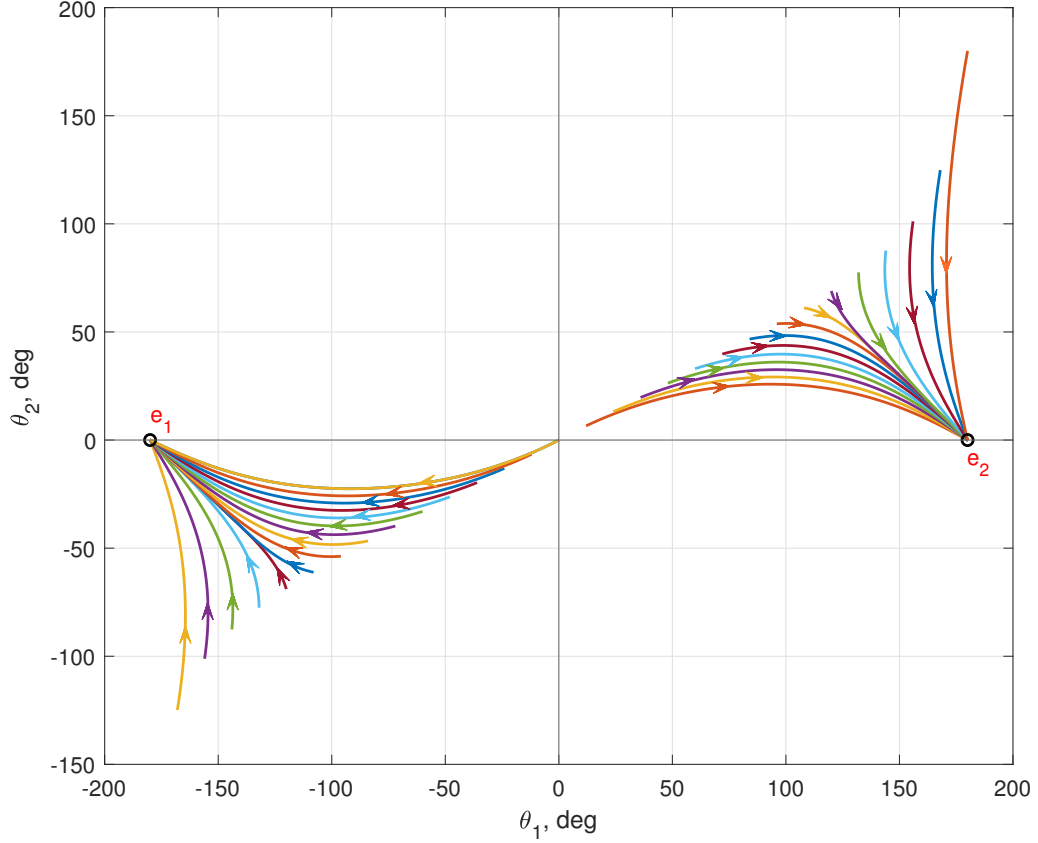
$$\dot{W} \leq 0 \quad \forall d \in \mathbb{R} \quad (2.30)$$

$$\dot{W} = 0 \quad \text{at } d = 0 \quad (2.31)$$

□

2.3.1 Phase portrait analysis

Using numerical simulation of the system Eqs. (2.1)-(2.6) and (2.8)-(2.10), we present a phase portrait analysis in θ_1 - θ_2 plane supporting the safe traversal property of the closed-loop kinematics subject to the proposed guidance command. In Fig. 2.5, phase plane trajectories are plotted for initial conditions $\theta_1(t_i), \theta_2(t_i) \in [-\pi, \pi]$. All trajectories reach $e_1((\theta_1, \theta_2) = (-\pi, 0))$ or $e_2((\theta_1, \theta_2) = (\pi, 0))$ which corresponds to the desired state for gap traversal.

Figure 2.5: Phase portrait in θ_1 - θ_2 plane

2.4 Quadrotor Dynamic Model and Control

The proposed guidance law provides the desired heading to follow the prescribed trajectories, and this section presents the detailed quadrotor model and tracking controllers for following the guidance command.

2.4.1 Quadrotor dynamic model

The free body diagram and coordinate system for the quadrotor are shown in Fig. 2.6 including the corresponding forces created by four rotors. The world frame, W , is defined by axes x_W , y_W , and z_W and body frame, B is defined by axes x_B , y_B , and z_B . Let $\tilde{r} = [x(t) \ y(t) \ z(t)]^T \in \mathbb{R}^3$ denote the position vector of the center of mass of the vehicle in the world frame. Let $[\phi(t) \ \theta(t) \ \psi(t)]^T \in \mathbb{R}^3$ represent the attitude vector consisting of roll(ϕ),

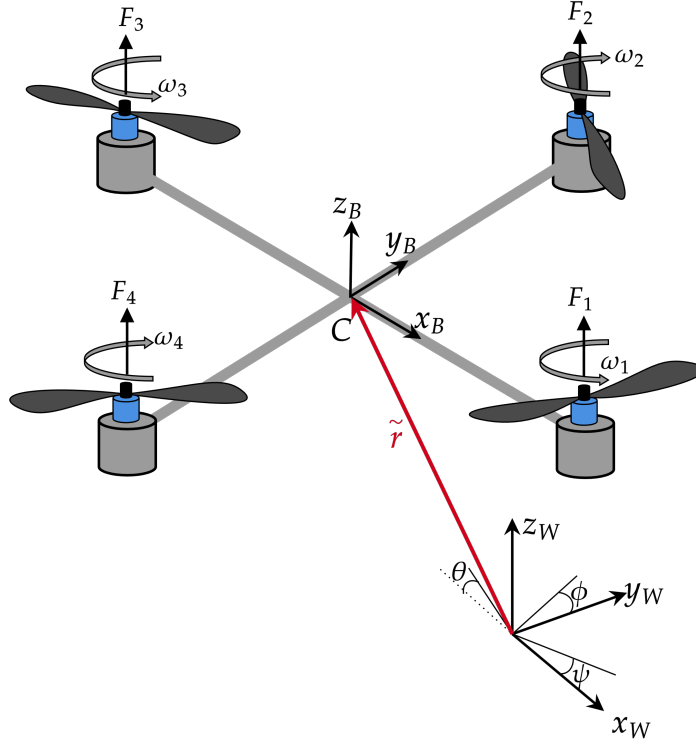


Figure 2.6: Coordinate frames and forces acting on the vehicle.

pitch(θ), and yaw(ψ) angles. Euler angle rotation matrix describing the rotation from the body frame to the world frame is defined as

$$R = \begin{bmatrix} C_\theta C_\psi & S_\phi S_\theta C_\psi - C_\phi S_\psi & C_\phi S_\theta C_\psi + S_\phi S_\psi \\ C_\theta S_\psi & S_\phi S_\theta S_\psi + C_\phi C_\psi & C_\phi S_\theta S_\psi - S_\phi C_\psi \\ -S_\theta & S_\phi C_\theta & C_\phi C_\theta \end{bmatrix} \quad (2.32)$$

where, S_ϕ and C_ϕ denote $\sin \phi$ and $\cos \phi$, respectively, and similarly for θ and ψ . The equations governing the acceleration of the center of mass can be described using the rotation matrix as

$$m \begin{bmatrix} \ddot{x} \\ \ddot{y} \\ \ddot{z} \end{bmatrix} = \begin{bmatrix} 0 \\ 0 \\ -mg \end{bmatrix} + R \begin{bmatrix} 0 \\ 0 \\ \sum_{i=1}^4 F_i \end{bmatrix} \quad (2.33)$$

where m is the mass of the vehicle, g the acceleration due to gravity and F_i represents the thrust force from the i^{th} rotor in z_B direction. The vertical thrust force can be expressed as

$$F_i = k_f \omega_i^2 \quad (2.34)$$

where k_f is the lift coefficient and ω_i represents the angular velocity of the i^{th} rotor. The rotors also produces torque

$$\tau_i = b\omega_i^2 \quad (2.35)$$

where b is the drag coefficient. The direction of torque produced by the rotor is opposite to the rotor rotating direction. Using Eq. (2.33), and considering the angles θ and ϕ to be small with negligible Coriolis terms in the derivatives of body frame angular velocities, simplified Newton-Euler equations of quadrotor motion can be written as [50]

$$\ddot{x} = (\cos \phi \sin \theta \cos \psi + \sin \phi \sin \psi) \frac{u_1}{m} \quad (2.36)$$

$$\ddot{y} = (\cos \phi \sin \theta \sin \psi - \sin \phi \cos \psi) \frac{u_1}{m} \quad (2.37)$$

$$\ddot{z} = -g + (\cos \phi \cos \theta) \frac{u_1}{m} \quad (2.38)$$

$$\ddot{\phi} = \frac{1}{J_x} u_2 \quad (2.39)$$

$$\ddot{\theta} = \frac{1}{J_y} u_3 \quad (2.40)$$

$$\ddot{\psi} = \frac{1}{J_z} u_4 \quad (2.41)$$

where, (J_x, J_y, J_z) are the moment of inertia referenced with respect to (x_B, y_B, z_B) axes, $u_1 = F = \sum_{i=1}^4 F_i$ is the total force acting on the quadrotor, and $u_2 = \tau_\phi$, $u_3 = \tau_\theta$, $u_4 = \tau_\psi$ are rolling torque, pitching torque, and yawing torque, respectively. The rolling torque is produced by the rotor 2 and rotor 4 as

$$\tau_\phi = lk_f(\omega_2^2 - \omega_4^2) \quad (2.42)$$

where l is the distance between center of mass of the quadrotor and the axis of a rotor. Similarly the pitching torque is produced by the rotor 1 and 3 as

$$\tau_\theta = lk(\omega_3^2 - \omega_1^2) \quad (2.43)$$

The drag of the rotor propellers generate yawing torque on the body of the quadrotor. The yawing torque is given by

$$\tau_\psi = \sum_{i=1}^4 \tau_i \quad (2.44)$$

Eqs. (2.36)-(2.41) relate the double derivatives of the translational and rotational position of the quadrotor to the control inputs. The angular velocity components of the vehicle in the body frame are p , q , and r , which are related to the derivative of roll, pitch, and yaw angle according to Eq. (2.45).

$$\begin{bmatrix} p \\ q \\ r \end{bmatrix} = \begin{bmatrix} 1 & 0 & -\sin \theta \\ 0 & \cos \phi & \sin \phi \cos \theta \\ 0 & -\sin \phi & \cos \phi \cos \theta \end{bmatrix} \begin{bmatrix} \dot{\phi} \\ \dot{\theta} \\ \dot{\psi} \end{bmatrix} \quad (2.45)$$

2.4.2 Tracking control

The guided trajectory is expressed in terms of desired heading angle χ_{des} as given in Eq. (2.8). The controller is herein designed to ensure that the quadrotor follows the desired heading angle. The guidance and tracking control architecture is shown in Fig. 2.7. The key idea here is to relate the control inputs $u_2 - u_4$ to a corresponding vehicle orientation which, in turn, is related to the heading command of Eq. (2.8) through translational acceleration. The four control

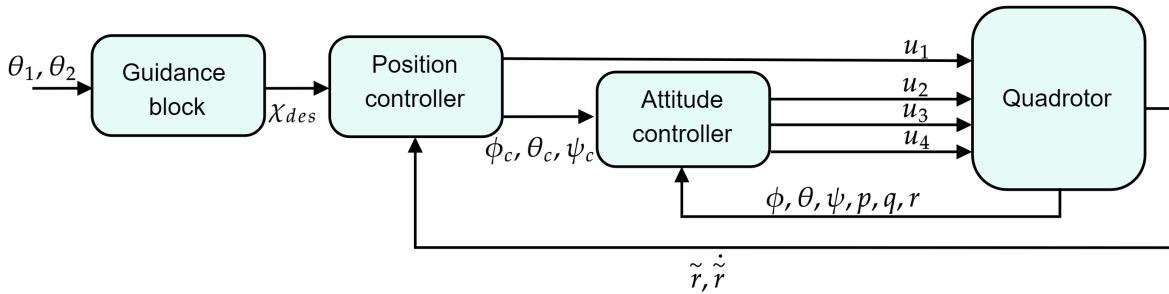


Figure 2.7: Guidance and tracking control architecture.

inputs are related to the desired altitude and desired attitude angles using a Proportional-Derivative (PD) control logic [21] as

$$u_1 = m(g + K_{dz}(\dot{z}_{des} - \dot{z}) + K_{pz}(z_{des} - z)) \quad (2.46)$$

$$u_2 = K_{d\phi}(p_c - p) + K_{p\phi}(\phi_c - \phi) \quad (2.47)$$

$$u_3 = K_{d\theta}(q_c - q) + K_{p\theta}(\theta_c - \theta) \quad (2.48)$$

$$u_4 = K_{d\psi}(r_c - r) + K_{p\psi}(\psi_c - \psi) \quad (2.49)$$

where (K_{dz}, K_{pz}) , $(K_{d\phi}, K_{p\phi})$, $(K_{d\theta}, K_{p\theta})$ and $(K_{d\psi}, K_{p\psi})$ represent the tunable controller gains for u_1 , u_2 , u_3 , and u_4 . Using small angle approximation for ϕ and θ in Eqs. (2.36)-(2.37), the commanded roll and pitch angles can be related to the commanded translational acceleration in x_W - y_W as

$$\phi_c = \frac{1}{g} (\ddot{x}_c \sin \psi_{des} - \ddot{y}_c \cos \psi_{des}) \quad (2.50)$$

$$\theta_c = \frac{1}{g} (\ddot{x}_c \cos \psi_{des} + \ddot{y}_c \sin \psi_{des}) \quad (2.51)$$

We consider the commanded yaw angle to be equal to the desired yaw angle as

$$\psi_c = \psi_{des} \quad (2.52)$$

Using Eqs. (2.50)-(2.52) the derivatives of commanded roll, pitch and yaw angle can be written as

$$\dot{\phi}_c = \frac{1}{g} \left(\ddot{x}_c \sin \psi_{des} + \ddot{x}_c \cos \psi_{des} \dot{\psi}_{des} - \ddot{y}_c \cos \psi_{des} + \ddot{y}_c \sin \psi_{des} \dot{\psi}_{des} \right) \quad (2.53)$$

$$\dot{\theta}_c = \frac{1}{g} \left(\ddot{x}_c \cos \psi_{des} - \ddot{x}_c \sin \psi_{des} \dot{\psi}_{des} + \ddot{y}_c \sin \psi_{des} + \ddot{y}_c \cos \psi_{des} \dot{\psi}_{des} \right) \quad (2.54)$$

$$\dot{\psi}_c = \dot{\psi}_{des} \quad (2.55)$$

The commanded angular velocity components p_c , q_c , r_c are computed using the derivatives of ϕ_c , θ_c , ψ_c in Eq. (2.45). The commanded acceleration components \ddot{x}_c and \ddot{y}_c are again computed using PD control logic using position and velocity errors as

$$\ddot{x}_c = \ddot{x}_{des} + K_{px}(x_{des} - x) + K_{dx}(\dot{x}_{des} - \dot{x}) \quad (2.56)$$

$$\ddot{y}_c = \ddot{y}_{des} + K_{py}(y_{des} - y) + K_{dy}(\dot{y}_{des} - \dot{y}) \quad (2.57)$$

where the terms \ddot{x}_{des} , \ddot{y}_{des} represents feedforward terms on the desired acceleration. The commanded jerk components are computed using PD control logic using velocity and acceleration errors as

$$\dddot{x}_c = \dddot{x}_{des} + K_{pjx}(\dot{x}_{des} - \dot{x}) + K_{dix}(\ddot{x}_{des} - \ddot{x}) \quad (2.58)$$

$$\dddot{y}_c = \dddot{y}_{des} + K_{pjiy}(\dot{y}_{des} - \dot{y}) + K_{dijy}(\ddot{y}_{des} - \ddot{y}) \quad (2.59)$$

At lower accelerations the terms \ddot{x}_{des} , \ddot{y}_{des} , \ddot{x}_{des} , and \ddot{y}_{des} can be ignored [21]. Accordingly, simplified commanded acceleration and jerk components, respectively, are written as

$$\ddot{x}_c = K_{px}(x_{des} - x) + K_{dx}(\dot{x}_{des} - \dot{x}) \quad (2.60)$$

$$\ddot{y}_c = K_{py}(y_{des} - y) + K_{dy}(\dot{y}_{des} - \dot{y}) \quad (2.61)$$

$$\ddot{x}_c = K_{pjx}(\dot{x}_{des} - \dot{x}) + K_{djx}(-\ddot{x}) \quad (2.62)$$

$$\ddot{y}_c = K_{p jy}(\dot{y}_{des} - \dot{y}) + K_{d jy}(-\ddot{y}) \quad (2.63)$$

Here, (K_{dx}, K_{px}) , (K_{dy}, K_{py}) , (K_{djx}, K_{pjx}) , and $(K_{d jy}, K_{p jy})$ represent tunable controller gains for \ddot{x}_c , \ddot{y}_c , \ddot{x}_c and \ddot{y}_c . The desired position derivatives can be related to the proposed guidance command of Eq. (2.8) as

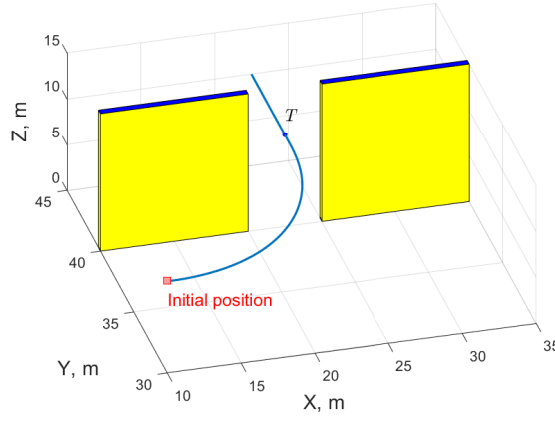
$$\begin{aligned} \dot{x}_{des}(t) &= V \cos(\chi_{des}(t)) \\ \dot{y}_{des}(t) &= V \sin(\chi_{des}(t)) \end{aligned} \quad (2.64)$$

which, in turn, are related to the desired position as

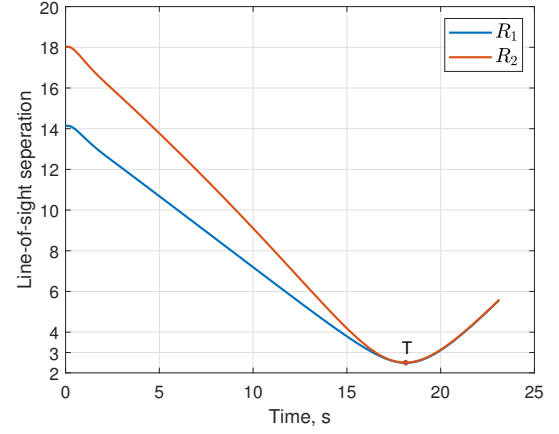
$$\begin{aligned} x_{des} &= \int_0^t \dot{x}_{des}(t) dt \\ y_{des} &= \int_0^t \dot{y}_{des}(t) dt \end{aligned} \quad (2.65)$$

2.5 Simulation Results

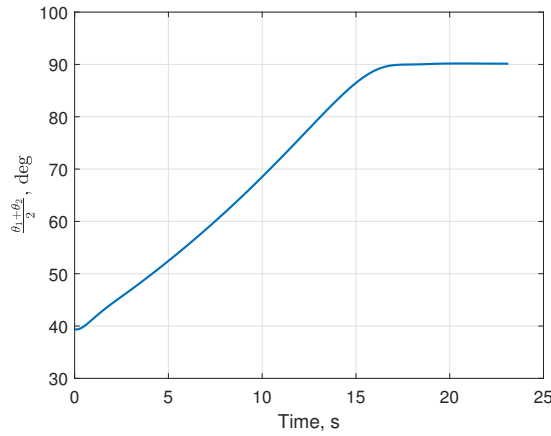
In this section, the proposed guidance logic is evaluated on a quadrotor model with mass $m = 0.47$ kg and moment of inertia $J_x = 0.0086$ kg-m², $J_y = 0.0086$ kg-m², $J_z = 0.0176$ kg-m² [51]. The desired quadrotor speed is considered to be $V = 1$ m/s. The proposed guidance is used up to the point when the traversability condition of Eq. (2.7) is satisfied. Upon satisfying Eq. (2.7), it is assumed that the vehicle continues to follow the already achieved constant heading direction of $\chi_{des} = \pm \frac{\pi}{2}$ rad. The controller gains are selected as $K_{dz} = 3.5$, $K_{pz} = 3.8$, $K_{d\phi} = 0.5$, $K_{p\phi} = 12.8$, $K_{d\theta} = 0.2$, $K_{p\theta} = 1.8$, $K_{d\psi} = 0.5$, $K_{p\psi} = 2$, $K_{djx} = 3.5$, $K_{pjx} = 6$, $K_{d jy} = 4.2$, $K_{p jy} = 12.7$, $K_{dx} = 3.5$, $K_{px} = 6$, $K_{dy} = 4.2$, and $K_{py} = 12.7$. All simulations use desired altitude and desired yaw angle of 10 m and 0.1 rad, respectively. The commanded roll and pitch angles are saturated to lie within ± 20 deg.



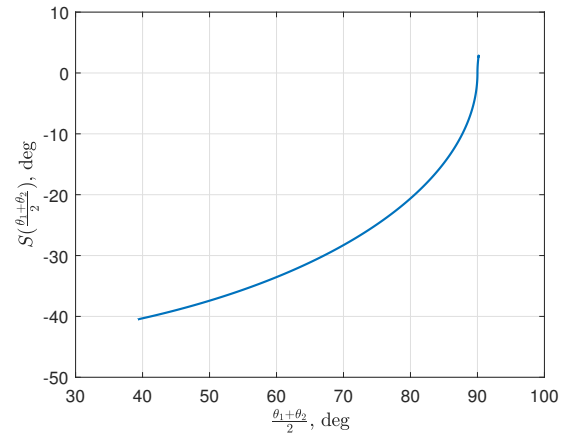
(a) Quadrotor trajectory



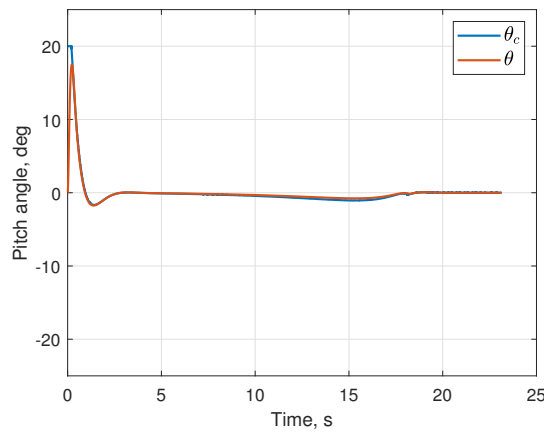
(b) Distance from gap extremities



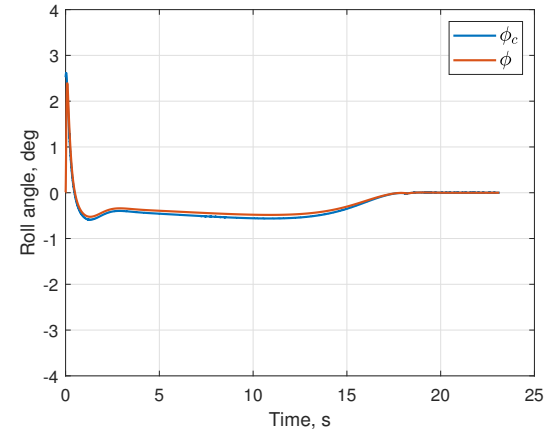
(c) Line-of-sight angular bisector variation



(d) Shaping angle profile



(e) Pitch angle response



(f) Roll angle response

Figure 2.8: Results for Case 1.

2.5.1 Case 1. Sample scenario with noise free gap bearing angles

In this case, the proposed guidance trajectory is generated using noise-free bearing angle information θ_1 and θ_2 of gap edges E_1 and E_2 respectively. This case considers a gap width of 5 m between two rectangular obstacles of height 15 m as shown in Fig. 2.8a. The vehicle initial position is $(x_i, y_i, z_i) = (10, 30, 10)$ m, gap edges are $E_1 = (20, 40, 10)$ m and $E_2 = (25, 40, 10)$ m. The initial gap bearing angles are accordingly deduced as $\theta_1(t_i) = 45$ deg, and $\theta_2(t_i) = 33.69$ deg. Figure 2.8a plots quadrotor trajectory safely passing through the gap. Figure 2.8b plots the vehicle distance from E_1 and E_2 , and it can be seen that the vehicle reaches the traversal point $T(22.5, 40, 10)$ at $t = 18.1325$ s at a distance of 2.5 m from E_1 and E_2 . In Fig. 2.8c, the variation of line-of-sight angular bisector term $\left(\frac{\theta_1 + \theta_2}{2}\right)$ is depicted, with the line-of-sight angular bisector term reaching its final desired value of 90 deg, leading to the desired entry into the gap. Figure 2.8d plots the variation in shaping angle S , which as governed by Eq. (2.9), is a monotonically increasing function of $\left(\frac{\theta_1 + \theta_2}{2}\right)$. The shaping angle increases to zero as the bisector angles attains its desired value. The time response of pitch and roll tracking controller is shown in Figs. 2.8e and 2.8f, respectively. Results shows a good inner loop tracking of attitude angles. The traversal velocity profile of the vehicle is shown in Fig. 2.9a where the vehicle achieves the desired speed of 1 m/s starting from the given initial speed of 0 m/s. Figure 2.9b presents an accurate tracking of the desired altitude of 10 m with maximum error less than 0.03 m.

2.5.2 Case 2. Effect of noise in bearing angle information

In this study, the guidance command of Eq. (2.8) uses noisy edge bearing measurements $\theta_{1_m}(t)$, $\theta_{2_m}(t)$, which are generated using a zero-mean Gaussian noise of standard deviation of 4 deg with a sampling time of 1 ms being added to the true values, $\theta_1(t)$ and $\theta_2(t)$, respectively. Robustness of the algorithm is studied with respect of unfiltered $\theta_{1_m}(t)$, $\theta_{2_m}(t)$ utilized in the guidance command of Eq. (2.8). This simulation scenario is identical to the one considered in case 1. Figure 2.10a plots the quadrotor trajectory, which shows the safe traversal of the vehicle through the gap. True and measured value of bearing angles are plotted in Figs. 2.10b and 2.10c. The line-of-sight separation with respect to gap edges from E_1 and E_2 , respectively,

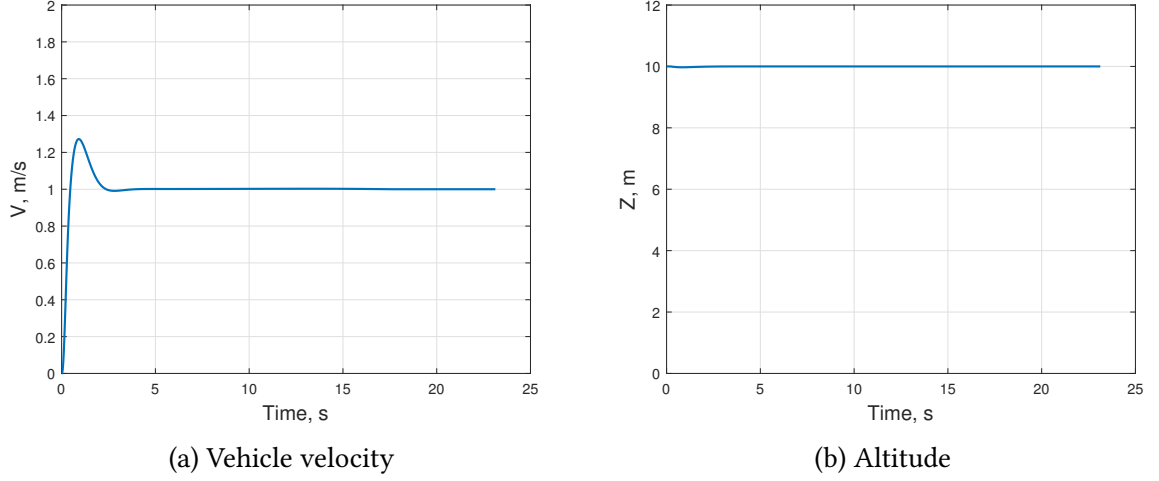


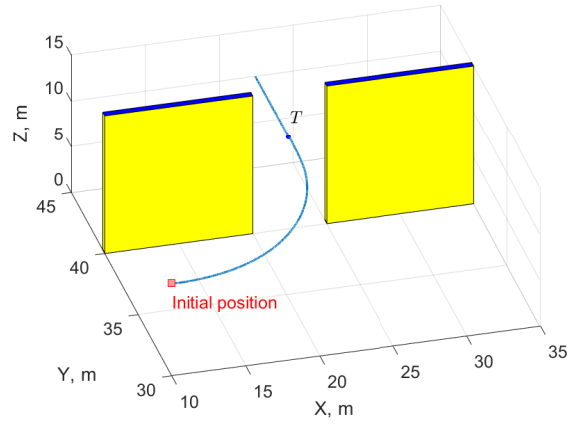
Figure 2.9: Velocity and altitude response for Case 1.

shown in Fig. 2.10d,c which shows that the vehicle keeps a safe distance of 2.4472 m and 2.5525 m at traversal point T .

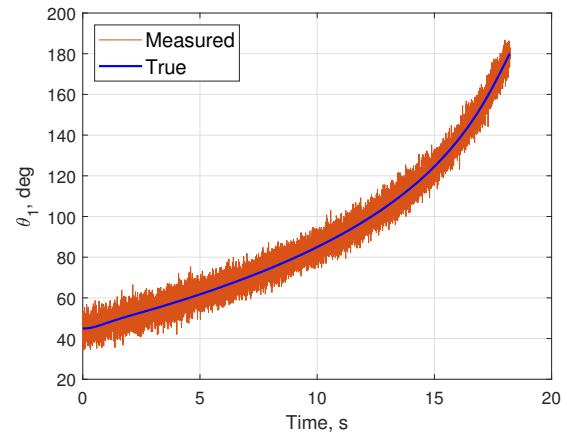
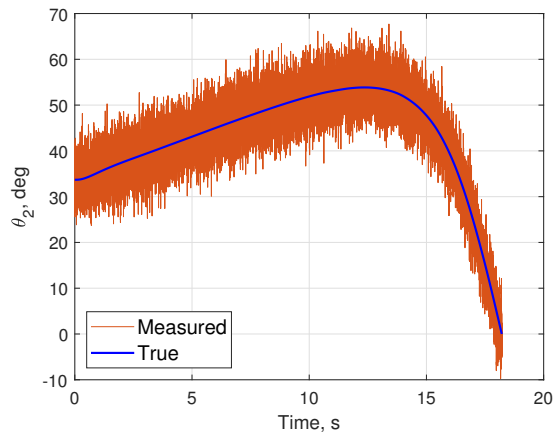
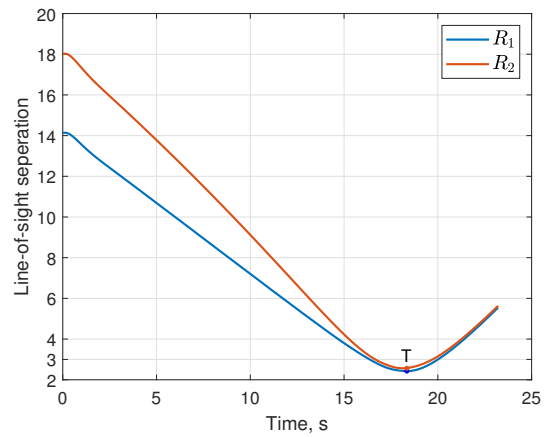
As a multiple gap traversal scenario, we augment the scene with two additional gaps with edges at (15, 60, 10) m-(18, 60, 10) m and (20, 78, 10) m-(21, 78, 10) m, respectively. The quadrotor trajectory for this scenario is shown in Fig. 2.10e. From its initial position (18, 25, 10) m, the quadrotor traverses the three gaps passing through traversal points T_1 , T_2 , and T_3 , respectively. The quadrotor uses the proposed guidance logic considering bearing information of the Gap-1 until it reaches the traversal point T_1 where Eq. (2.7) is satisfied. The quadrotor then switches to the edge bearing information for Gap-2 and reaches the traversal point T_2 . Finally, the logic is repeated for arriving at T_3 , the traversal point at Gap-3.

2.5.3 Case 3. Various initial conditions and noisy measurements

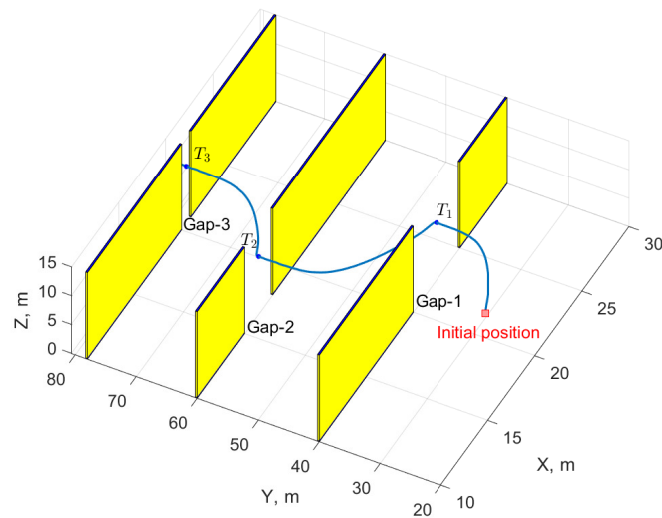
Considering several initial conditions as shown in Table 2.1, quadrotor trajectories are generated using the proposed guidance strategy. We consider four different initial conditions, each at altitude levels 6 m, 8 m, 10 m, and 12 m, and a desired gap traversal at an altitude of 10 m. The bearing measurements are considered to be noisy with characteristics identical to those considered in case 2. Trajectories plotted in Fig. 2.11 indicate that the quadrotor safely traverses through the gap. In this representative 3-D case, the guidance commands are generated considering an instantaneous 2-D horizontal plane passing through the vehicle instantaneous



(a) Quadrotor trajectory

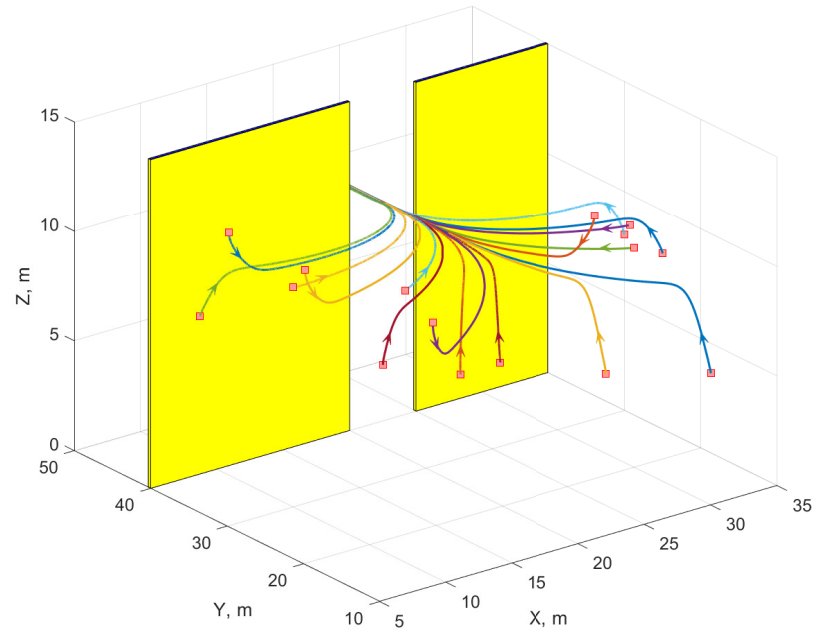
(b) Bearing angle θ_1 (c) Bearing angle θ_2 

(d) Distance from gap extremities

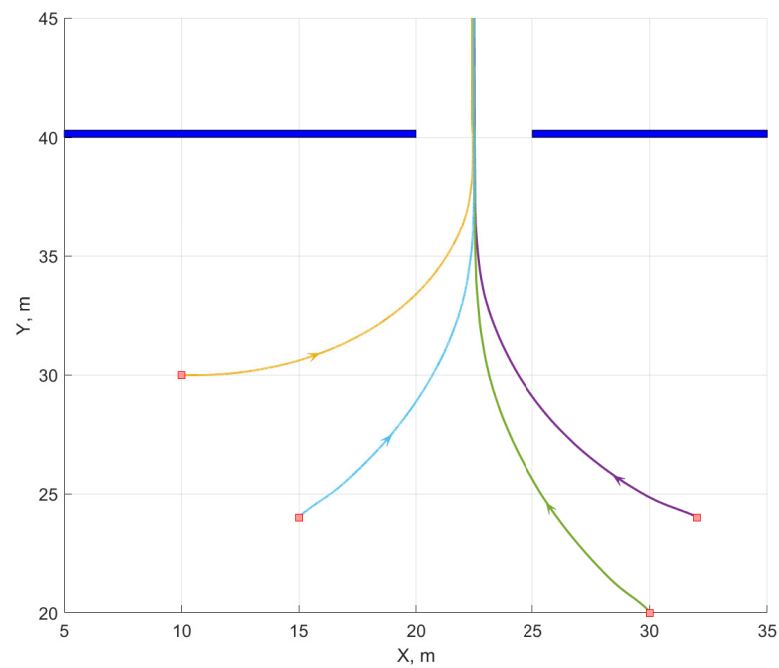


(e) Quadrotor trajectory-multiple gaps

Figure 2.10: Results for Case 2.



(a) Quadrotor trajectories



(b) Top view of trajectories starting at 10 m altitude

Figure 2.11: Results for Case 3.

position. For the initial conditions considered, the closest distance between the traversal point and gap edges varies between 2.3001 m and 2.4726 m.

Table 2.1: Initial conditions for Case 3.

x_i, y_i (altitude= 6 m)	x_i, y_i (altitude= 8 m)	x_i, y_i (altitude= 10) m	x_i, y_i (altitude= 12 m)
(21,22)	(7,37)	(10,30)	(8,35)
(30,10)	(35,30)	(32,24)	(27,20)
(18,22)	(11,20)	(30,20)	(8,25)
(25,15)	(35,25)	(15,24)	(9,10)

Further, a Monte-Carlo simulation is carried out for 100 random initial conditions. With uniform distributions, the initial coordinates satisfy $x_i \in [0, 50]$ m, $y_i \in [0, 39]$ m and $z_i \in [5, 15]$ m, respectively. The guidance method ensures safe traversal for all the initial conditions. The mean distance between the traversal point and the two gap extremities is obtained as $\mu_1 = 2.4806$ m and $\mu_2 = 2.5188$ m, respectively, with a corresponding standard deviation of $\sigma_1 = 0.0557$ m and $\sigma_2 = 0.0556$ m, respectively. These results are in concurrence with the analysis presented in Subsection 2.3.1. This study highlights the robustness of the proposed guidance method with respect to the initial position of the quadrotor.

2.6 Summary

This chapter addresses the quadrotor guidance problem of moving through a gap using relative bearings-only information of the gap extremities. The desired heading direction comprises an angle bisector of the bearing orientation of gap extremities and an elliptical trajectory-shaping angle proposed for lateral maneuver through the gap opening. Stability characteristics of the proposed guidance method followed by a phase plane analysis of closed-loop bearing angles are presented, ensuring guaranteed safe traversal. The proposed guidance method is applied to a six-degree-of-freedom quadrotor model combined with a tracking controller to ensure convergence towards the prescribed trajectory. Simulation results are presented to validate the effectiveness of the proposed traversal guidance strategy considering several initial conditions, noisy bearing measurements, and dynamic limits on roll and pitch angles. Robustness of the proposed method is verified using Monte-Carlo simulations considering random initial

conditions and noisy bearing measurements.

Chapter 3

Three-Dimensional Guidance for Window Traversal

This chapter presents a guidance method for three-dimensional window traversal using bearings-only information of the window extremities. The guidance commands include a desired flight path angle to follow the desired traversal altitude and a desired heading angle, which is further development of the idea presented in Chapter 2. The stability analysis of the resulting kinematics is analyzed, and a phase plane analysis is carried out. This chapter also presents a detailed qualitative comparison study between existing methods and proposed traversal strategies discussed in Chapters 2 and 3. Numerical simulation case studies are carried out on a realistic six-degree-of-freedom model.

3.1 Problem Description

Consider a quadrotor approaching a rectangular window in three-dimensional space as shown in Fig. 3.1. Here, $[x \ y \ z]^T \in \mathbb{R}^3$ denotes the position vector of the vehicle in a fixed $X - Y - Z$ frame. The window has four extremities, labeled as $E_1(x_1, y_1, z_1)$, $E_2(x_2, y_2, z_2)$, $E_3(x_3, y_3, z_3)$, and $E_4(x_4, y_4, z_4)$, respectively, and the dimensions are denoted as a and b . Without loss of generality, the fixed reference frame is considered with its XZ plane parallel to the window frame. The quadrotor has an onboard vision sensor that can measure the three-dimensional bearing angles of four window extremities. Using the information available, the objective is to design a guidance solution that enables the quadrotor to fly through the window safely.

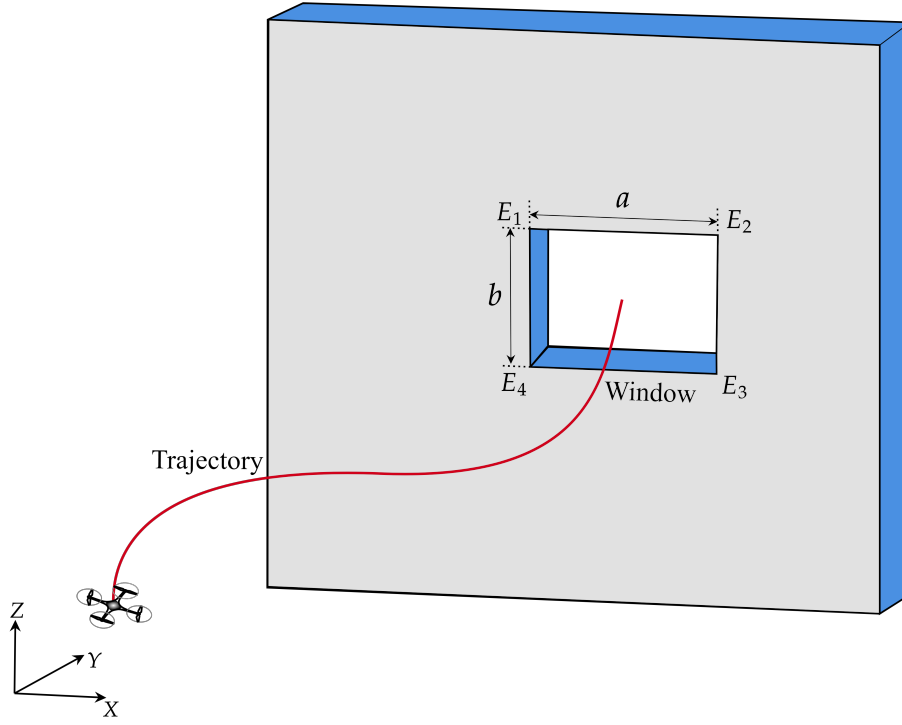


Figure 3.1: Quadrotor approaching a window.

3.2 Proposed Guidance Method

Consider a relative instantaneous geometry between the quadrotor and an i^{th} extremity point of the window $E_i(x_i, y_i, z_i)$, as shown in Fig. 3.2. Here, R_i represents the line-of-sight separation between the quadrotor and E_i . The azimuth and elevation angles for R_i can be expressed as

$$\beta_i = \tan^{-1} \left(\frac{y_i - y}{x_i - x} \right) \quad (3.1)$$

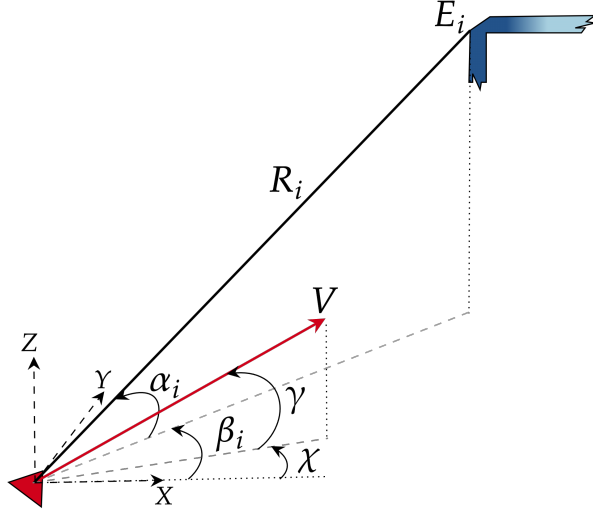
$$\alpha_i = \sin^{-1} \left(\frac{z_i - z}{R_i} \right) \quad (3.2)$$

where $\beta_i \in [-\pi, \pi)$ and $\alpha_i \in [-\frac{\pi}{2}, \frac{\pi}{2}]$. The line-of-sight separation R_i is given by

$$R_i = ((x_i - x)^2 + (y_i - y)^2 + (z_i - z)^2)^{\frac{1}{2}} \quad (3.3)$$

Kinematic equations of motion of a point object quadrotor in a three-dimensional space can be expressed as

$$\dot{x}(t) = V \cos \gamma(t) \cos \chi(t) \quad (3.4)$$

Figure 3.2: Relative geometry between quadrotor and E_i

$$\dot{y}(t) = V \cos \gamma(t) \sin \chi(t) \quad (3.5)$$

$$\dot{z}(t) = V \sin \gamma(t) \quad (3.6)$$

where $V, \chi \in [-\pi, \pi)$ and $\gamma \in [-\frac{\pi}{2}, \frac{\pi}{2}]$ represent speed, heading angle and flight path angle of the point object quadrotor, respectively. The three-dimensional kinematic equation of relative motion of the quadrotor with respect to any i^{th} extremity point of the window can be expressed as [52, 53]

$$\dot{R}_i = -V (\cos \gamma \cos \alpha_i \cos(\chi - \beta_i) + \sin \gamma \sin \alpha_i) \quad (3.7)$$

$$R_i \dot{\alpha}_i = -V (-\cos \gamma \sin \alpha_i \cos(\chi - \beta_i) + \sin \gamma \cos \alpha_i) \quad (3.8)$$

$$R_i \dot{\beta}_i \cos \alpha_i = -V \cos \gamma \sin(\chi - \beta_i) \quad (3.9)$$

An angular bisector approach which uses azimuth and elevation angles of window extremities is presented as a solution to the problem. Elevation angles α_i 's are used to generate the guidance logic for the desired flight path angle, and azimuth angles β_i 's are used to generate the desired heading angle of the point object quadrotor. Using Eqs. (3.1) and (3.2), desired bearing angles when the quadrotor is at the centroid of the window can be expressed as

$$\beta_1(t_T) = \beta_4(t_T) = \pm 180 \text{ deg.} \quad \beta_2(t_T) = \beta_3(t_T) = 0 \quad (3.10)$$

$$\alpha_1(t_T) = -\alpha_4(t_T) = \alpha_2(t_T) = -\alpha_3(t_T) = \sin^{-1} \left(\frac{b}{\sqrt{a^2 + b^2}} \right) \quad (3.11)$$

where t_T is the time at which the quadrotor reaches the window.

3.2.1 Desired flight path angle

Using elevation angles of the extremities E_1 and E_4 , the desired flight path angle for the vehicle is proposed as

$$\gamma_{des} = \begin{cases} \frac{\alpha_1 + \alpha_4}{2} + S_\gamma & \forall \frac{\alpha_1 + \alpha_4}{2} + S_\gamma \in \left[-\frac{\pi}{2}, \frac{\pi}{2}\right] \end{cases} \quad (3.12a)$$

$$\gamma_{des} = \begin{cases} \pi - \left(\frac{\alpha_1 + \alpha_4}{2} + S_\gamma\right) & \forall \frac{\alpha_1 + \alpha_4}{2} + S_\gamma > \frac{\pi}{2} \end{cases} \quad (3.12b)$$

$$\gamma_{des} = \begin{cases} -\left(\pi + \frac{\alpha_1 + \alpha_4}{2} + S_\gamma\right) & \forall \frac{\alpha_1 + \alpha_4}{2} + S_\gamma < -\frac{\pi}{2} \end{cases} \quad (3.12c)$$

where the term $\frac{\alpha_1 + \alpha_4}{2}$ represents the angular bisector component and the term S_γ represents shaping angle component. Further, the shaping angle function in Eq. (3.12) is proposed as

$$S_\gamma(\alpha_1, \alpha_4) = \begin{cases} \operatorname{sgn}\left(\frac{\alpha_1 + \alpha_4}{2}\right) \frac{\left|\pi^2 - 4\left(\frac{\alpha_1 + \alpha_4}{2} + \frac{\pi}{2}\right)^2\right|^{\frac{1}{2}}}{4}, & \text{for } \frac{\alpha_1 + \alpha_4}{2} \in \left[-\frac{\pi}{2}, 0\right] \\ \operatorname{sgn}\left(\frac{\alpha_1 + \alpha_4}{2}\right) \frac{\left|\pi^2 - 4\left(\frac{\alpha_1 + \alpha_4}{2} - \frac{\pi}{2}\right)^2\right|^{\frac{1}{2}}}{4}, & \text{for } \frac{\alpha_1 + \alpha_4}{2} \in \left(0, \frac{\pi}{2}\right] \end{cases} \quad (3.13)$$

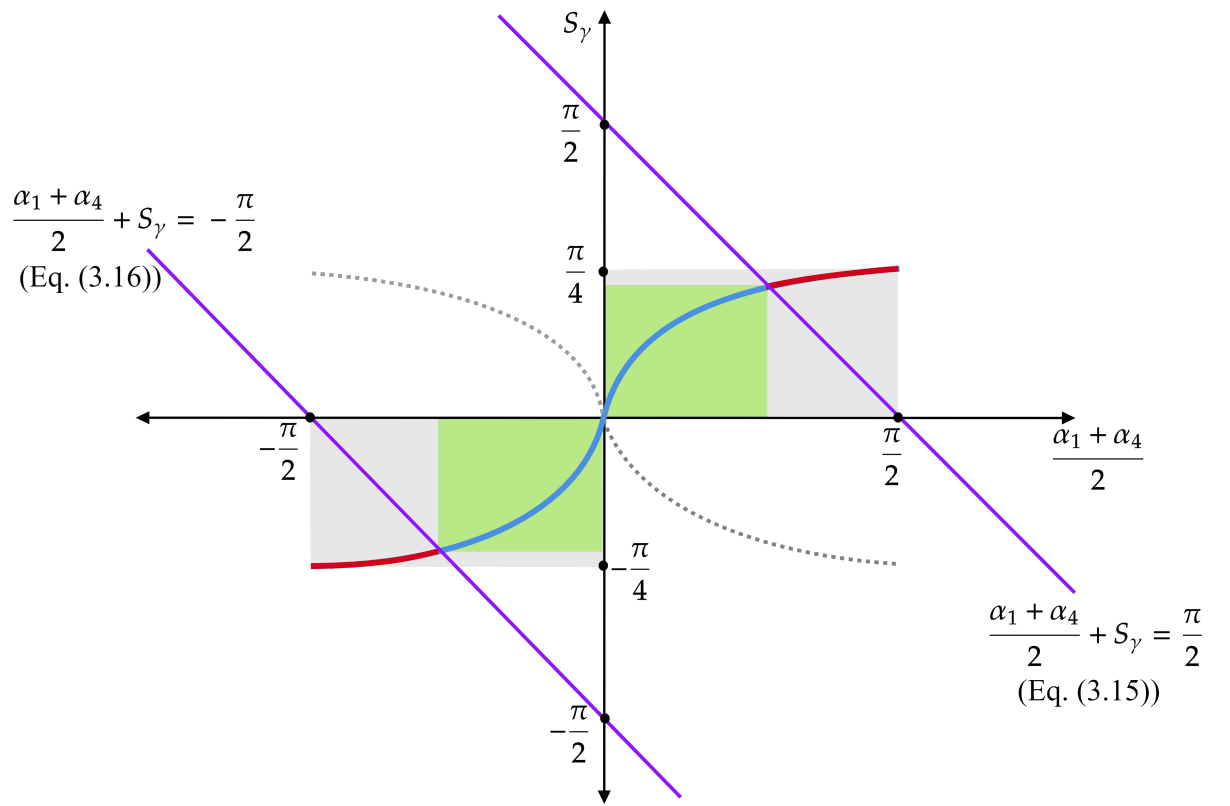
The signum function utilized in Eq. (3.13) is given by

$$\operatorname{sgn}\left(\frac{\alpha_1 + \alpha_4}{2}\right) = \begin{cases} +1, & \text{for } \frac{\alpha_1 + \alpha_4}{2} > 0 \\ 0, & \text{for } \frac{\alpha_1 + \alpha_4}{2} = 0 \\ -1, & \text{for } \frac{\alpha_1 + \alpha_4}{2} < 0 \end{cases} \quad (3.14)$$

Figure 3.3 depicts the relationship between the shaping angle and the angular bisector components. The key idea behind the proposed guidance approach (Eqs. (3.12)-(3.14)) is to adjust the shaping angle as a function of the angular bisector to achieve the desired flight path angle for flying through the window. The elliptical shaping angle profile illustrated in Fig. 3.3 comprises three operating regions separated by two violet lines defined by Eqs. (3.15) and (3.16) as

$$\frac{\alpha_1 + \alpha_4}{2} + S_\gamma = \frac{\pi}{2} \quad (3.15)$$

$$\frac{\alpha_1 + \alpha_4}{2} + S_\gamma = -\frac{\pi}{2} \quad (3.16)$$

Figure 3.3: Elliptic shaping angle profile for γ_{des}

The blue curve within the green-shaded region contributes to the desired flight path angle as governed by Eq. (3.12a). Equation (3.12a) limits the desired flight path angle within the feasible range $\gamma_{des} \in [-\frac{\pi}{2}, \frac{\pi}{2}]$. The red curve in the gray-shaded region to the right of the line defined by Eq. (3.15) determines the desired flight path angle according to Eq. (3.12b). Therein, since $\frac{\alpha_1 + \alpha_4}{2} + S_\gamma > \frac{\pi}{2}$, the desired flight path angle lies in $(0, \frac{\pi}{2})$. Similarly, the red curve in the gray-shaded region to the left of the line defined by Eq. (3.16) determines the desired flight path angle as in Eq. (3.12c), ensuring $\gamma_{des} \in (-\frac{\pi}{2}, 0)$ when $\frac{\alpha_1 + \alpha_4}{2} + S_\gamma < -\frac{\pi}{2}$.

Figure 3.4 considers three specific instantaneous geometries, displaying corresponding shaping angle values and desired flight path angles. Consider an instantaneous limiting geometry where the quadrotor makes elevation angles of $\alpha_1 = \alpha_4 = \frac{\pi}{2}$ rad, as shown in Fig. 3.4a. From Eq. (3.13) and as illustrated in Fig. 3.3, the shaping angle requirement S_γ for $\frac{\alpha_1 + \alpha_4}{2} = \frac{\pi}{2}$ rad is $\frac{\pi}{4}$ rad. This implies $\frac{\alpha_1 + \alpha_4}{2} + S_\gamma > \frac{\pi}{2}$, which corresponds to a point on the red color curve within the gray region shown in Fig. 3.3. The guidance command in Eq. (3.12b) directs the quadrotor at a flight path angle of $\gamma_{des} = \frac{\pi}{4}$ rad using which the quadrotor achieves desired Y separation while getting closer to the centroid of the window. Consider Fig. 3.4b; a positive shaping angle is added to the bisector component to shape the desired flight path angle. This corresponds to the shaping angle curve of blue color in the green shaded region shown in Fig. 3.3. The magnitude of the shaping angle reduces to zero when the angular bisector component is zero, and it indicates that the vehicle has arrived at the desired centroid position as shown in Fig. 3.4c. Figure 3.4d illustrates another scenario in which the quadrotor makes elevation angles of $\alpha_1 = \alpha_4 = -\frac{\pi}{2}$ rad, yielding the bisector term $\frac{\alpha_1 + \alpha_4}{2} = -\frac{\pi}{2}$ rad. According to Eq. 3.12c, the shaping angle requirement is $-\frac{\pi}{4}$ rad, which implies $\frac{\alpha_1 + \alpha_4}{2} + S_\gamma < -\frac{\pi}{2}$. This belongs to the point on the red curve in the gray region shown in Fig. 3.3. This will result in a flight path angle of $\gamma_{des} = -\frac{\pi}{4}$ rad according to Eq. (3.12c) using which the quadrotor achieves desired Y separation while getting closer to the centroid of the window.

Remark 3.1 *The desired flight path angle in Eq. (3.12) and shaping angle function in Eq. (3.13) can also be proposed as a function of the elevation angles with respect to the extremities E_2 and E_3 .*

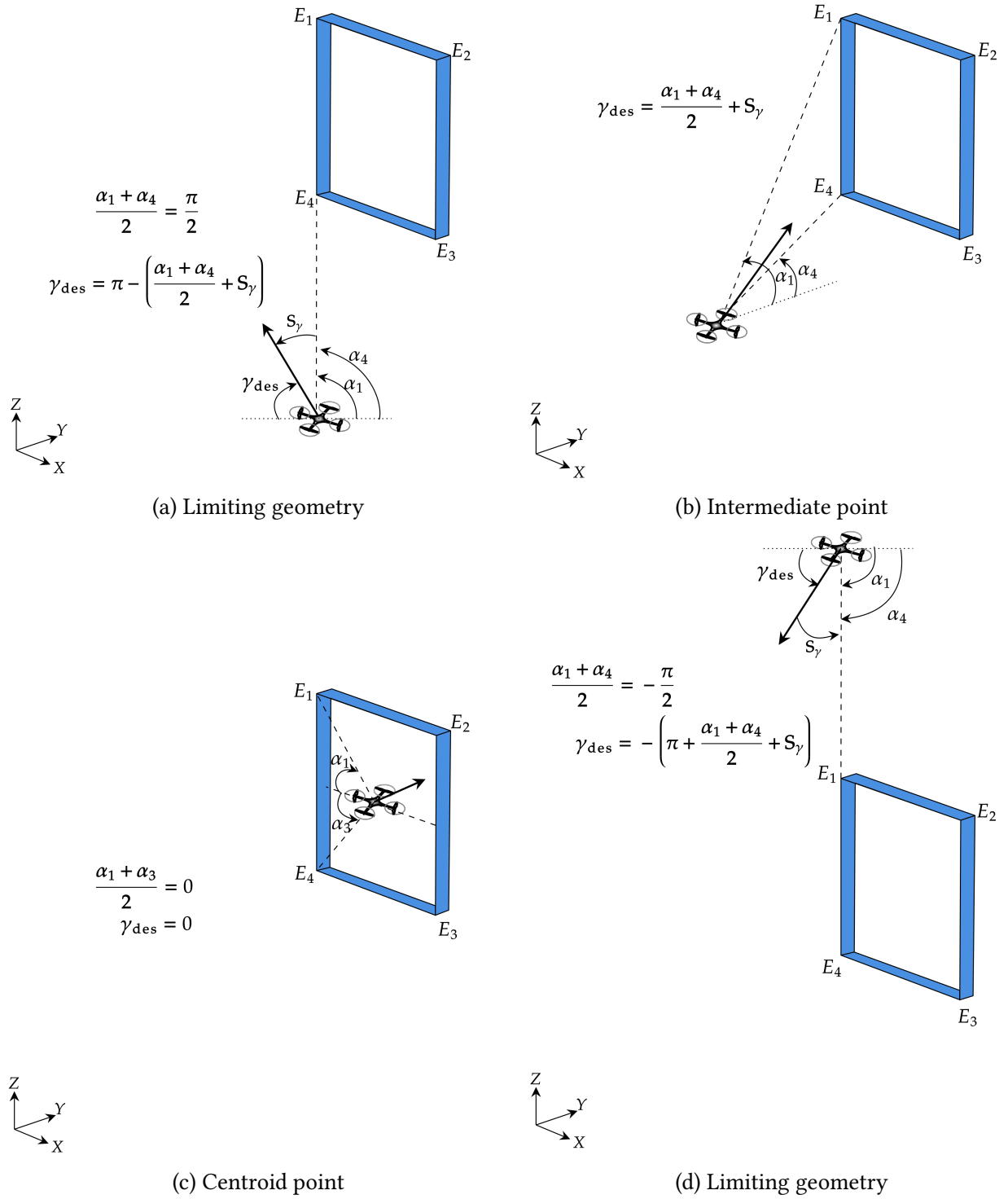


Figure 3.4: Instantaneous desired flight path angle along the guided trajectory

In order to achieve the three-dimensional traversal, a desired heading angle is to be designed along with the desired flight path angle, which is discussed in the subsequent subsection.

3.2.2 Desired heading angle

The desired heading angle using the azimuth angles β_1 and β_2 is proposed as

$$\chi_{des} = \begin{cases} \frac{\beta_1 + \beta_2}{2} + S_\chi & \forall \frac{\alpha_1 + \alpha_4}{2} + S_\gamma \in \left[-\frac{\pi}{2}, \frac{\pi}{2}\right] \\ -\left(\frac{\beta_1 + \beta_2}{2} + S_\chi\right) & \text{otherwise} \end{cases} \quad (3.17a)$$

$$(3.17b)$$

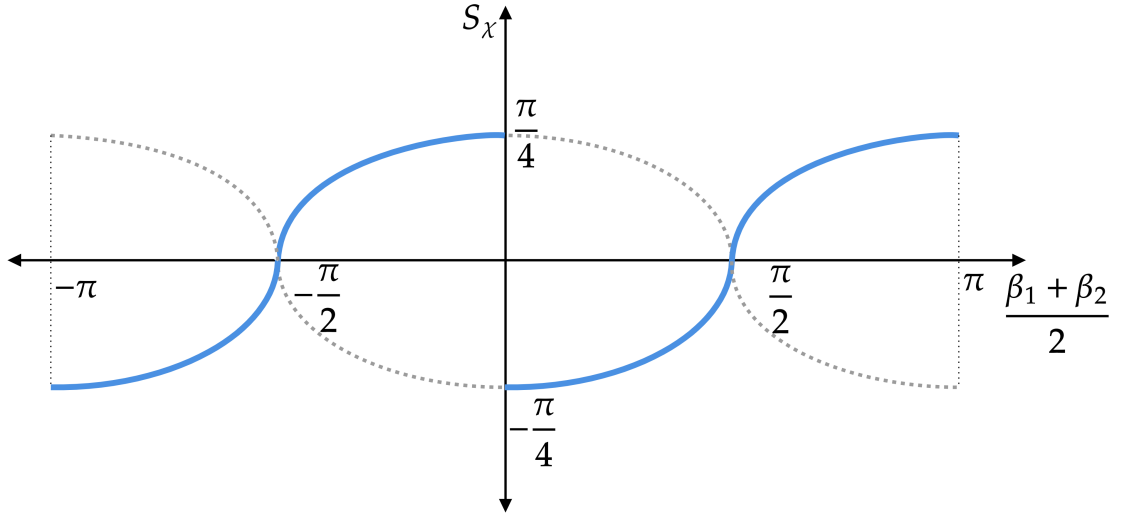
where the term $\frac{\beta_1 + \beta_2}{2}$ represents the angular bisector component and second term S_χ represents the shaping angle component. The key idea behind the proposed desired heading angle is similar to the one discussed in Subsection 2.2 of Chapter 2. The shaping angle term in Eq. (3.17) is given by

$$S_\chi(\beta_1, \beta_2) = \begin{cases} \operatorname{sgn}\left(\frac{\beta_1 + \beta_2}{2} + \frac{\pi}{2}\right) \frac{|\pi^2 - (\beta_1 + \beta_2)^2|^{\frac{1}{2}}}{4}, & \text{for } \beta_1(t), \beta_2(t) \in [-\pi, 0] \\ \operatorname{sgn}\left(\frac{\beta_1 + \beta_2}{2} - \frac{\pi}{2}\right) \frac{|\pi^2 - (\beta_1 + \beta_2)^2|^{\frac{1}{2}}}{4}, & \text{for } \beta_1(t), \beta_2(t) \in (0, \pi) \end{cases} \quad (3.18)$$

The guidance logic employed in the design of desired heading for the vehicle involves directing it towards the window by achieving an equal distance from the window edges $E_1 - E_4$ and $E_2 - E_3$. The shaping angle as governed by Eq. (3.18) and as illustrated in Fig. 3.5 is adjusted in accordance with the angular bisector component to direct the vehicle towards the center of the window.

For the geometries which corresponds to $\frac{\alpha_1 + \alpha_4}{2} + S_\gamma \notin \left[-\frac{\pi}{2}, \frac{\pi}{2}\right]$, that is, the ones characterized by Eqs. (3.12b) and (3.12c), the quadrotor heading direction is evaluated using Eq. (3.17b). This relation Eq. (3.17b) captures the effect of changes required for maintaining $\gamma_{des} \in \left[-\frac{\pi}{2}, \frac{\pi}{2}\right]$ on the $X - Y$ plane.

Remark 3.2 The proposed heading angle as expressed in Eq. (3.17), and the corresponding shaping function described as in Eq. (3.18) can also be formulated as a function of azimuth angles with respect to window extremities E_3 and E_4 .

Figure 3.5: Elliptic shaping angle profile for χ_{des}

3.3 Stability Characteristics

This section discusses the stability characteristics of the proposed guidance strategy followed by phase portrait analysis in the bearing angle space.

Theorem 3.1 *Governed by the system Eqs. (3.4)-(3.9) and (3.12)-(3.18), the vehicle motion is asymptotically stable about the line passing through the centroid of the window and normal to the window plane.*

Proof: Figure 3.6 shows an instantaneous geometry of a quadrotor approaching the window. Let D be the instantaneous distance of the quadrotor from the line normal to the window plane and passing through the centroid. Let D_x and D_z represent the horizontal and vertical displacements of the quadrotor with respect to the normal line, respectively, as shown in Fig. 3.6. Using the geometries depicted in Figs. 3.2 and 3.6 the following relations can be readily deduced,

$$D_x = - \left(R_1 \cos \alpha_1 \cos \beta_1 + \frac{a}{2} \right) \quad (3.19)$$

$$D_z = - \left(R_1 \sin \alpha_1 - \frac{b}{2} \right) \quad (3.20)$$

From Figs. 3.2 and 3.6, the window dimensions a and b can be expressed in terms of line-of-sight distances and bearing angles with respect to extremities E_1 , E_2 , and E_4 as

$$a = R_2 \cos \alpha_2 \cos \beta_2 - R_1 \cos \alpha_1 \cos \beta_1 \quad (3.21)$$

$$b = R_1 \sin \alpha_1 - R_4 \sin \alpha_4 \quad (3.22)$$

Using Eqs (3.21) and (3.22) in Eqs. (3.19) and (3.20) yield

$$D_x = -\frac{1}{2} (R_1 \cos \alpha_1 \cos \beta_1 + R_2 \cos \alpha_2 \cos \beta_2) \quad (3.23)$$

$$D_z = -\frac{1}{2} (R_1 \sin \alpha_1 + R_4 \sin \alpha_4) \quad (3.24)$$

Consider a Lyapunov function

$$W = \frac{1}{2} (D_x^2 + D_z^2) \quad (3.25)$$

Here, $W \geq 0$ for all $(D_x, D_z) \in \mathbb{R}^2$ with $W = 0$ if and only if $D_x = D_z = 0$. Hence the Lyapunov function W is positive definite in the domain \mathbb{R}^2 . Taking the time derivative of the Lyapunov function,

$$\dot{W} = D_x \dot{D}_x + D_z \dot{D}_z \quad (3.26)$$

Differentiating Eq. (3.23) with respect to time,

$$\begin{aligned} \dot{D}_x = \frac{1}{2} \bigg(& -R_1 \dot{\beta}_1 \cos \alpha_1 \sin \beta_1 + \cos \beta_1 \left(-R_1 \dot{\alpha}_1 \sin \alpha_1 + \dot{R}_1 \cos \alpha_1 \right) \\ & -R_2 \dot{\beta}_2 \cos \alpha_2 \sin \beta_2 + \cos \beta_2 \left(-R_2 \dot{\alpha}_2 \sin \alpha_2 + \dot{R}_2 \cos \alpha_2 \right) \bigg) \end{aligned} \quad (3.27)$$

Using Eqs. (3.7)-(3.9), $\gamma = \gamma_{des}$, and $\chi = \chi_{des}$ in Eq. (3.27),

$$\dot{D}_x = V \cos \gamma_{des} \cos \chi_{des} \quad (3.28)$$

Differentiating Eq. (3.24) with respect to time,

$$\dot{D}_z = \frac{1}{2} \left(R_1 \dot{\alpha}_1 \cos \alpha_1 + \dot{R}_1 \sin \alpha_1 + R_4 \dot{\alpha}_3 \cos \alpha_4 + \dot{R}_3 \sin \alpha_4 \right) \quad (3.29)$$

Using Eqs. (3.7)-(3.9) and $\gamma = \gamma_{des}$ in Eq. (3.29),

$$\dot{D}_z = V \sin \gamma_{des} \quad (3.30)$$

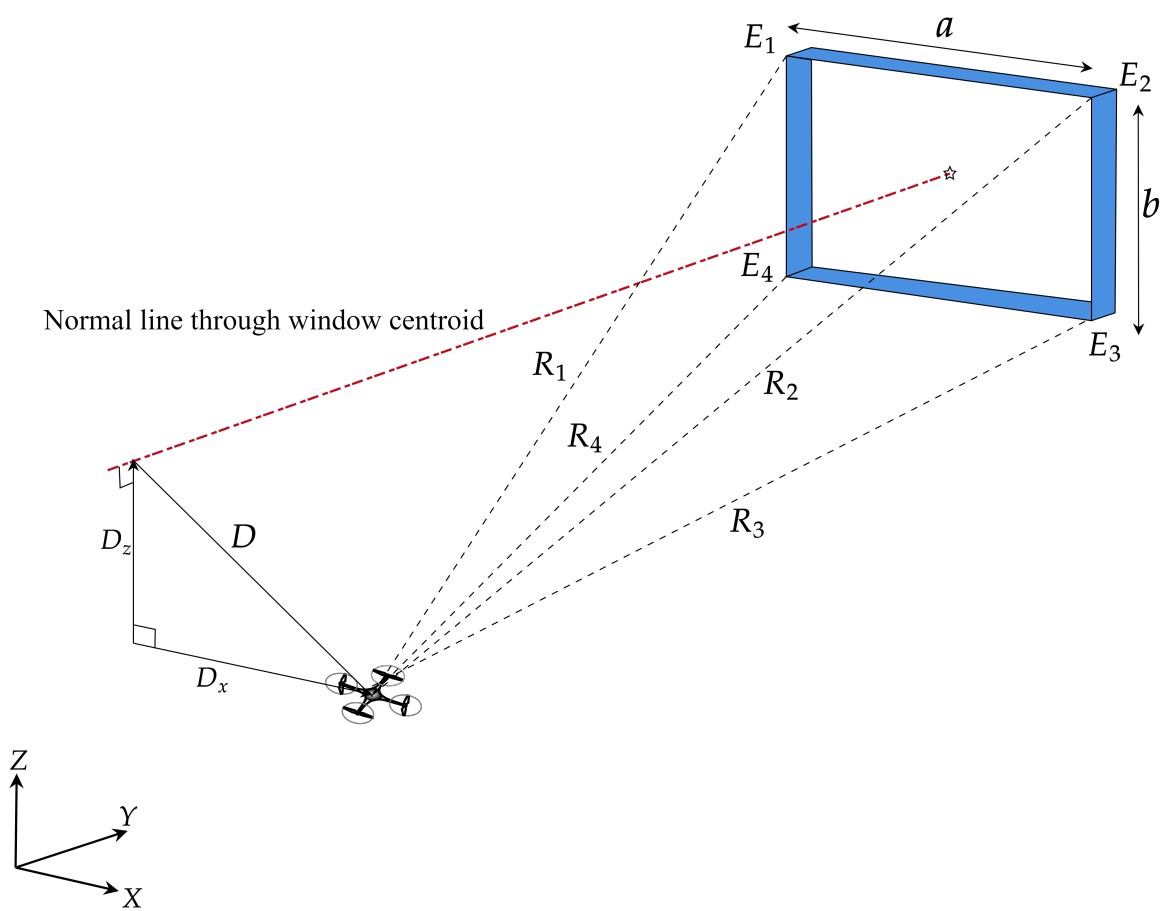


Figure 3.6: Instantaneous geometry of quadrotor moving towards the window

Using Eqs. (3.28) and (3.30) in Eq. (3.26),

$$\dot{W} = D_x V \cos \gamma_{des} \cos \chi_{des} + D_z V \sin \gamma_{des} \quad (3.31)$$

From the relative geometries in Figs. 3.7a and 3.7b, it can be noted that

$$\frac{\cos \alpha_1}{\cos \alpha_4} = \frac{R_4}{R_1} \quad (3.32)$$

$$\frac{R_1 \cos \alpha_1}{R_2 \cos \alpha_2} = \frac{\sin \beta_2}{\sin \beta_1} \quad (3.33)$$

Rest of the analysis divided into four quadrants around the centroid of the window as follows

1. Case 1: $D_z < 0$ and $D_x < 0$

From Eq. (3.24), when $D_z < 0$

$$R_1 \sin \alpha_1 + R_4 \sin \alpha_4 > 0 \quad (3.34)$$

which implies

$$\frac{R_1}{R_4} \sin \alpha_1 + \sin \alpha_4 > 0 \quad (3.35)$$

Using Eq. (3.32) in Eq. (3.35) with $D_z < 0$,

$$\begin{aligned} &\implies \frac{\cos \alpha_4}{\cos \alpha_1} \sin \alpha_1 + \sin \alpha_4 > 0 \\ &\implies \cos \alpha_4 \sin \alpha_1 + \sin \alpha_4 \cos \alpha_1 > 0 \\ &\implies \sin(\alpha_1 + \alpha_4) > 0 \end{aligned}$$

which implies

$$\frac{\alpha_1 + \alpha_4}{2} \in \left(0, \frac{\pi}{2}\right) \quad \forall D_z < 0 \quad (3.36)$$

From the proposed guidance command Eq. (3.12), it can be deduced that

$$\gamma_{des} \in \left(0, \frac{\pi}{2}\right) \quad \forall \frac{\alpha_1 + \alpha_4}{2} \in \left(0, \frac{\pi}{2}\right) \quad (3.37)$$

From Eq. (3.23), when $D_x < 0$

$$R_1 \cos \alpha_1 \cos \beta_1 + R_2 \cos \alpha_2 \cos \beta_2 > 0 \quad (3.38)$$

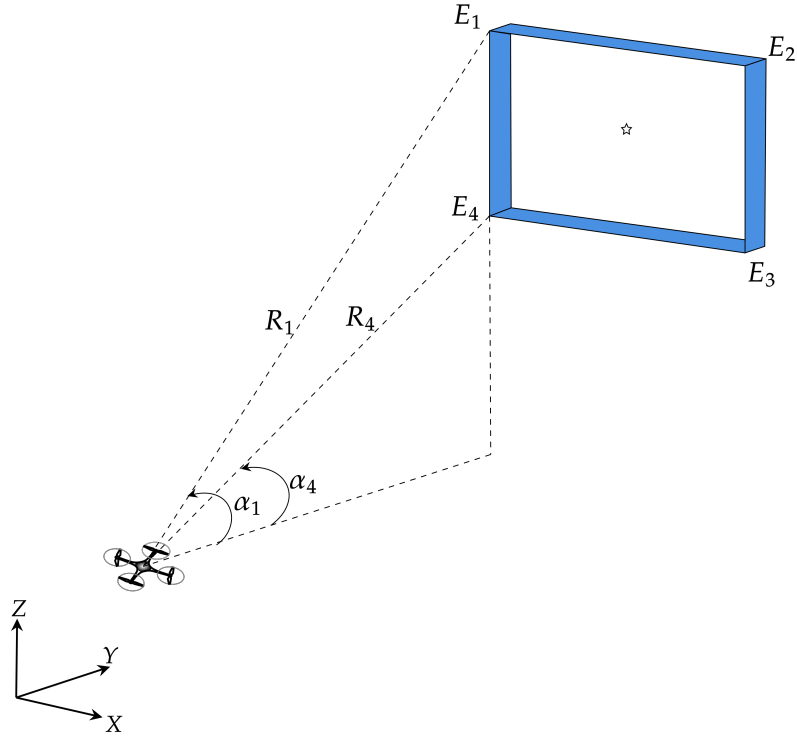
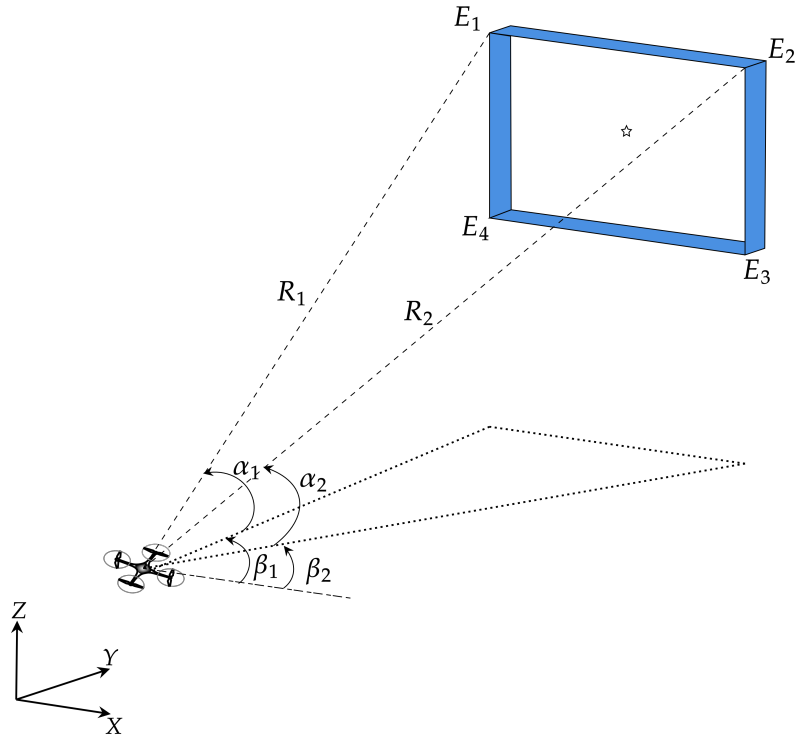
(a) Relative geometry with respect to E_1 and E_4 (b) Relative geometry with respect to E_1 and E_2

Figure 3.7: Relative geometries with respect to the window extremities

which implies

$$\frac{R_1 \cos \alpha_1}{R_2 \cos \alpha_2} \cos \beta_1 + \cos \beta_2 > 0 \quad (3.39)$$

Using Eq. (3.33) in Eq. (3.39) with $D_x < 0$,

$$\begin{aligned} &\implies \frac{\sin \beta_2}{\sin \beta_1} \cos \beta_1 + \cos \beta_2 > 0 \\ &\implies \sin \beta_2 \cos \beta_1 + \sin \beta_1 \cos \beta_1 > 0 \\ &\implies \sin(\beta_1 + \beta_2) > 0 \end{aligned}$$

which implies

$$\frac{\beta_1 + \beta_2}{2} \in \left(0, \frac{\pi}{2}\right) \quad \forall D_x < 0 \quad (3.40)$$

From the proposed guidance command Eq. (3.17), it can be deduced that

$$\chi_{des} \in \left(-\frac{\pi}{2}, \frac{\pi}{2}\right) \quad \forall \frac{\beta_1 + \beta_2}{2} \in \left(0, \frac{\pi}{2}\right) \quad (3.41)$$

Using Eqs. (3.37) and (3.41) in Eq. (3.31)

$$\dot{W} < 0 \quad \forall D_z < 0, D_x < 0 \quad (3.42)$$

2. Case 2: $D_z > 0$ and $D_x > 0$

From Eq. (3.24), when $D_z > 0$

$$R_1 \sin \alpha_1 + R_4 \sin \alpha_4 < 0 \quad (3.43)$$

which implies

$$\frac{R_1}{R_4} \sin \alpha_1 + \sin \alpha_4 < 0 \quad (3.44)$$

Using Eq. (3.32) in Eq. (3.44) with $D_z > 0$,

$$\begin{aligned} &\implies \frac{\cos \alpha_4}{\cos \alpha_1} \sin \alpha_1 + \sin \alpha_4 < 0 \\ &\implies \cos \alpha_4 \sin \alpha_1 + \sin \alpha_4 \cos \alpha_1 < 0 \\ &\implies \sin(\alpha_1 + \alpha_4) < 0 \end{aligned}$$

which implies

$$\frac{\alpha_1 + \alpha_4}{2} \in \left(-\frac{\pi}{2}, 0\right) \quad \forall D_z > 0 \quad (3.45)$$

From the proposed guidance command Eq. (3.12), it can be deduced that

$$\gamma_{des} \in \left(-\frac{\pi}{2}, 0\right) \quad \forall \frac{\alpha_1 + \alpha_4}{2} \in \left(-\frac{\pi}{2}, 0\right) \quad (3.46)$$

From Eq. (3.23), when $D_x > 0$

$$R_1 \cos \alpha_1 \cos \beta_1 + R_2 \cos \alpha_2 \cos \beta_2 < 0 \quad (3.47)$$

which implies

$$\frac{R_1 \cos \alpha_1}{R_2 \cos \alpha_2} \cos \beta_1 + \cos \beta_2 < 0 \quad (3.48)$$

Using Eq. (3.33) in Eq. (3.48) with $D_x > 0$,

$$\begin{aligned} &\implies \frac{\sin \beta_2}{\sin \beta_1} \cos \beta_1 + \cos \beta_2 < 0 \\ &\implies \sin \beta_2 \cos \beta_1 + \sin \beta_1 \cos \beta_2 < 0 \\ &\implies \sin(\beta_1 + \beta_2) < 0 \end{aligned}$$

which implies

$$\frac{\beta_1 + \beta_2}{2} \in \left(\frac{\pi}{2}, \pi\right) \quad \forall D_x > 0 \quad (3.49)$$

From the proposed guidance command Eq. (3.17), it can be deduced that

$$\chi_{des} \in \left(\frac{\pi}{2}, \pi\right] \cup \left(-\pi, -\frac{\pi}{2}\right) \quad \forall \frac{\beta_1 + \beta_2}{2} \in \left(\frac{\pi}{2}, \pi\right) \quad (3.50)$$

Using Eqs. (3.46) and (3.50) in Eq. (3.31)

$$\dot{W} < 0 \quad \forall D_z > 0, D_x > 0 \quad (3.51)$$

3. Case 3: $D_z < 0$ and $D_x > 0$

Using Eqs. (3.36) and (3.49) in proposed guidance command Eqs. (3.12) and (3.17), it can be deduced that

$$\gamma_{des} \in \left(0, \frac{\pi}{2}\right) \quad \forall \frac{\alpha_1 + \alpha_4}{2} \in \left(0, \frac{\pi}{2}\right) \quad (3.52)$$

$$\chi_{des} \in \left(\frac{\pi}{2}, \pi\right] \cup \left(-\pi, -\frac{\pi}{2}\right) \quad \forall \frac{\beta_1 + \beta_2}{2} \in \left(\frac{\pi}{2}, \pi\right) \quad (3.53)$$

Using Eqs. (3.52) and (3.53) in Eq. (3.31)

$$\dot{W} < 0 \quad \forall D_z < 0, D_x > 0 \quad (3.54)$$

4. Case 4: $D_z > 0$ and $D_x < 0$

Using Eqs. (3.40) and (3.45) in proposed guidance command Eqs. (3.12) and (3.17), it can be deduced that

$$\gamma_{des} \in \left(-\frac{\pi}{2}, 0\right) \quad \forall \frac{\alpha_1 + \alpha_4}{2} \in \left(-\frac{\pi}{2}, 0\right) \quad (3.55)$$

$$\chi_{des} \in \left(-\frac{\pi}{2}, \frac{\pi}{2}\right) \quad \forall \frac{\beta_1 + \beta_2}{2} \in \left(0, \frac{\pi}{2}\right) \quad (3.56)$$

Using Eqs. (3.56) and (3.55) in Eq. (3.31),

$$\dot{W} < 0 \quad \forall D_z > 0, D_x < 0 \quad (3.57)$$

From Eqs. (3.31), (3.42), (3.51), (3.54) and (3.57), it can be deduced that

$$\dot{W} \leq 0 \quad \forall (D_x, D_z) \in \mathbb{R}^2 \quad (3.58)$$

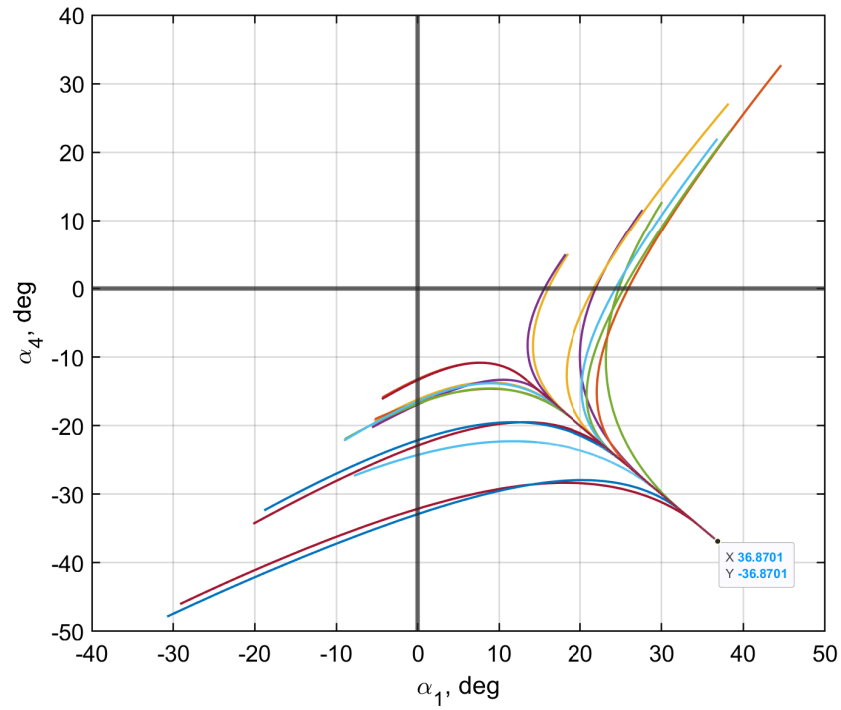
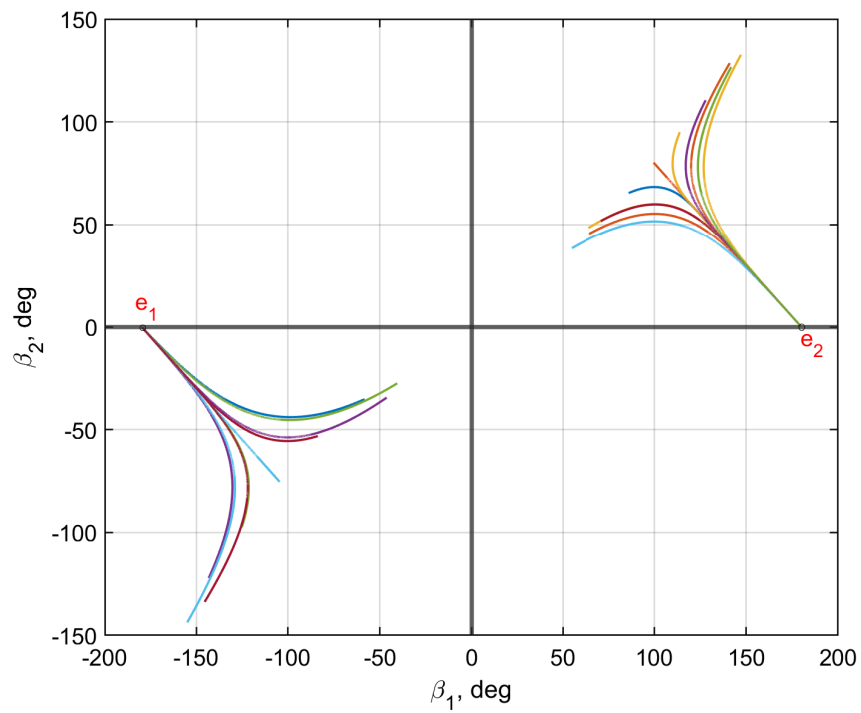
$$\dot{W} = 0 \quad \text{at } D_x = 0, D_z = 0 \quad (3.59)$$

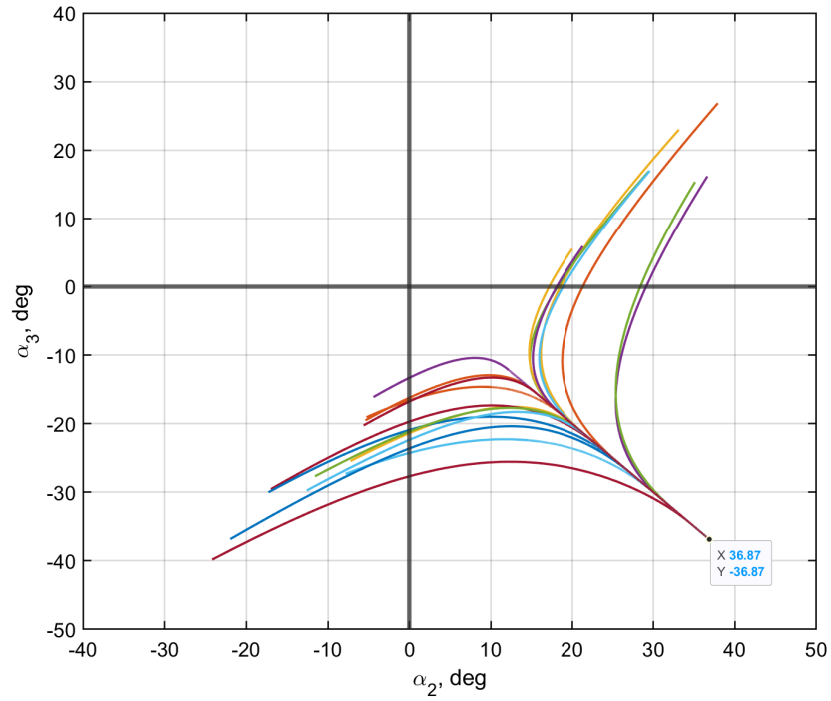
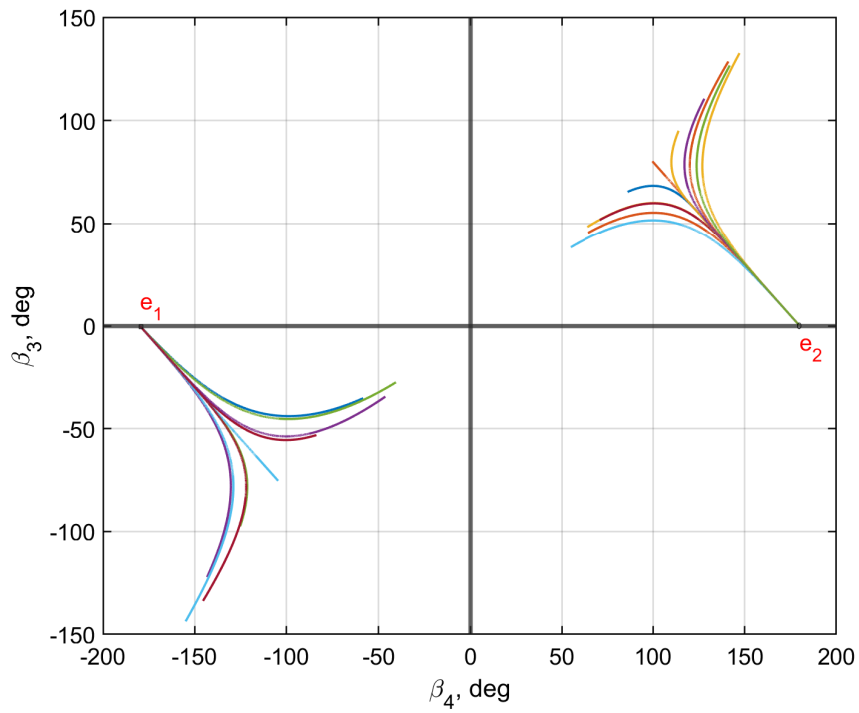
□

3.3.1 Phase plane analysis

In this section, we further analyze the behavior of the system described by the Eqs. (3.4)-(3.6) under the proposed guidance commands given by Eqs. (3.12) and (3.17), where χ and γ take their desired values. The analysis is carried out for a window of dimension of $a = 4$ m and $b = 3$ m. Considering the system states as α_1 , α_4 , β_1 and β_2 , phase portraits are generated by numerically solving system Eqs. (3.4)-(3.6) for various initial conditions $\alpha_1(t_i), \alpha_4(t_i) \in [-\frac{\pi}{2}, \frac{\pi}{2}]$ and $\beta_1(t_i), \beta_2(t_i) \in [-\pi, \pi)$. The resulting phase portraits are shown in Fig. 3.8.

The analysis shows that the system states $(\alpha_1(t), \alpha_4(t))$ reach to their desired final point of $(36.87, -36.87)$ deg, as illustrated in Fig. 3.8a. The elevation angles reach their desired values of $\alpha_1(t_T) = -\alpha_4(t_T) = 36.87$ deg, as in Eq. (3.11), indicating a successful window traversal. Furthermore, we analyze the trajectories of the system in the $\beta_1 - \beta_2$ plane, shown in Fig. 3.8b. All the trajectories converge to one of the two desired points $e_1 = (-180, 0)$ deg or $e_2 = (180, 0)$ deg, as in Eq. (3.10), indicating the final desired state of traversal. A similar phase portrait behavior in $\alpha_2 - \alpha_3$ and $\beta_4 - \beta_3$ plane can be seen in Figs. 3.9a and 3.9b. It is

(a) Phase portraits in $\alpha_1 - \alpha_4$ plane.(b) Phase portraits in $\beta_1 - \beta_2$ plane.Figure 3.8: Phase plane analysis in $\alpha_1 - \alpha_4$ and $\beta_1 - \beta_2$ planes

(a) Phase portraits in $\alpha_2 - \alpha_3$ plane.(b) Phase portraits in $\beta_4 - \beta_3$ plane.Figure 3.9: Phase plane analysis in $\alpha_2 - \alpha_3$ and $\beta_4 - \beta_3$ planes.

to be noted that in the planes considered, few trajectories seem to be intersecting. However, the three-dimensional vehicle trajectories are distinct and non-intersecting for different initial conditions, while the projections may not always indicate that.

3.4 Trajectory Generation and Control

This section presents the guided trajectory generation and the control architecture of the quadrotor. The desired velocity components (v_{xdes} , v_{ydes} , v_{zdes}) are generated using Eqs. (3.4)-

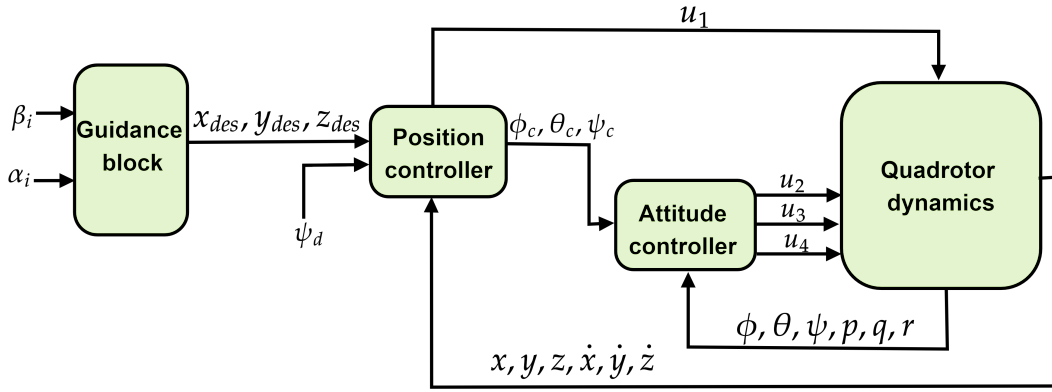


Figure 3.10: Guided trajectory generation and control architecture

(3.6) as

$$v_{xdes}(t) = V \cos \gamma_{des}(t) \cos \chi_{des}(t) \quad (3.60)$$

$$v_{ydes}(t) = V \cos \gamma_{des}(t) \sin \chi_{des}(t) \quad (3.61)$$

$$v_{zdes}(t) = V \sin \gamma_{des}(t) \quad (3.62)$$

Using Eqs. (3.60)-(3.62) the desired position (x_{des} , y_{des} , z_{des}) can be generated as

$$x_{des} = x(t_i) + \int_{t_i}^t v_{xdes}(t) dt \quad (3.63)$$

$$y_{des} = y(t_i) + \int_{t_i}^t v_{ydes}(t) dt \quad (3.64)$$

$$z_{des} = z(t_i) + \int_{t_i}^t v_{zdes}(t) dt \quad (3.65)$$

where $(x(t_i), y(t_i), z(t_i)) \in \mathbb{R}^3$ represent the initial position coordinate of the quadrotor in world frame. The control architecture of the quadrotor is illustrated in Fig. 3.10, where the desired trajectories are generated through the guidance block utilizing bearing angle information.

As discussed in Subsection 2.4.2 of Chapter 2, the desired position Eqs. (3.63)-(3.65) and its derivatives Eqs. (3.60)-(3.62) can be related to the control inputs u_1 , u_2 , u_3 , and u_4 through control relations Eqs. (3.66)-(3.69).

$$u_1 = m(g + K_{dz}(v_{zdes} - \dot{z}) + K_{pz}(z_{des} - z)) \quad (3.66)$$

$$u_2 = K_{d\phi}(p_c - p) + K_{p\phi}(\phi_c - \phi) \quad (3.67)$$

$$u_3 = K_{d\theta}(q_c - q) + K_{p\theta}(\theta_c - \theta) \quad (3.68)$$

$$u_4 = K_{d\psi}(r_c - r) + K_{p\psi}(\psi_c - \psi) \quad (3.69)$$

Here, (K_{dz}, K_{pz}) , $(K_{d\phi}, K_{p\phi})$, $(K_{d\theta}, K_{p\theta})$, and $(K_{d\psi}, K_{p\psi})$ represent the tunable controller gains for u_1 , u_2 , u_3 , and u_4 , respectively, and the commanded angular velocity components (p_c, q_c, r_c) are computed using the derivatives of commanded attitude angles $(\dot{\phi}_c, \dot{\theta}_c, \dot{\psi}_c)$ using Eq. (2.45).

3.5 Qualitative Comparison with Existing Works

A qualitative comparison study is carried out with existing gap traversal methods. Existing and proposed traversal strategies presented in Chapters 2 and 3 are compared with respect to gap information required and the computation involved in generating a safe trajectory. The comparative summary is presented in Table 3.1.

It can be noted that, in terms of the gap information, the proposed methods would require only an edge detection algorithm that can run on a binary image. This is in contrast to either complete prior information of the gap in the world frame or depth information of the gap. In addition, the proposed trajectory planning guidance commands offer a simple easy-to-implement analytic form that does not require iterations or numerical solutions.

Table 3.1: Qualitative comparison study

Methods	Gap information	Trajectory planning computations
Mellinger et al. [21]	Dimension of the gap in the world frame.	Instantaneous vehicle position, and velocity components are computed with backward integration of equation of motion considering known final goal point and arrival time.
Mellinger et al. [22]	Dimension of the gap in the world frame.	Computation of time parameterized optimal trajectory through a series of known waypoints with gap dimension constraints. Numerical solution of the optimization problem using Quadratic programming.
Saurabh et al. [23]	Gap vertices in the world frame.	Computation of six coefficients, two each for defining instantaneous desired position in 3-D.
Falanga et al. [26]	Gap centroid is computed using 8 feature points in the image, depth information.	Computation of time parameterized second order position and velocity profile passing through center of the gap. Numerical solution for trajectory parameters using Sequential Quadratic Programming (SQP).
Guo et al. [27]	Desired images of the gap need to be taken and stored before hand for comparison with instantaneous images, additional depth information for translation variables.	Image-based trajectory planning in terms of invariant image features and heading angle. Quadratic program based solution for minimum snap of translation between current image and desired image.
Proposed method	Bearing information of the gap boundary which can be obtained using edge detection algorithms followed by resolution of the obtained gap bearing information in horizontal plane.	Trajectory generation using simpler closed-form analytic guidance commands of Eqs. (2.8), (3.12) and (3.17).

3.6 Numerical Simulation Results

Numerical simulations are carried out to evaluate the performance of the proposed method using a 6-DOF quadrotor model with mass and moment of inertia properties described in Section 2.5 of Chapter 2. A window with dimensions $a = 2$ m and $b = 3$ m with edges $E_1 = (7, 10, 10)$ m, $E_2 = (9, 10, 10)$ m, $E_3 = (9, 10, 7)$ m, and $E_4 = (7, 10, 7)$ m, is considered. The centroid of the window is $W_c = (8, 10, 8.5)$ m, which is the desired traversal point. The quadrotor traversal speed is chosen as $V = 1$ m/s. All simulations use desired yaw angle $\psi_{des} = 0$ deg and initial velocity of 0 m/s. The controller gains for position and attitude control are selected as $K_{pz} = 3.8$, $K_{dz} = 3.5$, $K_{py} = 12.7$, $K_{dy} = 4.2$, $K_{px} = 6$, $K_{dx} = 3.5$, $K_{pjx} = 6$, $K_{dix} = 3.5$, $K_{pjiy} = 12.7$, $K_{djiy} = 4.2$, $K_{p\phi} = 12.8$, $K_{d\phi} = 0.5$, $K_{p\theta} = 1.8$, $K_{d\theta} = 0.2$, $K_{p\psi} = 2$, and $K_{d\psi} = 0.5$. Once the traversal condition (3.10) is met, the guidance commands follow their already achieved heading angle $\chi_{des} = \frac{\pi}{2}$ rad and flight path angle $\gamma_{des} = 0$ rad. The commanded roll and pitch angles are saturated to be within ± 20 deg.

3.6.1 Case 1. Sample window traversal scenario with noise-free bearing information

This case considers the trajectory generation using noise-free bearing angles α_1 , α_4 , β_1 , and β_2 , respectively. The initial position of the quadrotor is set to $(14, 2, 0)$ m. The quadrotor successfully traverses through the desired traversal point $T(8, 10, 8.5)$ m at 15.43 s, as shown in Fig. 3.11. The angular bisector of elevation angles $(\frac{\alpha_1 + \alpha_4}{2})$ reaches its final desired state of 0 deg at 13.5 s, as shown in Figs. 3.12a. Similarly, the angular bisector of azimuth angles $(\frac{\beta_1 + \beta_2}{2})$ achieves the desired value of $\frac{\pi}{2}$ rad at 13.63 s, as illustrated in Fig. 3.12b. In Fig. 3.12c, the variation of shaping angle component for γ_{des} is plotted against its angular bisector component. In accordance with Eq. (3.13), the shaping component monotonically decreases to zero when the angular bisector component reaches zero, leading to the desired traversal. Additionally, the variation of the shaping angle component for the χ_{des} is plotted against its angular bisector component in Fig. 3.12d. The shaping component attains zero when the desired angular bisector of $\frac{\pi}{2}$ rad is achieved. The roll and pitch responses of the quadrotor are illustrated in Figs. 3.13a and 3.13b, respectively. The velocity response of the quadrotor

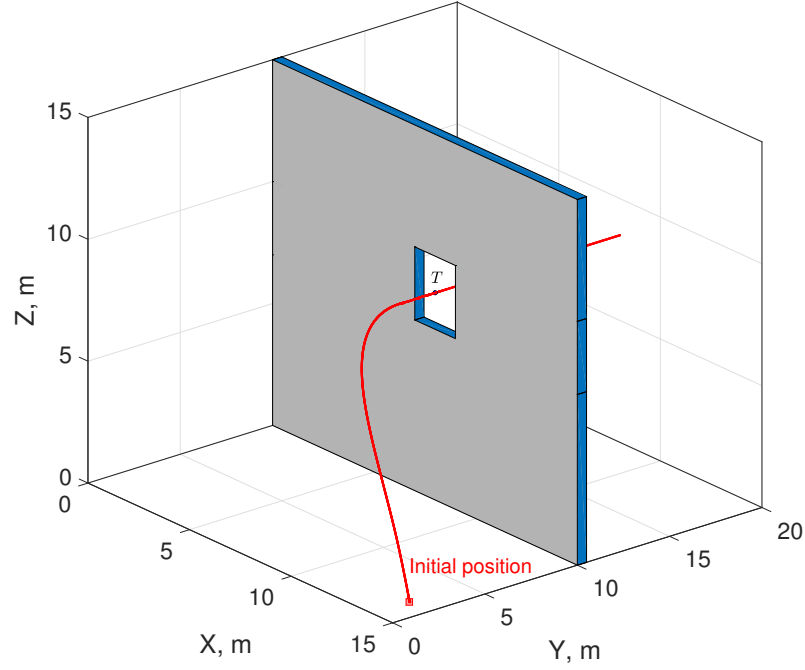
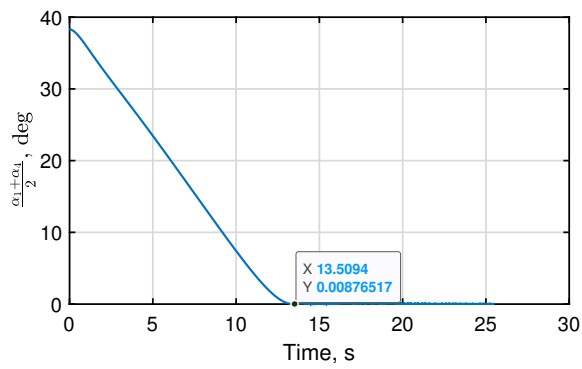


Figure 3.11: Quadrotor trajectory of Case 1

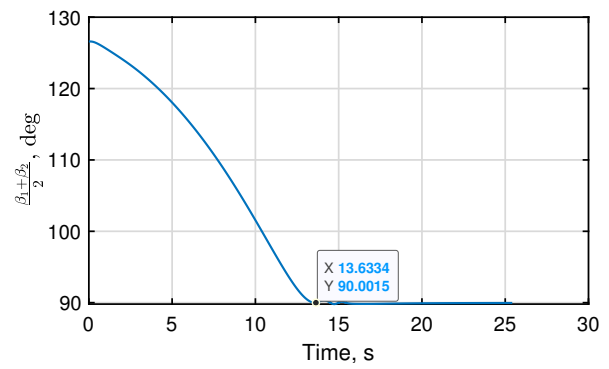
shown in Fig. 3.13c indicates that the traversal speed of 1 m/s is achieved at 3.75 s.

3.6.2 Case 2. Effect of noise in bearing information

This case study investigates the performance of proposed guidance method when the bearing angle information is corrupted by noise. The noisy bearing measurements are generated by adding zero mean Gaussian-noise to the true values. That is, $\alpha_{im}(t) = \alpha_i(t) + \mathcal{N}(0, \sigma^2)$, and $\beta_{im}(t) = \beta_i(t) + \mathcal{N}(0, \sigma^2)$, where α_{im} and β_{im} are the noisy bearing measurements. Here, σ is the standard deviations associated with the noise. The robustness of the guidance method is studied with respect of unfiltered α_{im} and β_{im} utilized in the proposed guidance commands of Eqs. (3.12) and (3.17). The initial conditions and window geometry are identical to the ones considered in Case 1. This case study considers the standard deviation of $\sigma = 4$ deg. The quadrotor trajectory plotted in Fig. 3.14, indicates a safe traversal of the quadrotor through the window. True values and measured values of the elevation angles and azimuth angles are plotted in Figs. 3.15a and 3.15b, respectively. The vehicle distance from the centroid of the



(a) Angular bisector of elevation angles.



(b) Angular bisector of azimuth angles

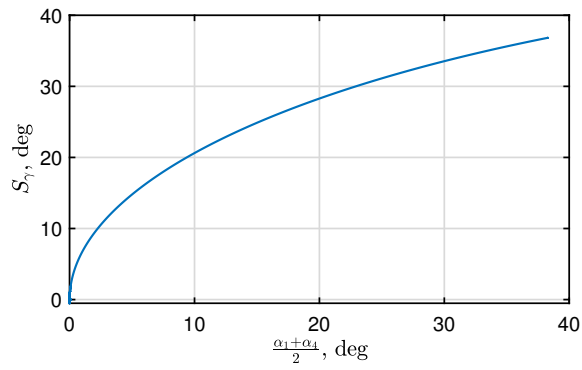
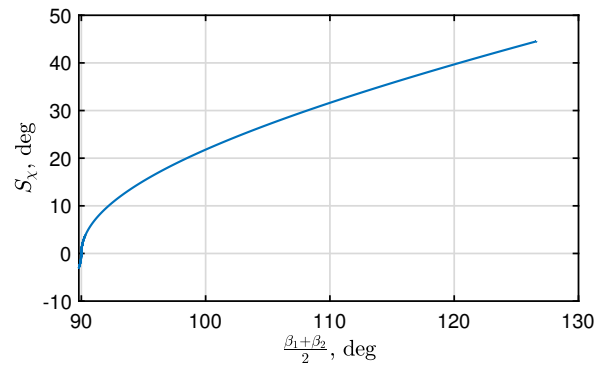
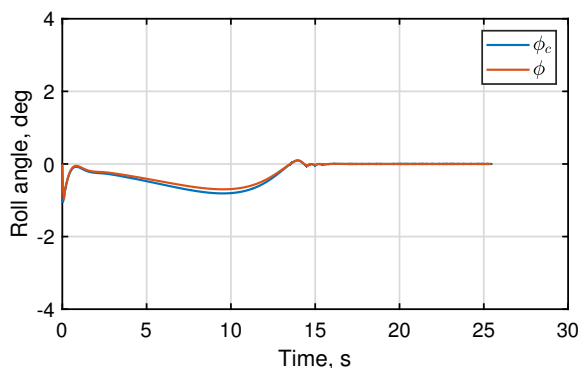
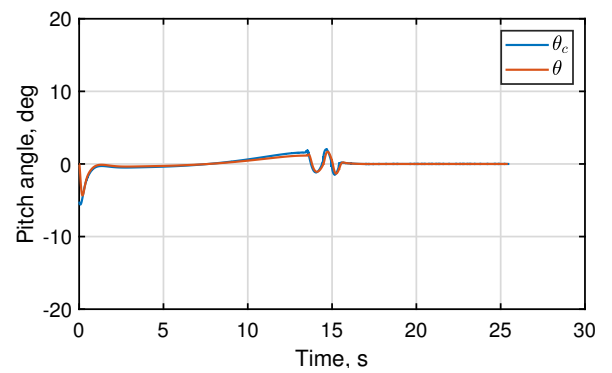
(c) Shaping angle component for γ_{des} (d) Shaping angle component for χ_{des}

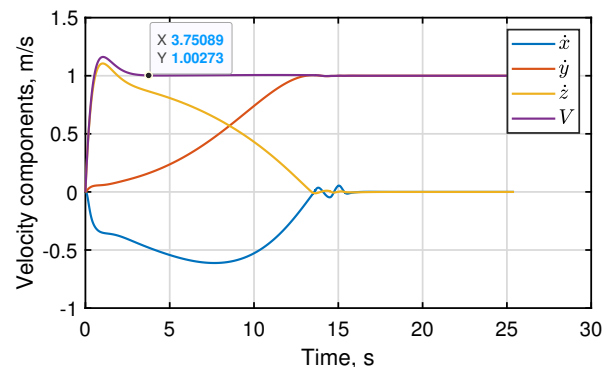
Figure 3.12: Results for Case 1



(a) Roll angle response.



(b) Pitch angle response



(c) Velocity components of the quadrotor

Figure 3.13: Results for Case 1

window is shown in Fig. 3.15c, which indicates that the quadrotor reaches the traversal point with a negligible error of $\Delta = 0.013$ m from its desired value. Here, $\Delta = \|T - W_c\|$ denotes the distance between the traversal point and centroid of the window.

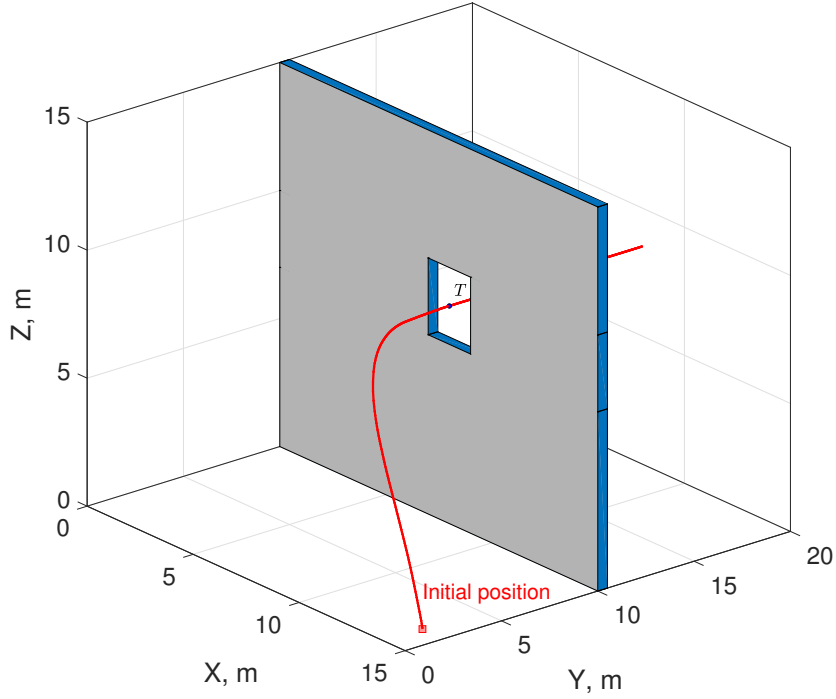
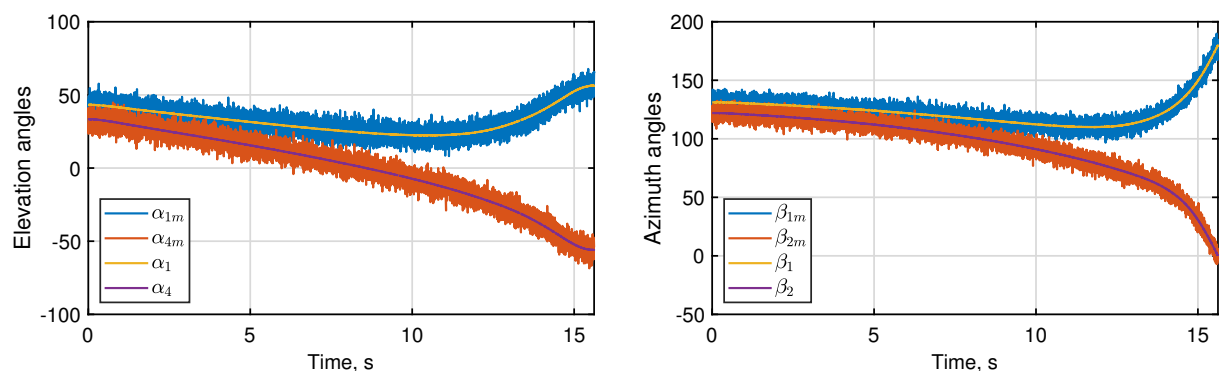


Figure 3.14: Quadrotor trajectory for Case 2

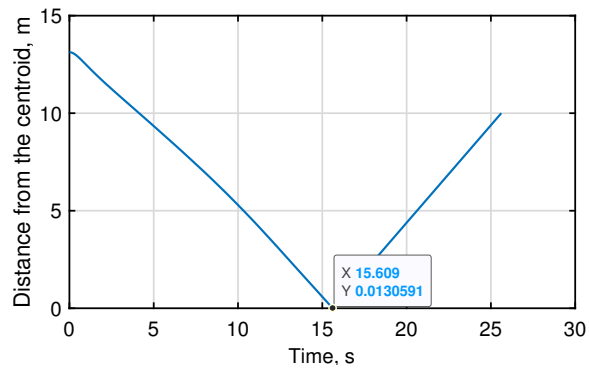
3.6.3 Case 3: Various initial conditions and noisy measurements

A Monte-Carlo simulation is carried out for 100 initial conditions, for a specified noise distribution. With uniform distribution, the initial conditions satisfy $x(t_i) \in [0, 20]$ m, $y(t_i) \in [0, 9]$ m, and $z(t_i) \in [0, 20]$ m, respectively. The bearing measurements are corrupted by noise with its characteristics identical to those considered in Case 2 with $\sigma = 1, 2, \dots, 7$ deg. The performance of the proposed method is evaluated by examining the distance between the quadrotor traversal point from its desired point. The statistical results for specified noise distribution are illustrated in Table. 3.2. The mean and standard deviation results indicate a negligible deterioration in the performance. Figure 3.16 presents twenty of randomly selected trajectories from the study. This case study demonstrates the robustness of the proposed method with respect



(a) Elevation angles.

(b) Azimuth angles



(c) Distance from the centroid of the window

Figure 3.15: Results for Case 2

Table 3.2: Statistical results of Case 3

Bearing measurement noise $\mathcal{N}(\text{mean, standard deviation}(\text{deg.})^2)$	Distance between traversal point and centroid (m)	
	Mean	Standard deviation
$\mathcal{N}(0, 1^2)$	0.0213	0.0627
$\mathcal{N}(0, 2^2)$	0.0381	0.1417
$\mathcal{N}(0, 3^2)$	0.0578	0.2289
$\mathcal{N}(0, 4^2)$	0.0514	0.2157
$\mathcal{N}(0, 5^2)$	0.0452	0.1185
$\mathcal{N}(0, 6^2)$	0.0526	0.1627
$\mathcal{N}(0, 7^2)$	0.0683	0.2556

to the quadrotor's initial points.

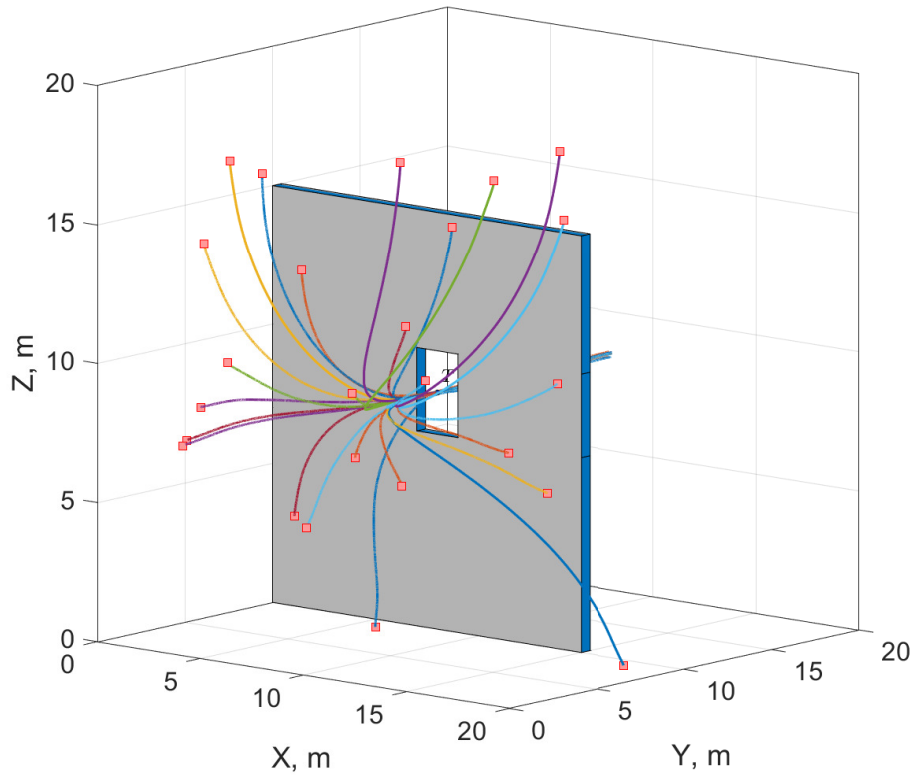


Figure 3.16: Quadrotor trajectories of Case 3

3.7 Summary

This chapter proposed a novel guidance solution to the problem of quadrotor window traversal using bearing-only information of window extremities. The desired trajectory is generated using two distinct proposed guidance commands, which include a desired flight path angle and a desired heading angle. These commands comprise an angular bisector component and an elliptical shaping function, dynamically responding to instantaneous bearing angle values. The proposed guidance commands generate a desired trajectory based on the instantaneous bearing angle values, with elevation and azimuth angles directing the desired flight path angle and heading direction for the traversal. Stability analysis and phase plane analysis confirm the guaranteed traversal capability of the proposed guidance method. The proposed method is applied to a 6-degree-of-freedom quadrotor by considering dynamic attitude constraints and noise in the bearing information. Monte-Carlo simulation with various initial conditions demonstrates the robustness of the proposed method.

Chapter 4

Guidance Framework for Lane Transition in Air Corridors

This chapter presents a new lane transition guidance method for a quadrotor flying in an air corridor system. The proposed method comprises three guidance phases: a discerning guidance phase for determining velocity of the neighboring vehicles, a longitudinal guidance phase for identifying an appropriate gap in the destination lane, and a transit guidance phase for maneuvering to the desired gap. Local asymptotic stability is ascertained for the proposed guidance phases. Simulation results and the Monte Carlo test demonstrate the feasibility, effectiveness, and robustness of the proposed method for safe autonomous lane transition.

4.1 Problem Formulation

Consider a two-dimensional air corridor UAV mobility system with a representative traffic lane and a service lane, as shown in Fig. 4.1. Traffic lane is a relatively busy segment with quadrotors moving along the prescribed traffic direction. Service lane can be used by quadrotors trying to gain access to the traffic lane. Figure 4.1 shows a typical lane transition scenario where the ego vehicle tries to join the main traffic starting from a given position in the service lane. The lanes in the air corridor are assumed to be operating at constant altitude levels. It is assumed that vehicles in the traffic lane move with a specified constant speed v_t . This helps in maintaining a constant safe separation between vehicles moving in the traffic lane. As a virtue of the corridor architecture, the lateral separation between the lanes d is a constant, and this information is available to the vehicles using the corridor. We consider a local planning sce-

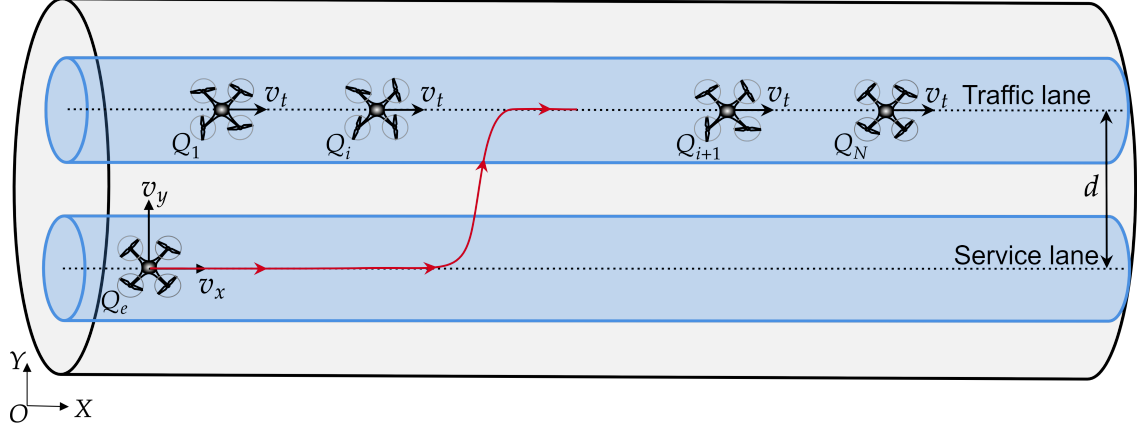


Figure 4.1: Lane transition scenario in an air corridor

nario where, using vision sensors, the ego vehicle has the relative bearing information of the immediate neighboring vehicles in the traffic lane. A fixed reference frame is considered with its X -axis parallel to the corridor lanes. The guidance objective here is to command the ego vehicle's longitudinal and lateral motion for identifying a suitable gap in the traffic lane and moving into it.

4.2 Proposed Lane Transition Guidance Method

Consider the instantaneous geometry between the ego vehicle and a neighboring vehicle in the traffic lane, as shown in Fig. 4.2. Here, Q_e represents the ego vehicle, and Q_i (for $i = 1, 2, \dots, N$) denotes the i^{th} vehicle in the traffic lane. The variables x_e , y_e , and χ_e represent the longitudinal position, lateral position, and the heading angle with respect to the positive X -axis of the ego vehicle, respectively. The kinematic equations of motion for point object ego vehicle are given by

$$\dot{x}_e(t) = v_x(t) = v_e(t) \cos \chi_e(t) \quad (4.1)$$

$$\dot{y}_e(t) = v_y(t) = v_e(t) \sin \chi_e(t) \quad (4.2)$$

where v_e represents the total velocity and v_x , v_y are the velocity components along the longitudinal and lateral directions, respectively. Using Eqs. (4.1) and (4.2), the total speed and

heading of the ego vehicle can be expressed as

$$v_e = (v_x^2 + v_y^2)^{\frac{1}{2}}, \quad \chi_e = \tan^{-1} \left(\frac{v_y}{v_x} \right) \quad (4.3)$$

In Fig. 4.2, R_i represents the line-of-sight separation between the vehicles Q_e and Q_i . The angular orientation θ_i of line-of-sight separation with respect to the positive X -axis defines the bearing or line-of-sight angle. Accordingly, the kinematic equations for relative motion

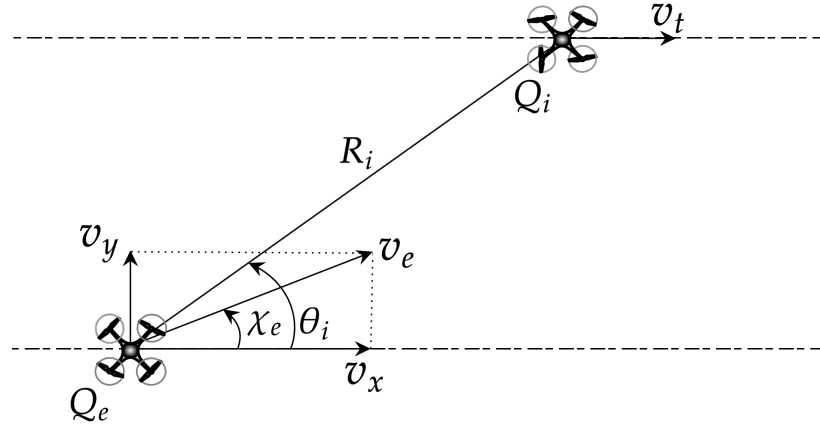


Figure 4.2: Instantaneous geometry.

between the ego vehicle and i^{th} neighboring vehicle can be defined as

$$\dot{R}_i = v_t \cos \theta_i - v_e \cos(\chi_e - \theta_i) \quad (4.4)$$

$$\dot{\theta}_i = \frac{-v_t \sin \theta_i - v_e \sin(\chi_e - \theta_i)}{R_i} \quad (4.5)$$

where v_t is the speed of the vehicles moving in the traffic lane. Based on bearings-only information, a three-phased guidance approach is presented as a solution to the problem.

4.2.1 Discerning guidance phase

The driving logic for the first phase, that is, discerning guidance phase is to maneuver the ego vehicle in the service lane so as to attain a non-rotating line-of-sight with respect to a neighboring vehicle in the traffic lane. Property 1 describes the logic.

Property 1 *The rate of change in line-of-sight angle is zero when two vehicles move with identical speeds and heading direction.*

The result in Property 1 can be readily deduced by using $v_e = v_t$ and $\chi_e = 0$ in Eq. (4.5), which leads to

$$\dot{\theta}_i = 0 \quad (4.6)$$

For the discerning phase a forward acceleration command is proposed for the ego vehicle as

$$a_x = -\delta \dot{\theta}_i \quad (4.7)$$

where δ is a positive gain. Using $v_y = 0$ in Eq. (4.3), the total velocity and heading of the ego vehicle can be obtained as

$$v_e = v_x, \quad \chi_e = 0 \quad (4.8)$$

Using Eq. (4.8) in Eq. (4.5), the rate of change of line-of-sight angle in this phase can be written as

$$\dot{\theta}_i = \frac{(v_x - v_t) \sin \theta_i}{R_i} \quad (4.9)$$

where $v_x \in \mathcal{D}_d$ and $\theta_i \in (0, \pi)$. Here, $\mathcal{D}_d = [-v_m, v_m]$ represents the domain of longitudinal speed, where $v_m \in \mathbb{R}$ is the maximum speed of the ego vehicle. It can be noted that $v_x = v_t$ is the equilibrium point for the dynamics in Eq. (4.9).

Proposition 4.1 *For the proposed forward acceleration guidance command Eq. (4.7), the vehicle motion is locally asymptotically stable about the equilibrium point $v_x = v_t$ for all $v_x(t = 0) \in \mathcal{D}_d$.*

Proof: Consider a Lyapunov function,

$$W_1(v_x) = \frac{1}{2}(v_t - v_x)^2 \quad (4.10)$$

Here, $W_1(v_x) = 0$ for $v_x = v_t$ and $W_1(v_x) > 0$, for all $v_x \neq v_t$. Hence, the function $W_1(v_x)$ is positive definite in \mathcal{D}_d . Taking the time derivative of the candidate function in Eq. (4.10),

$$\dot{W}_1(v_x) = -(v_t - v_x)a_x \quad (4.11)$$

Using Eq. (4.7) and Eq. (4.11),

$$\dot{W}_1(v_x) = (v_t - v_x)\delta \dot{\theta}_i \quad (4.12)$$

Using the line-of-sight rate expression of Eq. (4.9) in Eq. (4.12) leads to

$$\dot{W}_1(v_x) = -\frac{(v_t - v_x)^2 \delta \sin \theta_i}{R_i} \quad (4.13)$$

Using Eq. (4.13), $\theta_i \in (0, \pi)$ and $\delta > 0$, it can be deduced that $\dot{W}_1(v_x)$ is a negative definite function in \mathcal{D}_d , that is,

$$\dot{W}_1(v_x) \leq 0 \quad \forall v_x \in \mathcal{D}_d \quad (4.14)$$

$$\dot{W}_1(v_x) = 0 \quad \text{at } v_x = v_t \quad (4.15)$$

□

As per Proposition 4.1, the ego vehicle attains a longitudinal speed that is equal to the unknown speed of the vehicles in the traffic lane. Accordingly, the ego vehicle registers its instantaneous speed at the end of the discerning phase as the speed of the vehicles in the traffic lane.

Proposition 4.2 *Following the proposed guidance command of Eq. (4.7) in the discerning phase, an approximate time T_D taken to reach any line-of-sight rate ϵ is given by*

$$T_D \cong \frac{d}{\delta \sin^2 \theta_{id}(t_o)} \log \left(\frac{\dot{\theta}_{id}(t_o)}{\epsilon} \right)$$

where $\dot{\theta}_{id}(t_o)$ is the line-of-sight rate at the beginning of the discerning phase and $\frac{\epsilon}{\dot{\theta}_{id}(t_o)} \in (0, 1)$.

Proof: During the discerning phase, the of line-of-sight separation R_i can be related to the lateral separation d between the lanes as

$$R_i = \frac{d}{\sin \theta_i} \quad (4.16)$$

Using Eq. (4.16) in Eq. (4.9), the line-of-sight rate can be expressed as

$$\dot{\theta}_i = \frac{\sin^2 \theta_i (v_x - v_t)}{d} \quad (4.17)$$

Assuming negligible changes in the initial line-of-sight angle $\theta_{id}(t_o)$ during the discerning phase, Eq. (4.17) simplifies to

$$\dot{\theta}_i = \frac{\sin^2 \theta_{id}(t_o) (v_x - v_t)}{d} \quad (4.18)$$

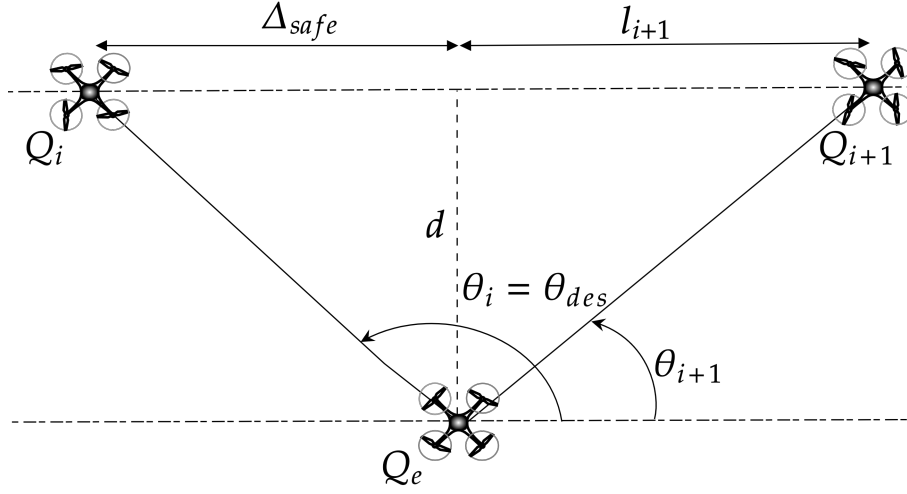


Figure 4.3: An instantaneous geometry during the longitudinal guidance phase.

Differentiating Eq. (4.18) with respect to time and using Eq. (4.7) therein leads to

$$\ddot{\theta}_i = \frac{-\delta \sin^2 \theta_{id}(t_o)}{d} \dot{\theta}_i \quad (4.19)$$

which can be solved to obtain

$$\dot{\theta}_i(t) = \dot{\theta}_{id}(t_o) e^{-\frac{\delta \sin^2 \theta_{id}(t_o)}{d} t} \quad (4.20)$$

Since $\frac{\delta \sin^2 \theta_{id}(t_o)}{d} > 0$, from (4.20), it can be deduced that $\dot{\theta}_i(t)$ varies monotonically from $\dot{\theta}_{id}(t_o)$ to zero. Integrating Eq. (4.20), the time T_D taken to attain any line-of-sight rate ϵ satisfying $\frac{\epsilon}{\dot{\theta}_{id}(t_o)} \in (0, 1)$ can be deduced as

$$T_D \approx \frac{d}{\delta \sin^2 \theta_{id}(t_o)} \log \left(\frac{\dot{\theta}_{id}(t_o)}{\epsilon} \right) \quad (4.21)$$

□

4.2.2 Longitudinal guidance phase

Utilizing the speed of the vehicles in the traffic lane as obtained at the end of the discerning guidance phase, the longitudinal guidance phase maneuvers the ego vehicle along the service lane until it finds a gap of suitable width in the traffic lane. The gaps in the traffic lane are identified using bearing information of two adjacent vehicles as depicted in Fig. 4.3. A gap of

minimum width $2\Delta_{safe}$ is considered feasible for merging into the traffic lane. The ego vehicle maneuvers to achieve the bearing orientation θ_{des} with respect to the i^{th} vehicle in the traffic lane such that

$$\theta_{des} = \pi - \tan^{-1} \left(\frac{d}{\Delta_{safe}} \right) \quad (4.22)$$

At this orientation, a forward clearance is Δ_{safe} with respect to the i^{th} vehicle. Using d , $\Delta_{safe} > 0$ in Eq. (4.22),

$$\theta_{des} \in \left(\frac{\pi}{2}, \pi \right) \quad (4.23)$$

From this relative position, the forward separation between ego vehicle and $i + 1^{\text{th}}$ vehicle can be determined as

$$l_{i+1} = \frac{d}{\tan \theta_{i+1}} \quad (4.24)$$

A gap is considered suitable if

$$l_{i+1} \geq \Delta_{safe} \quad (4.25)$$

For achieving the desired orientation with respect to the i^{th} vehicle in the traffic lane, a longitudinal velocity command is proposed for the ego vehicle as

$$v_x = v_t (1 + k \sin(\theta_{des} - \theta_i)) \quad (4.26)$$

where k is a positive gain.

It can be noted that the proposed longitudinal velocity command in Eq. (4.26) provides a variable relative speed with respect to the neighboring vehicle, which leads to attaining the desired relative orientation θ_{des} . To construct such a velocity command, the neighboring vehicles' velocity v_t is needed, which is obtained by the proposed discerning phase. Again, using $v_y = 0$ in Eq. (4.3), the total velocity and heading of the ego vehicle in the longitudinal phase satisfy Eq. (4.8), which leads to the line-of-sight rate as governed by Eq. (4.9). Using Eq. (4.26) in Eq. (4.9), the line-of-sight rate in the longitudinal phase can be deduced as

$$\dot{\theta}_i = \frac{kv_t \sin(\theta_{des} - \theta_i) \sin \theta_i}{R_i} \quad (4.27)$$

where $\theta_i \in \mathcal{D}_L$. The domain of line-of-sight angle during longitudinal phase \mathcal{D}_L is defined as $\mathcal{D}_L = (0, \pi)$. The solution $\theta_i = \theta_{des}$ corresponds to equilibrium line-of-sight angle for this phase. Next, we investigate the stability of the system about that equilibrium point.

Proposition 4.3 *Following the proposed longitudinal velocity command of Eq. (4.26), the motion of the ego vehicle is asymptotically stable about $\theta_i = \theta_{des}$ for all $\theta_i(t_o) \in \mathcal{D}_L$.*

Proof: Consider the Lyapunov candidate function

$$W_2(\theta_i) = \frac{1}{2} (\theta_{des} - \theta_i)^2 \quad (4.28)$$

Here, $W_2(\theta_i) \geq 0$ for all $\theta_i \in \mathcal{D}_L$ with $W_2(\theta_i) = 0$ if and only if $\theta_i = \theta_{des}$. Hence, the Lyapunov candidate function in Eq. (4.28) is positive definite over the domain \mathcal{D}_L . The time derivative of the Lyapunov candidate function can be obtained using Eq. (4.28) as

$$\dot{W}_2(\theta_i) = -(\theta_{des} - \theta_i)\dot{\theta}_i \quad (4.29)$$

Using Eq. (4.27) in Eq. (4.29) yields

$$\dot{W}_2(\theta_i) = -\frac{kv_t(\theta_{des} - \theta_i) \sin(\theta_{des} - \theta_i) \sin \theta_i}{R_i} \quad (4.30)$$

Eq. (4.30) implies

$$\dot{W}_2(\theta_i) \leq 0 \quad \forall \theta_i \in \mathcal{D}_L \quad (4.31)$$

$$\dot{W}_2(\theta_i) = 0 \quad \text{at } \theta_i = \theta_{des} \quad (4.32)$$

□

If a gap is found unsuitable, the ego vehicle uses the proposed longitudinal velocity command for achieving θ_{des} with respect to the $i + 1^{\text{th}}$ vehicle. The process is repeated until a suitable gap is found.

Proposition 4.4 *During a longitudinal phase, the time T_L taken by the ego vehicle to attain any $\theta_{ilf} \in (\theta_{il}(t_o), \theta_{des})$, where $\theta_{il}(t_o)$ is the line-of-sight angle at the beginning of that longitudinal phase, is given by*

$$T_L = \frac{d}{kv_t \sin^2 \theta_{des}} \left(\sin \theta_{des} (\csc \theta_{il}(t_o) - \csc \theta_{ilf}) + 2 \tanh^{-1} \left(\sin \theta_{des} \tan \frac{\theta_{ilf}}{2} + \cos \theta_{des} \right) \right. \\ \left. + \cos \theta_{des} \log \left(\frac{\tan \frac{\theta_{ilf}}{2}}{\tan \frac{\theta_{il}(t_o)}{2}} \right) - 2 \tanh^{-1} \left(\sin \theta_{des} \tan \frac{\theta_{il}(t_o)}{2} + \cos \theta_{des} \right) \right)$$

Proof: During longitudinal phase, the line-of-sight separation again satisfies Eq. (4.16), and using that information in (4.27), the line-of-sight rate can be expressed as

$$\dot{\theta}_i = \frac{kv_t \sin(\theta_{des} - \theta_i) \sin^2 \theta_i}{d} \quad (4.33)$$

which implies

$$T_L = \frac{d}{kv_t} \int_{\theta_{il}(t_o)}^{\theta_{ilf}} \frac{d\theta_i}{\sin(\theta_{des} - \theta_i) \sin^2 \theta_i} \quad (4.34)$$

$$\begin{aligned} \Rightarrow T_L = \frac{d}{kv_t \sin^2 \theta_{des}} & \left(\sin \theta_{des} (\csc \theta_{il}(t_o) - \csc \theta_{ilf}) + 2 \tanh^{-1} \left(\sin \theta_{des} \tan \frac{\theta_{ilf}}{2} + \cos \theta_{des} \right) \right. \\ & \left. + \cos \theta_{des} \log \left(\frac{\tan \frac{\theta_{ilf}}{2}}{\tan \frac{\theta_{il}(t_o)}{2}} \right) - 2 \tanh^{-1} \left(\sin \theta_{des} \tan \frac{\theta_{il}(t_o)}{2} + \cos \theta_{des} \right) \right) \end{aligned} \quad (4.35)$$

□

4.2.3 Transit guidance phase

The transit guidance phase is a maneuver that starts after the ego vehicle identifies a suitable gap in the traffic lane. Specifically, when the ego vehicle attains θ_{des} with respect to i^{th} neighboring vehicle, with l_{i+1} satisfying Eq. (4.25). Using the bearing information θ_i , the longitudinal and lateral velocity commands for the transit guidance phase are proposed as

$$v_x = v_t \quad (4.36)$$

$$v_y = \kappa \sin \theta_i \quad (4.37)$$

where κ is a positive gain. The transit guidance phase uses a purely lateral maneuver for the ego vehicle to move to the identified gap in the traffic lane. Figure 4.4 represents an instantaneous quadrotor position while executing the transit maneuver. Using Eqs. (4.1) and (4.2) in Eq. (4.5),

$$\dot{\theta}_i = \frac{-v_t \sin \theta_i - v_y \cos \theta_i + v_x \sin \theta_i}{R_i} \quad (4.38)$$

Using Eqs. (4.36)-(4.38), the rate of change of line-of-sight angle in this phase can be expressed as,

$$\dot{\theta}_i = -\frac{\kappa \sin \theta_i \cos \theta_i}{R_i} \quad (4.39)$$

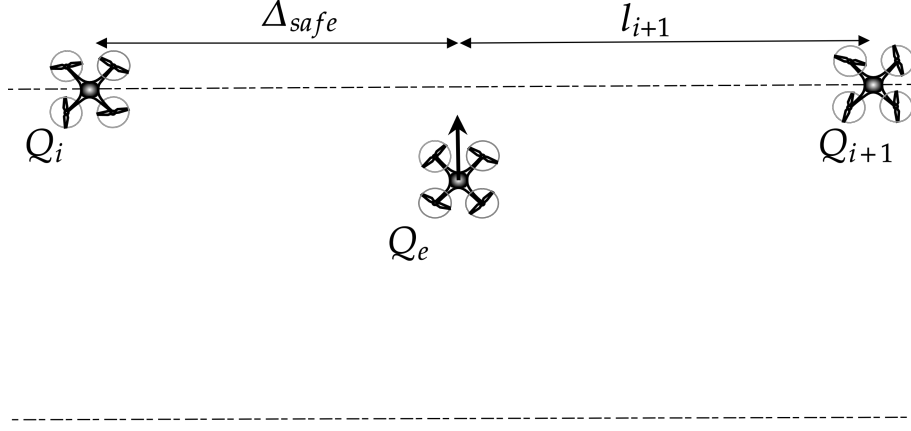


Figure 4.4: Instantaneous geometry during transit phase

where $\theta_i \in \mathcal{D}_T$. The domain for line-of-sight angle during the transit phase is given by

$$\mathcal{D}_T = \left[\theta_{des}, \frac{3\pi}{2} \right) \quad (4.40)$$

Note that $\frac{3\pi}{2}$ is the theoretical upper bound on θ_i during this phase, which corresponds to $y_e \rightarrow \infty$. Equations (4.23) and (4.40) imply

$$\mathcal{D}_T = \left(\frac{\pi}{2}, \frac{3\pi}{2} \right) \quad (4.41)$$

Note that $\theta_i = \pi$ is the only equilibrium point of the dynamics given in Eq. (4.39) that is within \mathcal{D}_T . This equilibrium point corresponds to the desired position of the ego vehicle in the traffic lane.

Proposition 4.5 *Under the lateral velocity guidance command given in Eq. (4.37), the ego vehicle motion is asymptotically stable about $\theta_i = \pi$ for all $\theta_i(t_o) \in \mathcal{D}_T$.*

Proof: Consider a Lyapunov candidate function

$$W_3(\theta_i) = \frac{1}{2} (\pi - \theta_i)^2 \quad (4.42)$$

Here, $W_3(\pi) = 0$ and $W_3(\theta_i) > 0$, for all $\theta_i \neq \pi$, and accordingly, the function in Eq. (4.42) is positive definite in \mathcal{D}_T . Taking the time derivative of the Lyapunov candidate function in Eq. (4.42)

$$\dot{W}_3(\theta_i) = -(\pi - \theta_i)\dot{\theta}_i \quad (4.43)$$

Using Eq. (4.39) in Eq. (4.43),

$$\dot{W}_3(\theta_i) = \frac{\kappa(\pi - \theta_i) \sin \theta_i \cos \theta_i}{R_i} \quad (4.44)$$

Eq. (4.44) implies

$$\dot{W}_3(\theta_i) \leq 0 \quad \forall \theta_i \in \mathcal{D}_T \quad (4.45)$$

$$\dot{W}_3(\theta_i) = 0 \quad \text{at } \theta_i = \pi \quad (4.46)$$

□

Thus, using the proposed lateral velocity guidance law, the bearing angle asymptotically converges to the desired value of π starting from any initial condition in \mathcal{D}_T . Further, the relative motion during the proposed transit phase is along the shortest distance between the two lanes, which can minimize the time spent outside any cylindrical geofences considered around the lanes.

Proposition 4.6 *The time T_T taken by the ego vehicle to reach any $\theta_{itf} \in (\theta_{des}, \pi)$ during transit phase is given by*

$$T_T = \frac{\Delta_{safe}}{\kappa} \left(\sec \theta_{itf} - \sec \theta_{des} + \log \left(\frac{\csc \theta_{des} + \cot \theta_{des}}{\csc \theta_{itf} + \cot \theta_{itf}} \right) \right)$$

Proof: Since the transit phase is a purely lateral maneuver, the line-of-sight separation is related to forward clearance Δ_{safe} as

$$R_i \cos(\pi - \theta_i) = \Delta_{safe} \quad (4.47)$$

Using (4.47) in Eq. (4.39), the line-of-sight rate during transit phase is deduced as

$$\dot{\theta}_i = \frac{\kappa \sin \theta_i \cos^2 \theta_i}{\Delta_{safe}} \quad (4.48)$$

Integrating Eq. (4.48), the time taken by the ego vehicle to reach any $\theta_{itf} \in (\theta_{des}, \pi)$ can be obtained as

$$T_T = \frac{\Delta_{safe}}{\kappa} \int_{\theta_{des}}^{\theta_{itf}} \frac{d\theta_i}{\sin \theta_i \cos^2 \theta_i} \quad (4.49)$$

$$\Rightarrow T_T = \frac{\Delta_{safe}}{\kappa} \left(\sec \theta_{itf} - \sec \theta_{des} + \log \left(\frac{\csc \theta_{des} + \cot \theta_{des}}{\csc \theta_{itf} + \cot \theta_{itf}} \right) \right) \quad (4.50)$$

□

Remark 4.1 *The time duration characteristics of the three guidance phases expressed in Eqs. (4.21), (4.35), and (4.50) can serve as effective tools for choosing the guidance gains δ , k , and κ , respectively.*

Proposition 4.7 describes the minimum safety distance property of the proposed three-phased guidance method.

Proposition 4.7 *For $\Delta_{safe} \leq d$, the line of sight separation $R_i(t) \geq \Delta_{safe}, \forall t \geq 0$.*

Proof: Let t_d , t_l , and t_t denote the time instants at the end of the discerning, longitudinal and transit guidance phase, respectively, where $t_t > t_l > t_d > 0$. The line-of-sight separation between Q_e and Q_i can be written as

$$R_i = ((x_e - x_i)^2 + (y_e - y_i)^2)^{\frac{1}{2}} \quad (4.51)$$

where (x_i, y_i) denotes the position of the i^{th} vehicle in the traffic lane. During the discerning and longitudinal phases, $v_y = 0$ or $y_i - y_e = d$. Using that information in Eq. (4.51) leads to

$$R_i^2 = (x_e - x_i)^2 + d^2, \quad t \leq t_l \quad (4.52)$$

$$\implies R_i(t) \geq d, \quad t \leq t_l \quad (4.53)$$

During the transit phase, $x_e - x_i = \Delta_{safe}$, which, using Eq. (4.51), implies

$$R_i^2 = \Delta_{safe}^2 + (y_e - y_i)^2, \quad t_l < t \leq t_t \quad (4.54)$$

$$\implies R_i \geq \Delta_{safe}, \quad t_l < t \leq t_t \quad (4.55)$$

Using Eqs. (4.53) and (4.55) with $\Delta_{safe} \leq d$,

$$R_i(t) \geq \Delta_{safe}, \quad \forall t \geq 0 \quad (4.56)$$

□

4.2.4 Discussion

The present work is focused on a paradigm where the ego vehicle has only the local information, that is, it can measure the bearing information of the immediate neighboring vehicles.

Vehicles using air corridors may have limited sensing capability, and the proposed framework offers an autonomous lane change plan applicable in such scenarios. In the other scenario where the bearing information of all the vehicles in the traffic lane is accurately available to the ego vehicle, the first suitable gap can be readily determined by evaluating the gap width condition

$$\frac{d}{\tan \theta_{i+1}} - \frac{d}{\tan \theta_i} \geq 2\Delta_{safe}, \quad \text{for } i = 1, 2, \dots, N \quad (4.57)$$

where the $\frac{d}{\tan \theta_i}$ is the instantaneous X separation between the ego vehicle and the i^{th} vehicle in the traffic lane. The longitudinal guidance command of Eq. (4.26) can then be used directly to approach the first suitable opening. This may avoid the repeated accelerations and decelerations used by the ego vehicle in locally evaluating all the gap widths prior to finding the first suitable one. In essence, the proposed method works for a quadrotor having the minimum sensing information to execute lane merge. However, as discussed, a modified version of the proposed method can be used to ignore unsuitable gaps in case accurate global information is available.

4.3 Guided Trajectory Generation and Control

The control architecture shown in Fig. 4.5 illustrates the tracking control for the quadrotor. Using the bearing information θ_i , and depending on the guidance phase, the guidance block generates desired velocity commands. The position controller takes the longitudinal and lateral velocity commands, desired altitude, and desired yaw angle as input to generate commanded attitude angles and total thrust. The inner attitude control loop generates the rolling, pitching, and yawing torque.

Desired velocity in the discerning phase can be obtained by integrating the proposed forward acceleration command in Eq. (4.7), as

$$v_{xd}(t) = v_{x_o} + \int_{t_o}^t -\delta\dot{\theta}_i dt \quad (4.58)$$

where v_{x_o} represents the initial longitudinal velocity of the ego vehicle. Using Eq. (4.58), the commanded velocity components for discerning phase can be expressed as

$$(v_{xd}, v_{yd}) = (v_{x_o} - \delta(\theta_i - \theta_i(t_o)), 0) \quad (4.59)$$

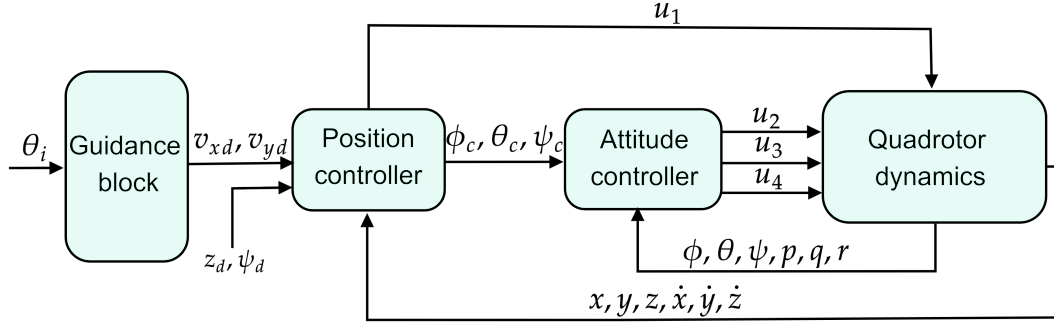


Figure 4.5: Control architecture.

In the longitudinal phase, the velocity components are deduced using Eq. (4.26) as

$$(v_{xd}, v_{yd}) = (v_t (1 + k \sin(\theta_{des} - \theta_i)), 0) \quad (4.60)$$

In the transit phase, Eqs. (4.36) and (4.37) are used to deduce the commanded velocity components as

$$(v_{xd}, v_{yd}) = (v_t, \kappa \sin \theta_i) \quad (4.61)$$

Note that the first two phases do not involve lateral motion. The position control logic generates the commanded roll and pitch angles considering a linearized version of Eqs. (2.36) and (2.37) as

$$\phi_c = \frac{1}{g} (\ddot{x}_c \sin \psi_d - \ddot{y}_c \cos \psi_d) \quad (4.62)$$

$$\theta_c = \frac{1}{g} (\ddot{x}_c \cos \psi_d + \ddot{y}_c \sin \psi_d) \quad (4.63)$$

where ψ_d represents the desired yaw angle. The commanded yaw angle is considered to be equal to the desired yaw angle, that is

$$\psi_c = \psi_d \quad (4.64)$$

The commanded translational acceleration components \ddot{x}_c , and \ddot{y}_c are computed using Proportional Derivative (PD) control logic [21], as

$$\ddot{x}_c = K_{px}(x_d - x) + K_{dx}(v_{xd} - \dot{x}) \quad (4.65)$$

$$\ddot{y}_c = K_{py}(y_d - y) + K_{dy}(v_{yd} - \dot{y}) \quad (4.66)$$

where K_{px} , K_{dx} , K_{py} , and K_{dy} are tunable position controller gains and the desired position coordinates, x_d and y_d are obtained by integrating v_{xd} and v_{yd} . The control input u_1 is calculated using PD control logic as

$$u_1 = m(g + K_{dz}(\dot{z}_d - \dot{z}) + K_{pz}(z_d - z)) \quad (4.67)$$

where z_d represents the desired altitude and (K_{dz}, K_{pz}) are tunable controller gains. The inner-loop attitude control structure uses ϕ_c , θ_c , and ψ_c to generate the control inputs u_2 , u_3 , and u_4 , respectively, details of which can be found in Subsection 2.4.2 of Chapter 2.

4.4 Numerical Simulation Results

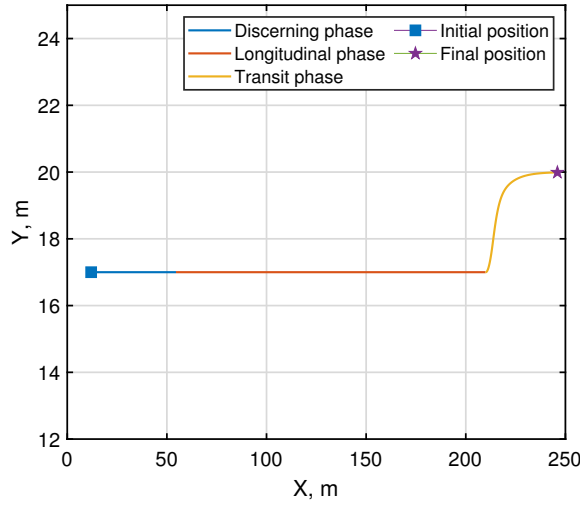
Numerical simulations are conducted to evaluate the performance of the proposed method. Consider an air corridor system consisting of a traffic and service lane with a lateral separation $d = 3$ m. As a sample scenario, we consider three vehicles moving in the traffic lane and an ego vehicle in the service lane. The quadrotor parameters are chosen as similar to the 6-DOF quadrotor model with mass and moment of inertia properties described in Section 2.5 of Chapter 2. The initial positions of the ego vehicle and the three vehicles in the traffic lane are (12, 17, 10) m, (16, 20, 10) m, (21, 20, 10) m, and (30, 20, 10) m, respectively. The initial velocity of the ego vehicle is 6 m/s. The minimum feasible gap width is considered as $2\Delta_{safe} = 8$ m, which using Eq. (4.22), corresponds to $\theta_{des} = 143.13$ deg. The speed of vehicles in the traffic lane is considered as $v_t = 5$ m/s. All simulations use a desired altitude of $z_d = 10$ m, desired yaw angle of $\psi_d = 0$, and saturation limits on commanded pitch and roll angles as ± 25 deg. The guidance gains are selected as $\delta = 7$, $k = 0.5$, and $\kappa = 3.3$, respectively. The position controller gains are chosen as $K_{dx} = 7.75$, $K_{px} = 15$, $K_{dy} = 8.15$, $K_{py} = 13$, $K_{dz} = 7.5$, and $K_{pz} = 15.8$. For the inner-loop structure as borrowed from Section 2.4.2 of Chapter 2, the gains are chosen as $K_{d\phi} = 0.7$, $K_{p\phi} = 12.8$, $K_{d\theta} = 0.5$, $K_{p\theta} = 5$, $K_{d\psi} = 0.5$, $K_{p\psi} = 2$, $K_{d\dot{x}} = 7.75$, $K_{p\dot{x}} = 15$, $K_{d\dot{y}} = 8.15$ and $K_{p\dot{y}} = 13$. The discerning phase is considered to be over when the absolute angular bearing rate between the ego vehicle and the neighboring vehicle goes below 5×10^{-5} rad/s. The longitudinal phase ends when the angular orientation between the ego vehicle and neighboring vehicle reaches $|\theta_{des} - \theta_i| \leq 0.005$ rad. All simulations are

terminated when the ego vehicle attains $|y_t - y_e(t)| \leq 0.01$ m, where y_t is the desired lateral position in the traffic lane.

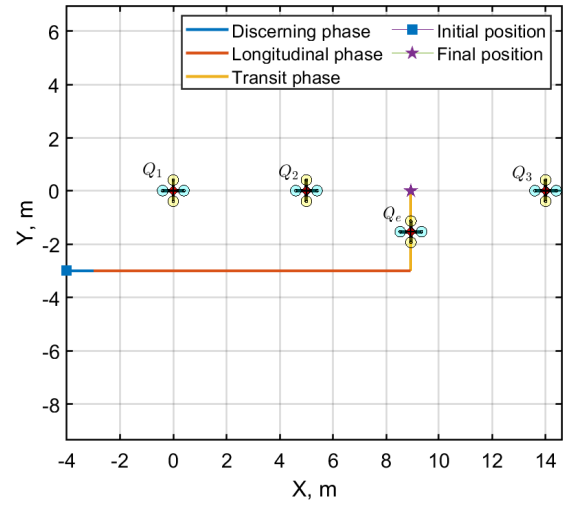
4.4.1 Case I: Sample lane transition scenario with noise free bearing information

The proposed guided trajectory is generated using true bearing angle information θ_1 , θ_2 , and θ_3 of the vehicles Q_1 , Q_2 , and Q_3 , respectively. Figures 4.6a and 4.6b plot the ego vehicle trajectory and its relative trajectory with respect to the neighboring vehicles, respectively. Therein, blue, red, and yellow portions of the trajectory represent discerning, longitudinal, and transit guidance phases, respectively. The bearing angle variations of the neighboring vehicles are shown in Fig. 4.6c. The engagement starts with the ego vehicle executing the discerning phase, which ends with a bearing angle of $\theta_1 = 45.052$ deg at 8.3142 s. Using Eq. (4.21), the duration of the discerning phase can be computed as $T_D = 9.2658$ s by considering $\epsilon = 5 \times 10^{-5}$ rad/s, which is the termination criterion for the discerning phase. This moderate error is because of the assumptions made in deriving the analytic expression and the effect of the 6-DOF dynamics of the vehicle. As marked in Fig. 4.6d, ego vehicle speed at that instant, $\dot{x} = 5$ m/s is recorded as the speed of the vehicles in the traffic lane.

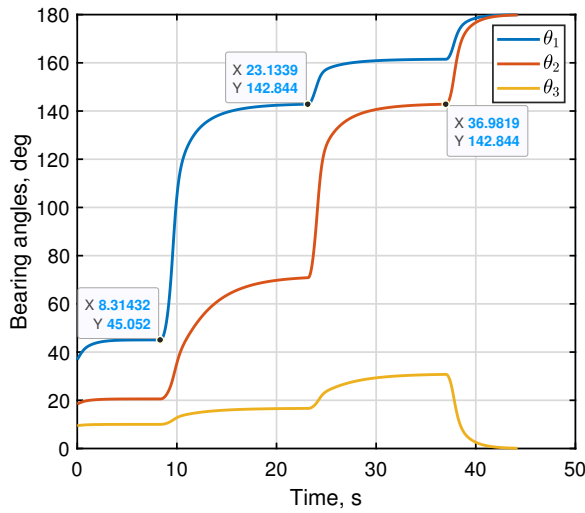
In the longitudinal phase, the ego vehicle moves forward to attain the desired bearing angle $\theta_1 = \theta_{des}$ deg. with respect to vehicle Q_1 and evaluates the safety criterion as given in Eq. (4.25). The duration of longitudinal phase is 14.8196 s, which matches closely with the $T_L = 14.7032$ s as obtained using the analytic expression given in Eq. (4.35) with $\theta_{ilf} = \theta_{des} - 0.005$ rad. The forward separation l_2 , as evaluated using Eq. (4.24), is found to be 1 m, which violates Eq. (4.25). Accordingly, the vehicle moves forward to attain $\theta_2 = \theta_{des}$ deg and l_3 is evaluated to be 5 m, which is feasible for a transition. The transit phase starts at 36.9819 s, which eventually takes the ego vehicle to the final desired position in 7.2202 s. This time duration of the transit phase closely matches with $T_T = 7.0739$ s as evaluated using Eq. (4.50). Therein, $\theta_{itf} = \pi - \tan^{-1} \left(\frac{0.01}{\Delta_{safe}} \right)$ is used, which corresponds to $y_t - y_e(t) = 0.01$ m. The close match for the analytic and simulation values of T_L and T_T , respectively, can be attributed to the exact nature of closed-form expression. From Fig. 4.6d, it can be seen that



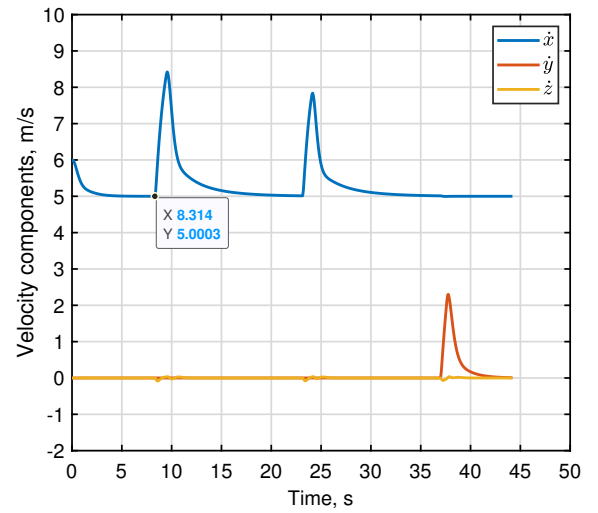
(a) Ego vehicle trajectory.



(b) Relative trajectory.



(c) Line-of-sight angle histories



(d) Velocity components of ego vehicle

Figure 4.6: Results for Case 1.

the lateral component of the velocity is zero during the discerning and longitudinal guidance phases. Positive lateral velocity contributes to the lateral movement of the quadrotor during the transit phase. At the end of the transit guidance phase, the quadrotor attains $(\dot{x}, \dot{y}) = (5, 0)$ m/s, which matches the speed of the vehicles in the traffic lane. Figures 4.7a and 4.7b show the pitch and roll angle profiles, respectively. The altitude response of the outer loop position controller is plotted in Fig. 4.7c, which shows tracking of the desired altitude of 10 m with

negligible error.

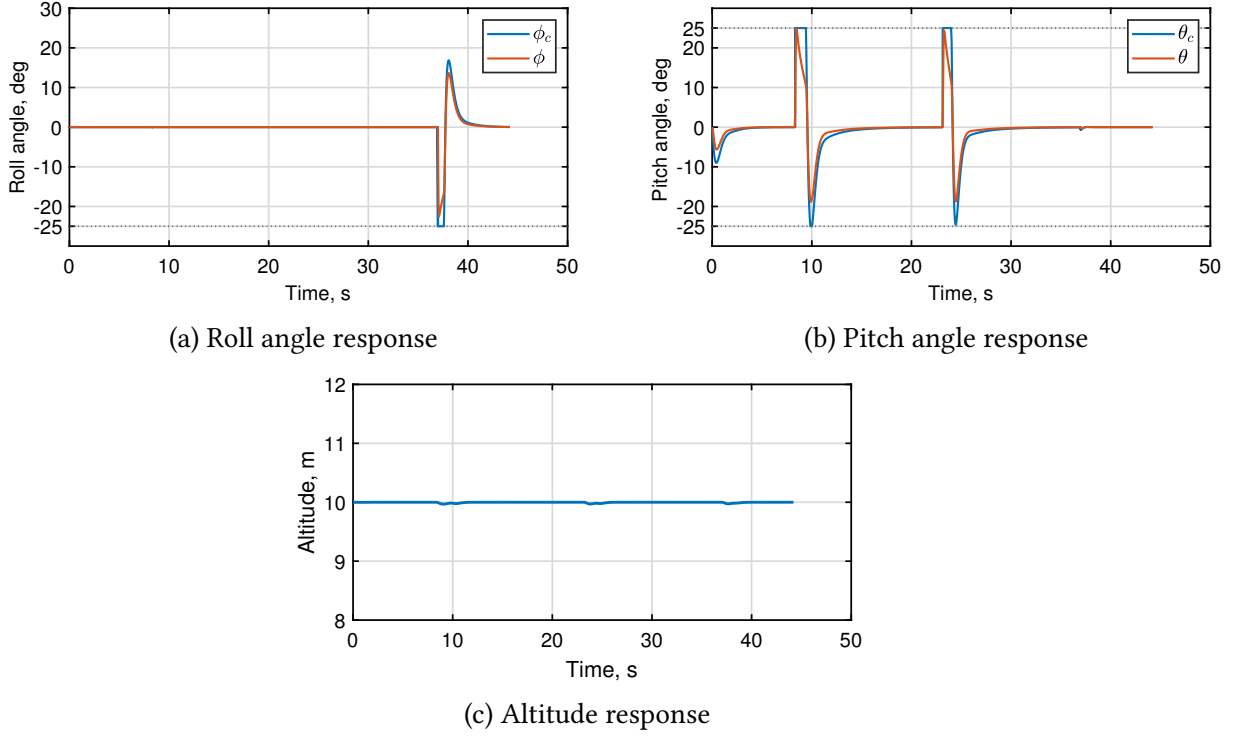


Figure 4.7: Attitude angles and altitude response for Case 1.

4.4.2 Case 2. Effect of noise in bearing information

This case study considers a scenario where the bearing information is corrupted with noise. The noisy bearing measurements $\theta_{i_m}(t)$ are generated by adding zero-mean Gaussian noise $\mathcal{N}(0, \sigma_\theta^2)$ to the true values $\theta_i(t)$, where σ_θ is its standard deviation. A second-order low pass filter [54] is used to obtain filtered bearing angles θ_{i_f} , which are then fed to the guidance block. The filter dynamics is governed by

$$\frac{d^2\theta_{i_f}}{dt^2} + 2\zeta\omega_N \frac{d\theta_{i_f}}{dt} + \omega_N^2\theta_{i_f} = \omega_N^2\theta_{i_m}, \quad i = 1, 2, 3 \quad (4.68)$$

where ζ and ω_N are the damping ratio and natural frequency of the filter. The filter parameters are chosen as $\zeta = 0.707$ and $\omega_N = 2\pi$ rad/sec.

The simulation scenario is similar to the one considered in Case 1. A Monte Carlo simulation study of 100 runs each is conducted for a specified noise distribution. The performance of

Table 4.1: Effect of noise in bearing information

Bearing measurement noise $\mathcal{N}(\text{mean, standard deviation(deg.)}^2)$	Detected velocity v_t (m/sec)		Distance from desired final position $ R_2(t_f) - \Delta_{safe} $ (m)	
	mean	standard deviation	mean	standard deviation
$\mathcal{N}(0, 0.5^2)$	5.0193	0.0084	0.0836	0.0525
$\mathcal{N}(0, 1^2)$	5.0186	0.0113	0.0831	0.0670
$\mathcal{N}(0, 1.5^2)$	5.0153	0.0124	0.0818	0.1081
$\mathcal{N}(0, 2^2)$	5.0168	0.0165	0.1090	0.1134
$\mathcal{N}(0, 2.5^2)$	5.0178	0.0236	0.1464	0.1666
$\mathcal{N}(0, 3^2)$	5.0223	0.0245	0.1713	0.1746

the proposed guidance method is evaluated by studying the detected velocity of neighboring vehicles at the end of the discerning phase v_t and the position error with respect to the desired final position in the destination lane $|R_2(t_f) - \Delta_{safe}|$, where $R_2(t_f)$ represents the final line-of-sight separation between Q_e and Q_2 . Table 4.1 illustrates the statistical results, which present negligible deterioration in performance. Errors in detected velocity and desired final position tend to increase with the increased standard deviation of the noise level. However, these errors are very small.

4.5 Summary

This chapter proposed a bearing-only information-based quadrotor guidance method for safe lane transition in air corridors. The method uses a three-phased guidance logic using the bearing information of the neighboring vehicles in the destination lane. The discerning guidance phase determines the velocity of the vehicles in the destination lane by utilizing a forward acceleration command that nullifies the rate of change of bearing angle. Through a forward velocity command, the subsequent longitudinal phase attains a desired orientation with respect to a potential gap in the destination lane. In the final phase, the ego vehicle occupies the desired gap using a lateral velocity guidance command. The commanded velocity inputs in the proposed method are designed as sinusoidal functions of the bearing information, which offers smooth and bounded variation in guidance commands to the quadrotor. Asymptotic

stability is ascertained around the desired equilibrium points of the three guidance phases. Further analysis deduces closed-form analytic expression for the duration of the three guidance phases. Therein, exact relationships are reduced for the time duration of the longitudinal and transit phases, while an approximate one is established for the discerning phase. The performance of the proposed guidance method is verified through simulation studies. Monte Carlo simulations are carried out using a second-order low-pass filter for normally distributed noise in the bearing information.

Chapter 5

Experimental Results

This chapter presents experimental validation results for the proposed guidance methods discussed in Chapters 2 and 3. An indoor experimental setup is utilized, integrating a quadrotor, command and communication center, and motion capture system. Figure 5.1 provides an overview of the system architecture of the overall experimental setup, illustrating the nature of information exchange between the components. The position and orientation of the quadrotor are measured using the indoor motion capture system. By combining the motion capture data and the quadrotor's inertial measurement unit (IMU) data, the command and communication system generates and sends control commands to the quadrotor.

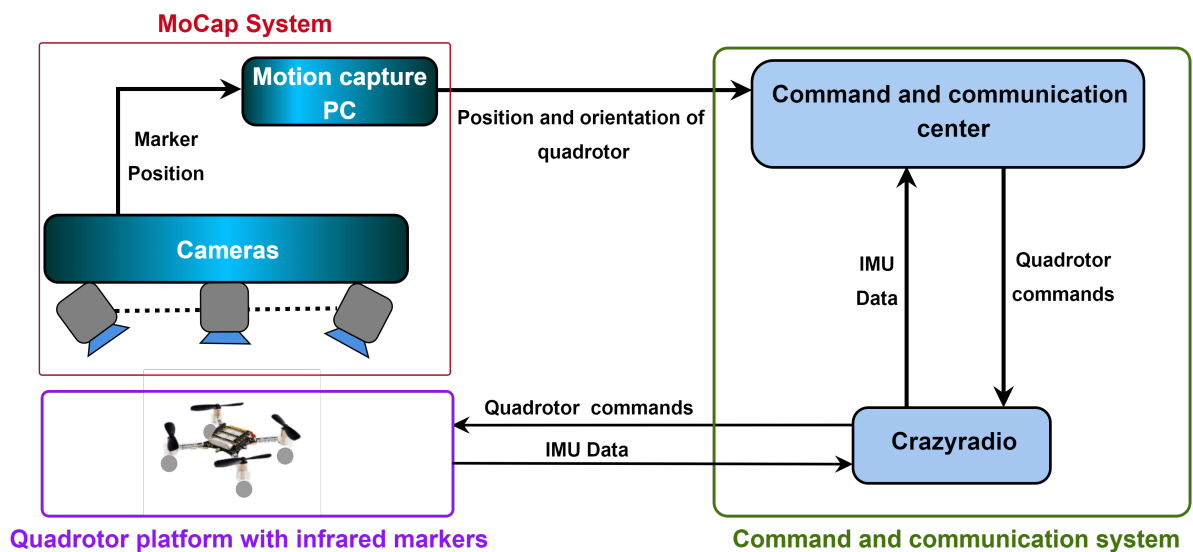


Figure 5.1: System architecture

5.1 Experimental Setup

The experimental setup includes a crazyflie 2.0 quadrotor platform with infrared markers attached to it, a motion capture system, and a command and communication system. Details of these components are presented in the following subsections.

5.1.1 Crazyflie 2.0 Quadrotor

Crazyflie 2.0 nano quadrotor is an open-source experimental platform widely used in academic research [55–58]. Figure 5.2 shows the Crazyflie 2.0 quadrotor. The quadrotor has four coreless DC motors, each with a rating of 4.2 V and 1 A. The motors are equipped with shafts measuring 3.5 mm in length and 0.8 mm in diameter. The motors are coupled with four plastic propellers, each with a diameter of 45 mm. These propulsion units are connected to the circuit board frame of the quadrotor. The dimension of the Crazyflie unit is 92 mm between diagonally opposed motor shafts and 29 mm in height. The total weight of the unit is 27 g. The quadrotor is supplied by a 250 mAh, 3.7 V Lithium polymer battery which weighs 7.1 g that can charge via standard uUSB. The charging time of the battery is 40 minutes and it is capable of sustaining continuous flight for up to 7 minutes. Crazyflie 2.0 has a maximum payload capacity of 15 g.



Figure 5.2: Crazyflie 2.0 quadrotor

Crazyflie 2.0 quadrotor is equipped with two microcontrollers, namely ARM Cortex-M4 and ARM CortexM0. The microcontroller ARM Cortex-M4 embedded processor STM32F405

is used to run the main application. This processor is a 32-bit architecture that operates at 168 MHz with 192 kb of SRAM. Additionally, it has a floating point unit that supports all ARM single-precision data-processing instructions and data types. The second microcontroller ARM CortexM0 embedded processor nRF51822, 32 MHz is for energy and radio communication management. The onboard sensor system is the MPU-9250 Inertial Measurement Unit. The unit contains gyroscope, accelerometer, magnetometer, and high-precision pressure sensor. The hardware and software architecture of the quadrotor is open source. More information on Crazyflie 2.0 can be found in [59].

5.1.2 Motion Capture System

Motion Capture (MoCap) is the process of recording the movement of objects or people. It comprises infrared source, cameras, infrared reflective markers, and software. The LED illumination ring of the camera produces infrared light, and the markers reflect it. The lens at the center of the camera captures reflected infrared light and it is processed by the cameras. The MoCap software receives the data through an ethernet protocol connected to the cameras, which is used to determine the position of markers accurately. The MoCap software allows to creating a rigid body using a group of markers arranged on the quadrotor, and it utilizes the received data to perform triangulation and calculate their precise locations. The motion of the object is tracked by the MoCap system, and the position and orientation of the rigid body are obtained.

The three-dimensional view of the laboratory and the capture volume of MoCap system are shown in Fig. 5.3. The choice of camera, number of cameras and their placement is dependent on the capture volume, which is defined as the volume where the quadrotors operate. The system uses OptiTrack Prime-13 camera as shown in Fig. 5.4a. Sixteen OptiTrack Prime-13 cameras are mounted on room ceiling using steel bars to cover the capture volume as shown in Fig. 5.3. OptiTrack Prime-13 camera lens has 56 deg. horizontal field-of-view (FOV) and 46 deg. vertical FOV as shown in Fig. 5.3. The placement and orientation of the cameras are based on spatial optimization which maximizes the coverage of the capture volume. Any point in the capture volume is covered by at least three cameras. Motion capture system uses

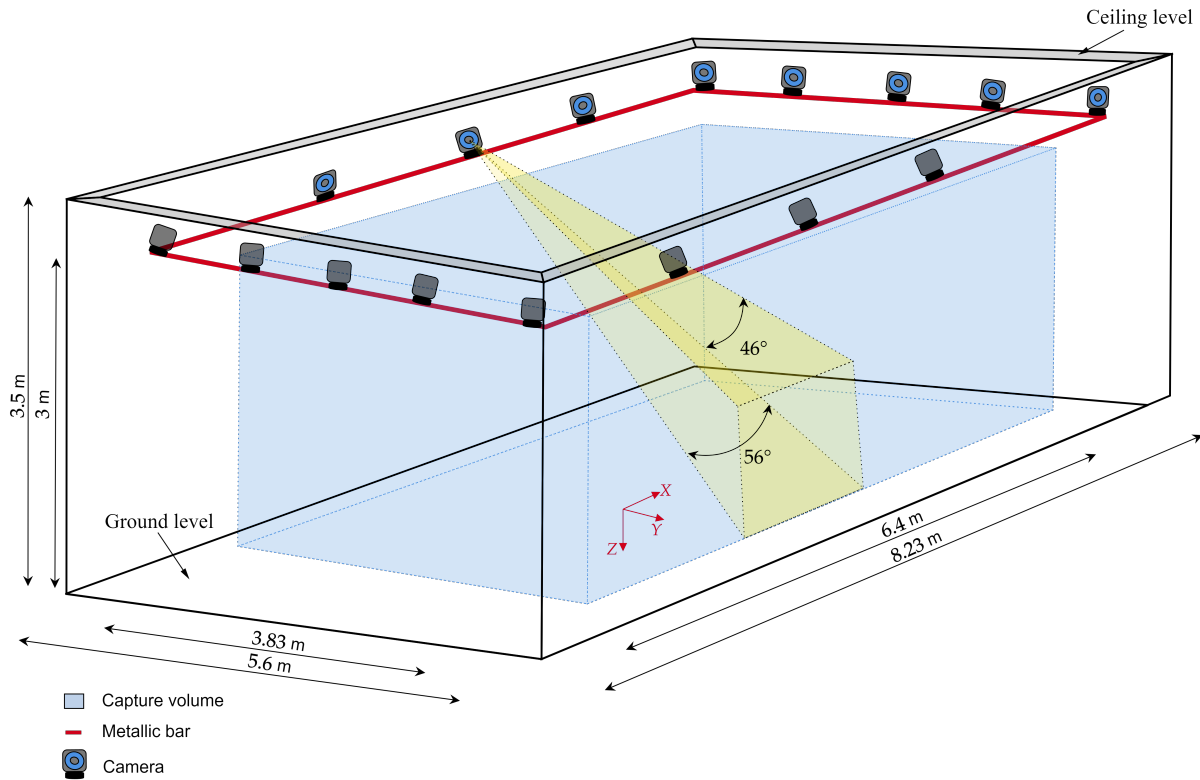


Figure 5.3: Room specification and camera placement



(a) OptiTrack Prime 13-camera



(b) OptiTrack infrared marker

Figure 5.4: OptiTrack Prime-13 camera and marker

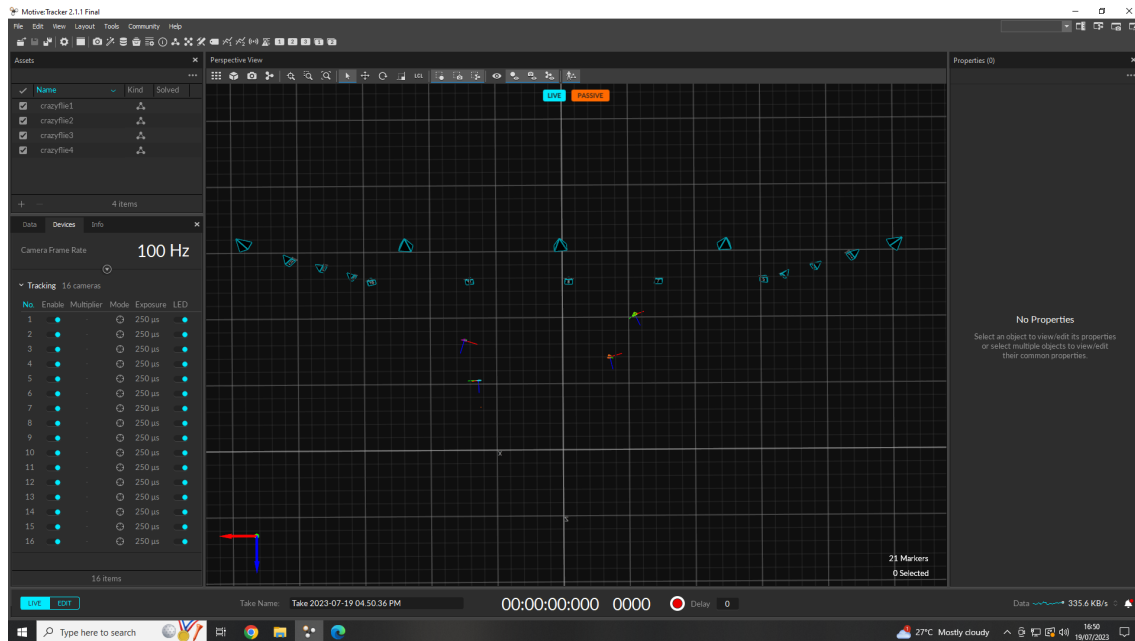
infrared reflective markers on the quadrotor body. The markers used are spherical in shape with a diameter of size 11 mm, as shown in Fig. 5.4b.

OptiTrack Motive software offers a graphical user interface (GUI) for the MoCap system. It facilitates the calibration process to define the capture volume and coordinate frame. The calibration process involves two steps: wand and setting the ground plane. During the wand process, a calibration wand equipped with asymmetric marker pattern is moved throughout the capture volume. The system is pre-programmed with information about the calibration wand's dimensions and the precise spacing between its markers. As the calibration wand traverses through the capture volume, the system captures synchronized 2D images from each camera. Through a triangulation process, the system determines the spatial position of the wand markers in relation to each camera. This movement helps identify the position and orientation of the cameras relative to each other. The setting of the ground planes aligns the MoCap coordinate system with the capture volume coordinate system, which is a fixed frame ($X - Y - Z$) with its origin at the ground level, as shown in Fig. 5.3. This step ensures that the recorded motion data is represented correctly in the defined coordinate system. Motive utilizes the rigid body information generated from the markers placed on the quadrotor to compute the real time position and orientation of the quadrotor. The visualization of rigid bodies on Motive software window is shown in Fig. 5.5. The rigid bodies data is then used by command center to control the quadrotors. More information on OptiTrack motion capture system can be found in [60].

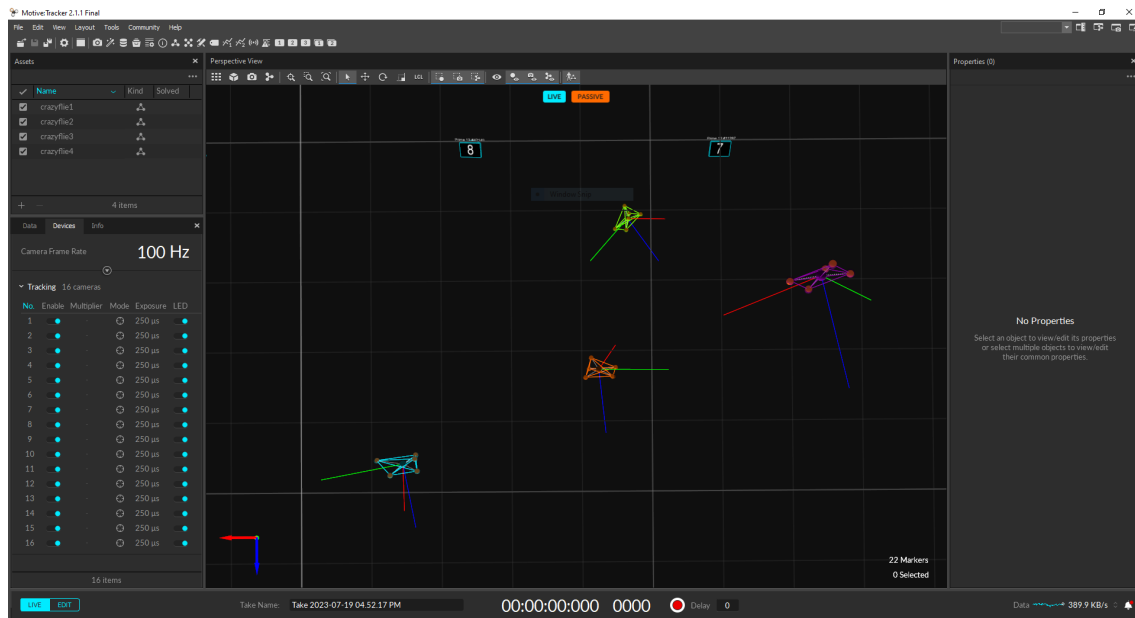
5.1.3 Command and Communication System

The command and communication system comprises command and communication center, and a crazyradio.

1. Command and communication center: The setup uses MATLAB Simulink as the command center, which runs on a Windows PC. The guidance logic and the control loops for task completion are developed in the Simulink. The communication center runs on a Linux PC, which uses Robotic Operating System (ROS). The communication center communicates with Crazyflie, MoCap, and the command center in a fashion as shown



(a) Front-view



(b) Zoomed-in version of front-view

Figure 5.5: Visualization of rigid bodies on Motive software interface

in Fig. 5.6 . Local Area Network connection is used for communication between the two PCs.

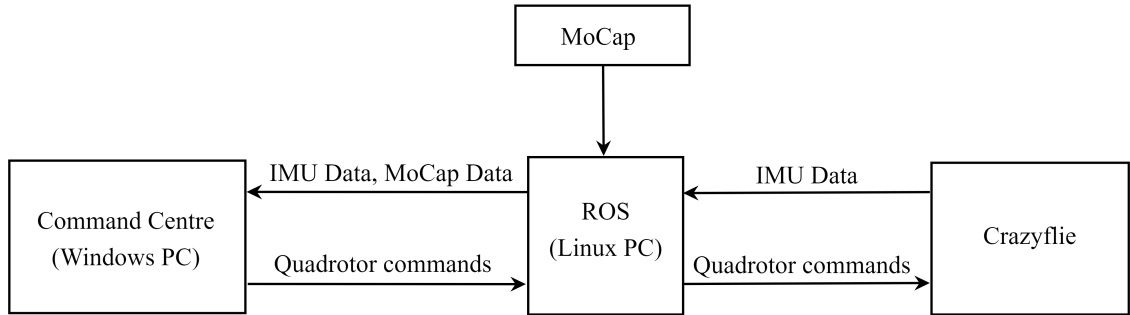


Figure 5.6: ROS communication with various systems

2. Crazyradio: Crazyradio as shown in Fig. 5.7 is a 2.4 GHz long range open source USB

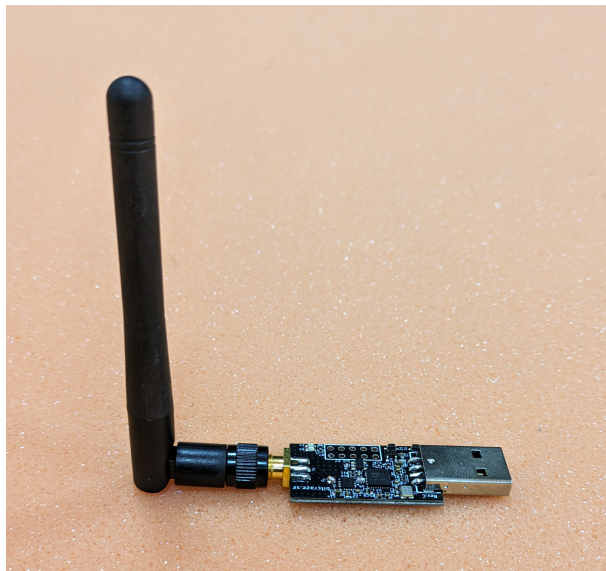


Figure 5.7: Crazyradio

radio dongle based on the nRF52840 from Nordic Semiconductor, which is used to communicate with the crazyflie 2.0. It is bidirectional radio link operating between crazyflie 2.0 and command and communication center.

5.1.4 Guidance and Control Architecture

As shown in Fig. 5.8, the Simulink architecture developed in the command center comprises three levels, namely commencing way point selector, guidance, and control. The quadrotor

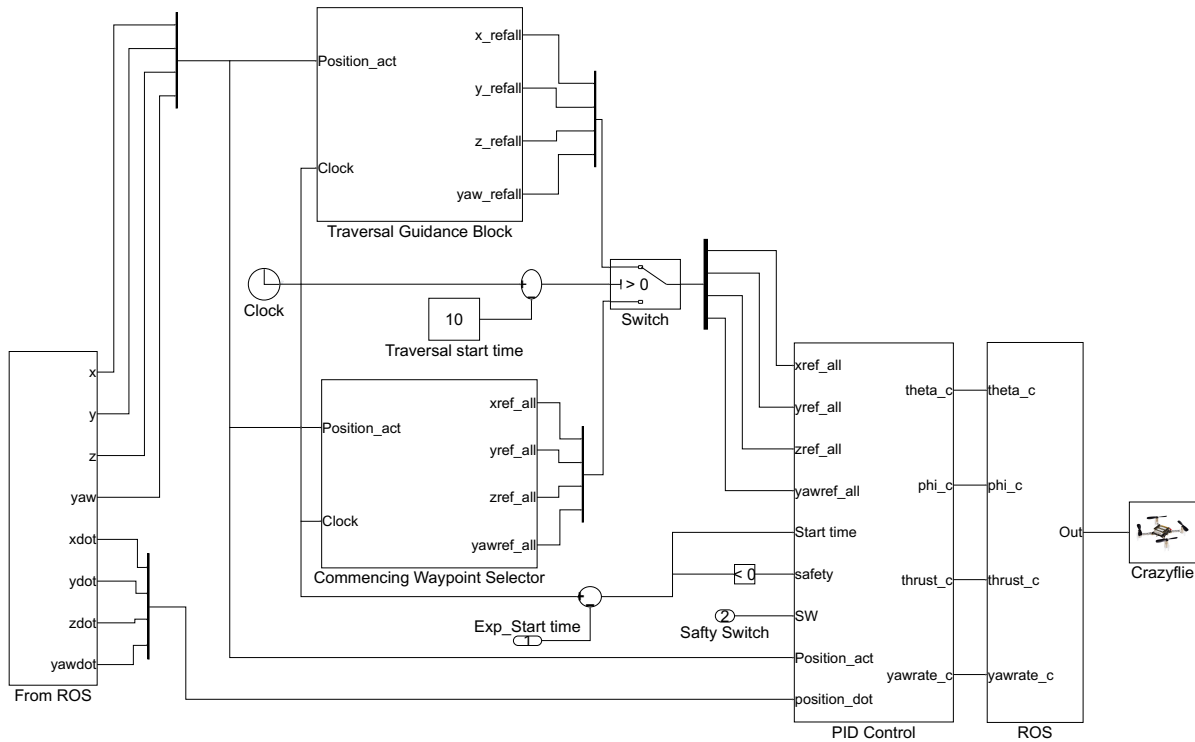


Figure 5.8: Simulink diagram

states are obtained from the “From ROS” subsystem. For generating arbitrary initial conditions for validation, subsystem “Commencing Waypoint Selector” is used to guide the quadrotor to a selected commencing waypoint before the traversal guidance starts. The “Commencing Waypoint Selector” uses minimum snap trajectory generation logic [22] for traversing between the initial point to any commencing waypoint. The proposed guidance methodologies are implemented in the “Traversal Guidance Block” subsystem, which generates the desired position and its derivatives. The quadrotor states are controlled by the “PID control” subsystem,

functioning as the autopilot for executing guidance commands while maintaining vehicle stability. The Crazyflie quadrotor platform operates with four distinct control inputs, namely total thrust u_1 , commanded roll ϕ_c , commanded pitch θ_c , and commanded yaw rate $\dot{\psi}_c$,

$$u = [u_1 \quad \phi_c \quad \theta_c \quad \dot{\psi}_c]^T \quad (5.1)$$

The autopilot generates these control inputs for the Crazyflie to track the reference commands. "ROS" subsystem transmits the generated control inputs to the Crazyflie through the Crazyradio dongle.

5.2 Flight Experiment Results

This section discusses the flight experimental results of the proposed guidance methods discussed in Chapters 2 and 3. Here, the bearing information of gap extremities are obtained by placing reflective infrared markers on the extremities. All experiments are carried out with the commanded yaw rate and commanded yaw angle set to zero.

5.2.1 Gap Traversal Guidance Method

A gap is indicated using two cuboid foams with dimensions of $0.2 \times 0.15 \times 1.27$ m, as shown in Fig. 5.9. The foams are placed making a gap of width 0.5 m at points $E_1(1.35, 0.63, 0)$ m and $E_2(1.85, 0.63, 0)$, as shown in Fig. 5.10. The Crazyflie is made initially to hover at commencing waypoint $(-1.5, -0.5, -1)$ m. The desired altitude and the desired velocity for the traversal are chosen as $z_{des} = -1$ m and $V = 0.3$ m/s, respectively. The bearing information of the gap edges are computed at every instant in the guidance block using the instantaneous relative position of Crazyflie with respect to E_1 and E_2 , that is θ_1 and θ_2 . These information are used for generating proposed guidance command χ_{des} as in Eq.(2.8). Further, the desired velocity components \dot{x}_{des} and \dot{y}_{des} and their desired trajectory components x_{des} and y_{des} are generated in "Traversal Guidance Block" using Eqs. (2.64) and (2.65). It uses the proposed guidance command in Eq.(2.8) till the instant when the traversal condition of Eq. (2.7) satisfies. Upon satisfying Eq. (2.7), the Crazyflie continues to follow the already achieved constant heading direction of $\chi_{des} = \frac{\pi}{2}$ rad.

The gap traversal guidance starts from its commencing waypoint, and the Crazyflie tracks

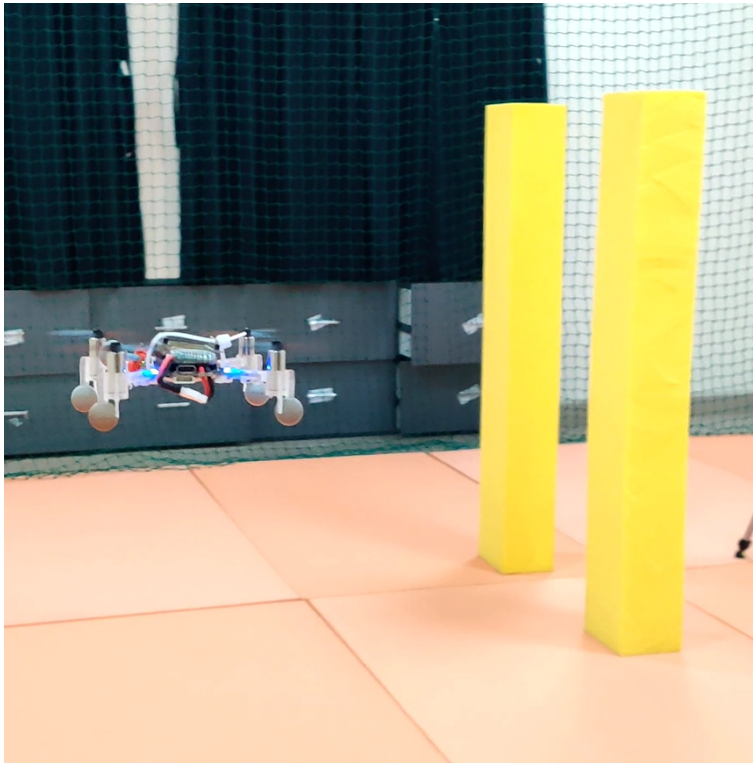


Figure 5.9: Crazyflie maneuvering towards the gap

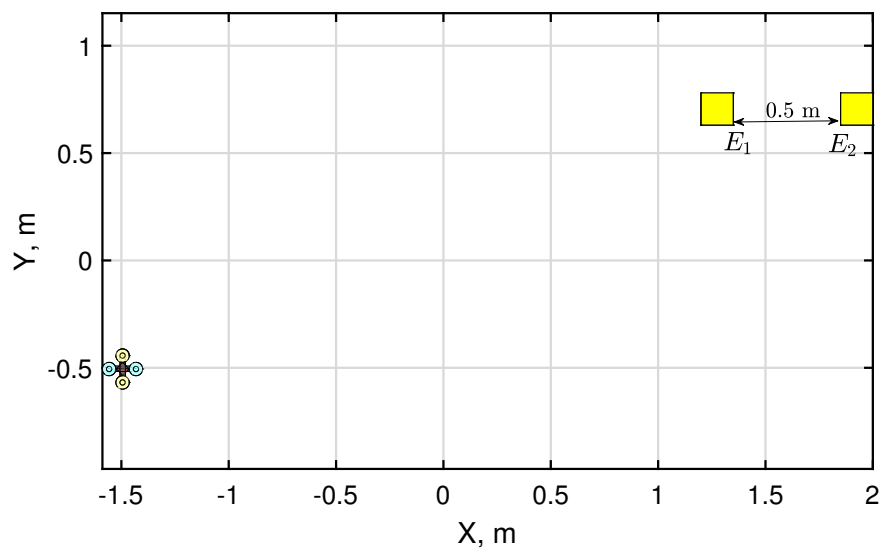


Figure 5.10: Top view of the Crazyflie hovering at commencing waypoint and the gap

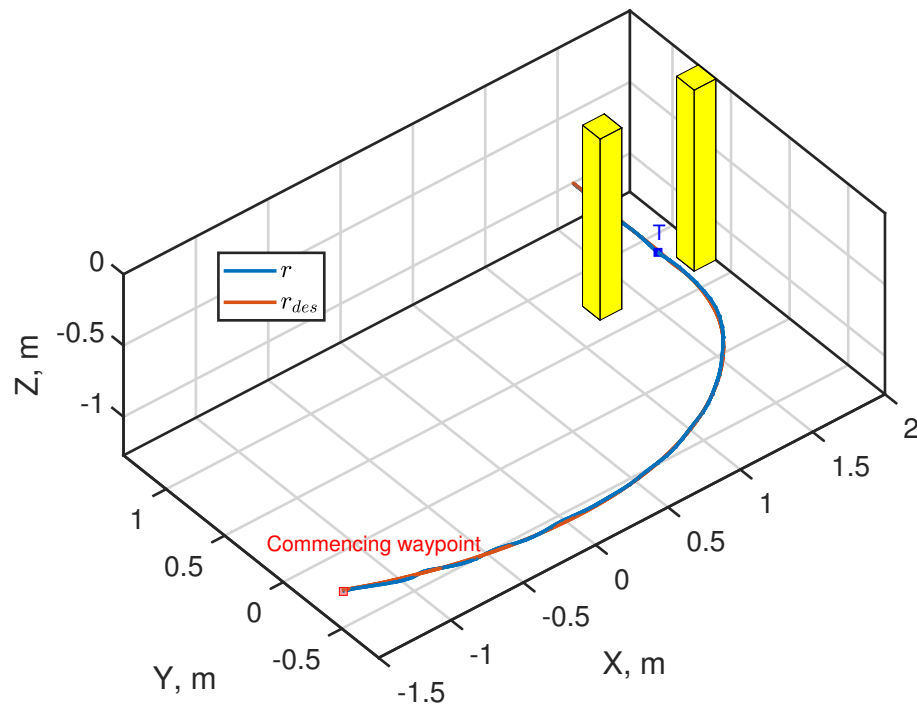


Figure 5.11: Crazyfly trajectory

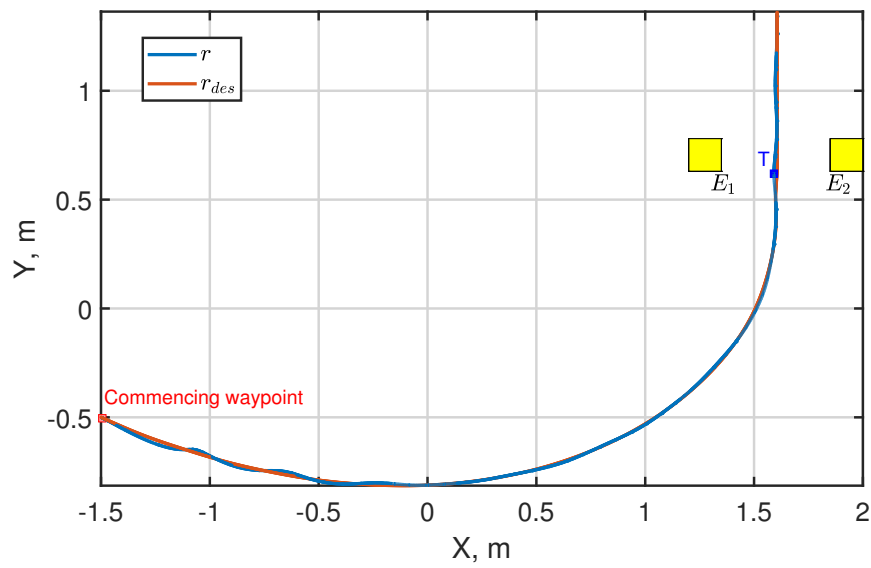


Figure 5.12: Top view of Crazyfly trajectory

the desired trajectory generated by the gap traversal guidance method, as shown in Figs. 5.11 and 5.12. Here, $r = [x \ y \ z]^T$ and $r_{des} = [x_{des} \ y_{des} \ z_{des}]^T$ are the achieved trajectory and the desired trajectory, respectively. The corresponding commanded and achieved trajectory components of the Crazyflie are plotted in Fig. 5.13. It can be seen that the Crazyflie maintains its desired altitude of -1 m with negligible deviation throughout its flight, and it reaches the traversal point (1.5917, 0.6306, -0.9938) m at 13.33 sec, with negligible position error of 0.0104 m. The bearing angle information obtained from the relative position of Crazyflie with

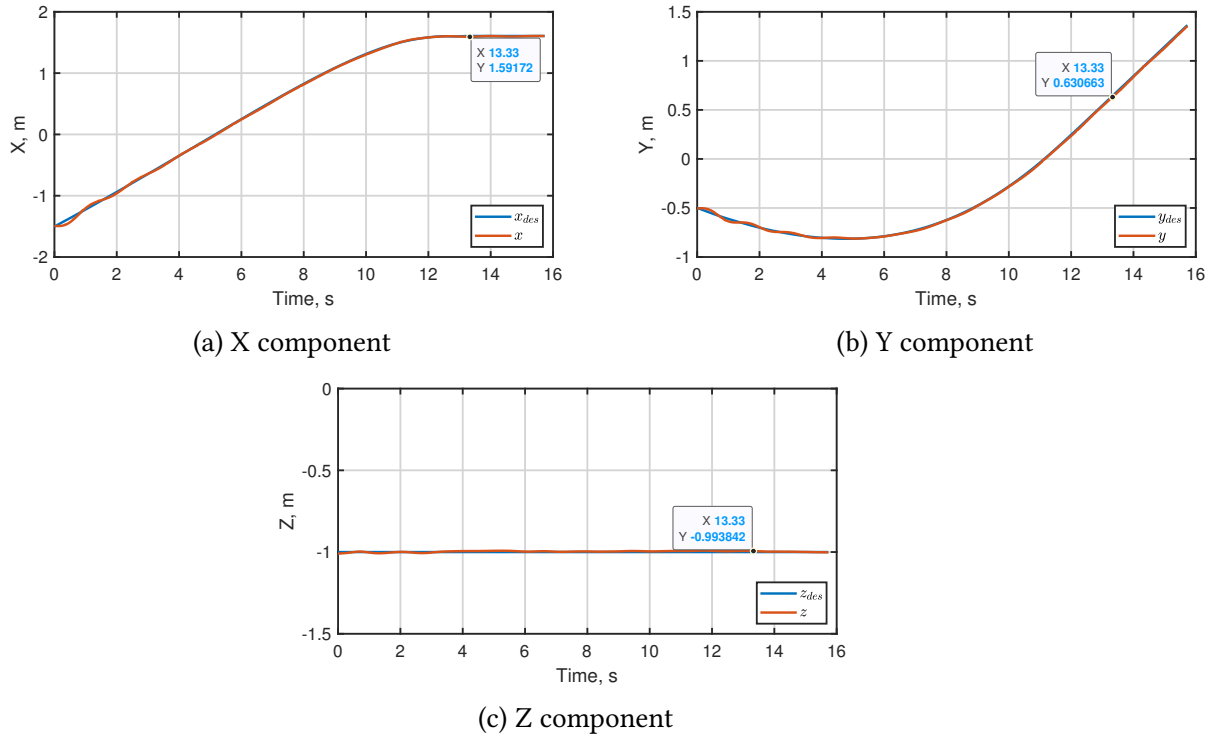


Figure 5.13: Trajectory components

respect to two wall edges, E_1 and E_2 , are plotted in Fig. 5.14a. It can be seen that the Crazyflie attains the gap traversing bearing angles at 13.33 sec. The bisector component $\frac{\theta_1 + \theta_2}{2}$ and shaping angle S component are plotted in Figs. 5.14b and 5.14c, respectively. It can be seen that the bisector component reaches its desired value of 90 deg. prior to reaching the gap, and the shaping component requirement diminishes to zero as the Crazyflie approaches the gap. The experimental video is available at the following URL:

<https://youtu.be/bXhuK-Lmwnc?si=KrPh1V3PHhar3Vh0>

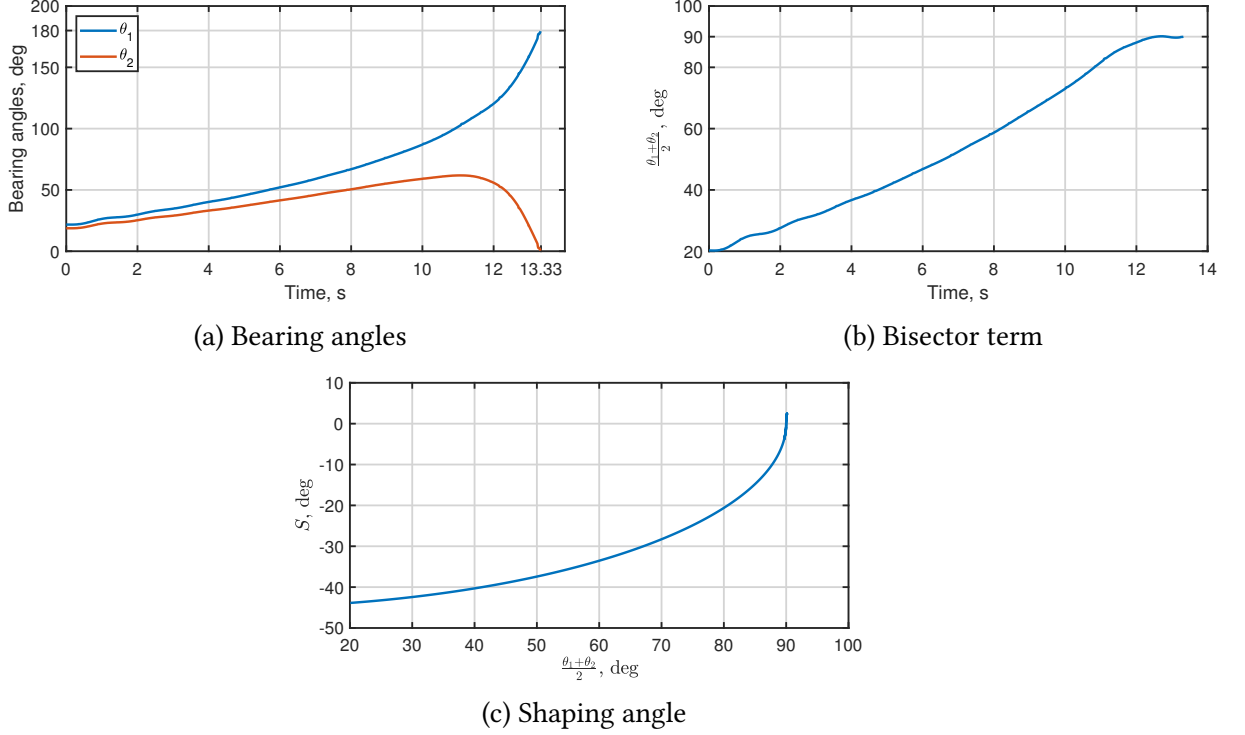


Figure 5.14: Angles for guidance computation

5.2.2 Guidance Method for Window Traversal

This subsection discusses experimental results for the window traversal guidance method illustrated in Chapter 3. An indicative window made up of foam is used for illustration, as shown in Fig. 5.15. The window presents a gap of dimension 0.6×0.6 m with its four extremities are located at $E_1(0.43, 1.22, -0.8)$ m, $E_2(1.03, 1.22, -0.8)$ m, $E_3(0.43, 1.22, -0.2)$ m, and $E_4(1.03, 1.22, -0.2)$ m, as shown in Fig. 5.16. The commencing waypoint for the Crazyflie in this experiment trial is set at $(2, 0, -2)$ m. The instantaneous azimuth angles β_i 's and elevation angles α_i 's (for $i = 1, 2, 3, 4$) of the four extremities are evaluated in the “Traversal Guidance block” shown in Fig. 5.8 using the instantaneous relative position of the Crazyflie through MoCap. This information is then utilized to generate the guidance commands χ_{des} and γ_{des} as in Eqs. (3.17) and (3.12). Once the traversal condition (3.10) is met, the guidance commands follow their already achieved heading angle $\chi_{des} = \frac{\pi}{2}$ rad and flight path angle $\gamma_{des} = 0$ rad. Utilizing Eqs. (3.60)-(3.65) the desired velocity components $(\dot{x}_{des}, \dot{y}_{des}, \dot{z}_{des})$ and the desired

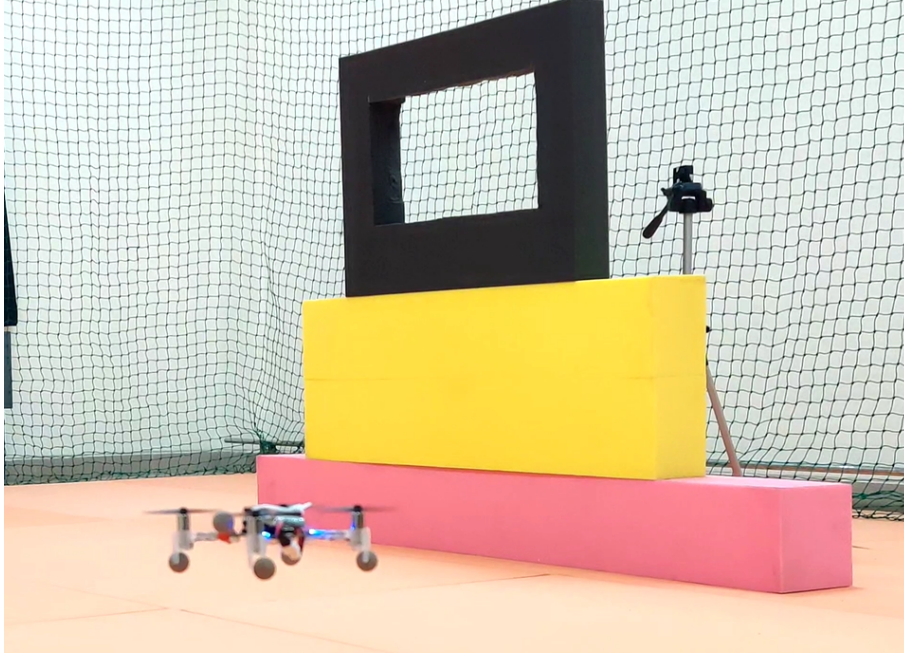


Figure 5.15: Crazyflie maneuvering towards the window

position components $(x_{des}, y_{des}, z_{des})$ are generated in the “Traversal Guidance Block” shown in Fig. 5.8. This experimental study considers the traversal velocity of Crazyflie as $V = 0.1$ m/s.

The commanded trajectory r_{des} generated by the guidance algorithm and the achieved trajectory of the Crazyflie r are shown in Fig. 5.16. It is observed that the Crazyflie tracks the commanded trajectory with a negligible error less than 0.0283 m. From Fig. 5.17, it can be seen that the Crazyflie successfully reaches the traversal point $T(0.7242, 1.2216, -0.5014)$ m at 27.72 s, with a negligible error of 0.014 m from the centroid of the window. The elevation angles with respect to the extremities E_1 and E_4 , and the azimuth angles with respect to E_1 and E_2 are depicted in Figs. 5.18a and 5.18b, respectively. The elevation angles and azimuth angles achieve their desired values as $(\alpha_1, \alpha_3) = (45, -45)$ deg and $(\beta_1, \beta_2) = (180, 0)$ deg, respectively in 27.72 s. From Figs. 5.18c and 5.18d, it can be seen that the bisector of elevation angles $\frac{\alpha_1 + \alpha_3}{2}$ and the bisector of azimuth angles $\frac{\beta_1 + \beta_2}{2}$ attain their desired value of 0 deg and 90 deg, respectively, when the Crazyflie approaches to the window. The shaping angle requirement monotonically diminishes to zero, as depicted in Figs. 5.18e and 5.18f.

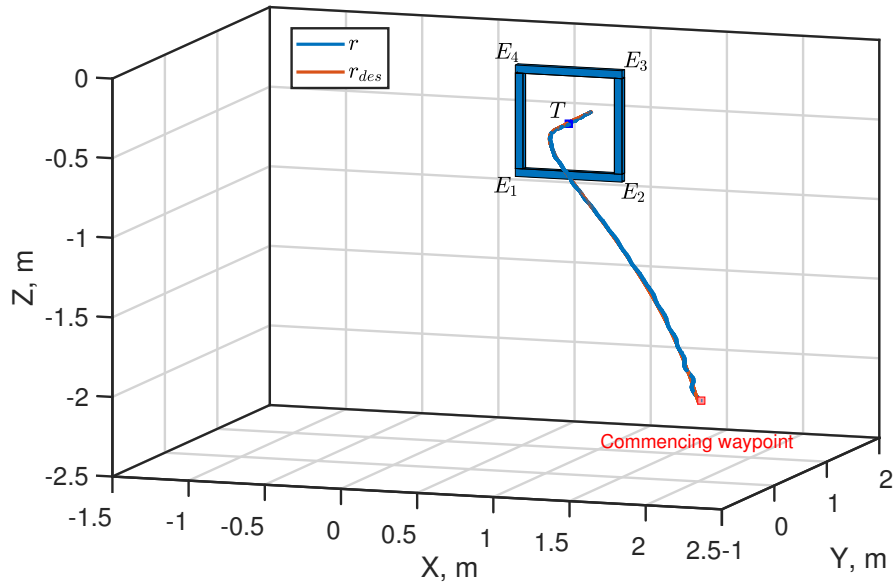
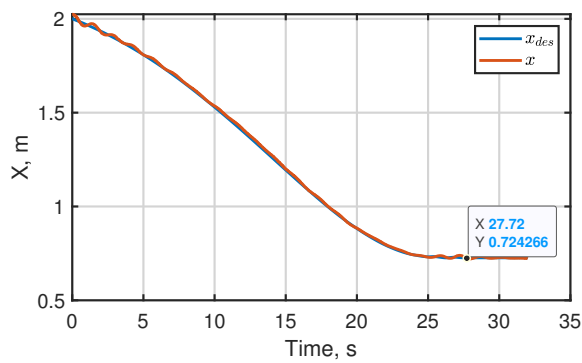
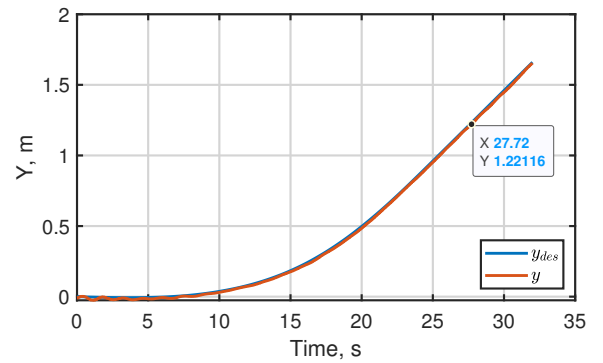


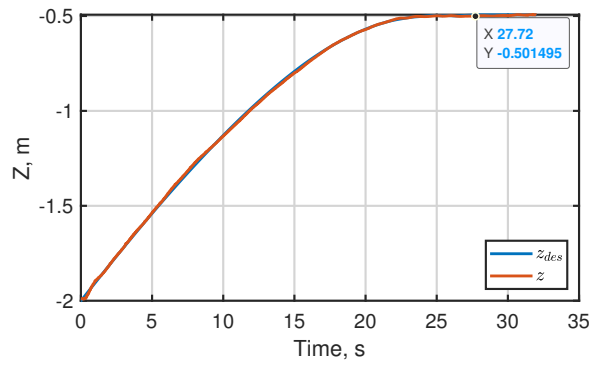
Figure 5.16: Crazyflie trajectory



(a) X component

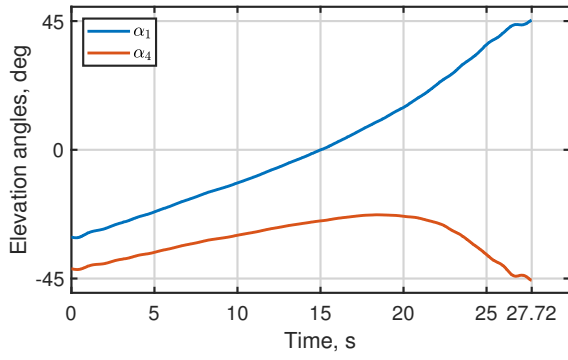


(b) Y component

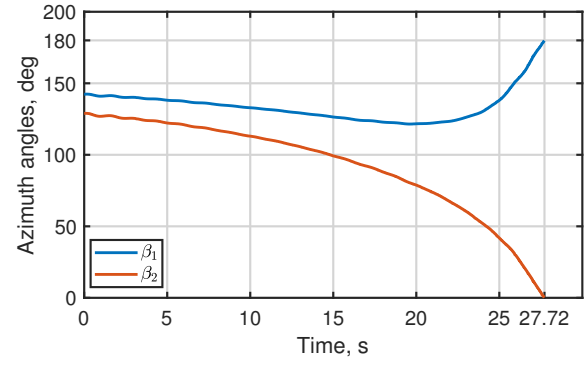


(c) Z component

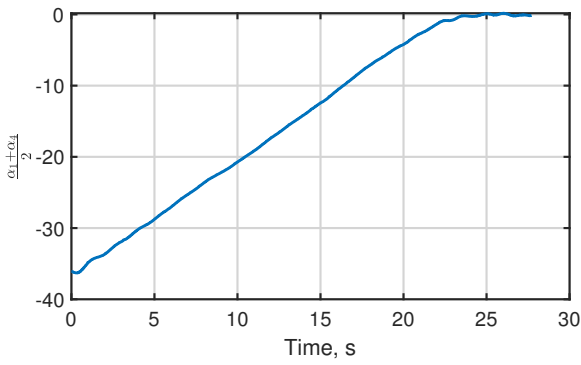
Figure 5.17: Trajectory components



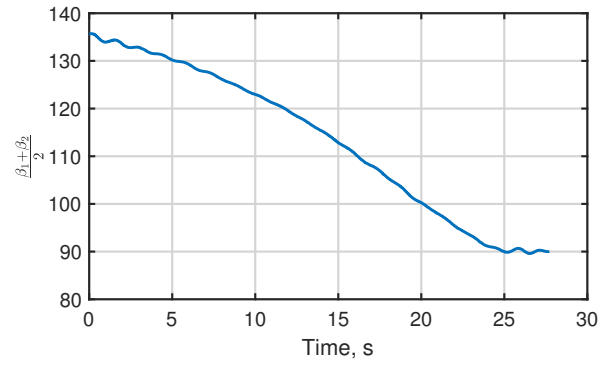
(a) Elevation angles



(b) Azimuth angles



(c) Bisector of elevation angles



(d) Bisector of azimuth angles

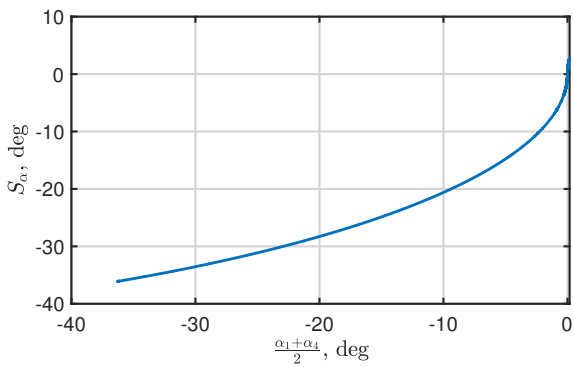
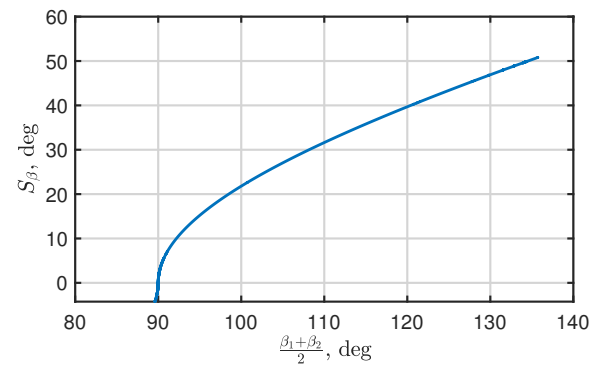
(e) Shaping angle component for γ_{des} (f) Shaping angle component for χ_{des}

Figure 5.18: Angles for guidance computation

5.3 Summary

This chapter considered the hardware setup for the experimental study and flight experiment results for the proposed guidance methods addressed in Chapters 2 and 3. The experiments utilize an indoor motion capture system, and the chapter discusses all the key components involved. The bearing information is obtained through an external motion capture system. The proposed guidance algorithms are implemented on a nano quadrotor using a command and communication center and motion capture system. Two flight experimental trials are presented considering a gap formed by two obstacles and a window. The experimental results highlight the accurate tracking of the proposed guidance commands that were generated.

Chapter 6

Conclusions and Future Work

This thesis explores quadrotor guidance solutions for gap traversal problems using only the relative bearing information. The scenarios encompass planar flight through gaps, three-dimensional traversal through windows, and a lane transition transition scenario employing a moving gap traversal logic within an air corridor system.

Chapter 2 presents a planar guidance method for traversal through a gap formed by two obstacles, relying solely on the bearing information of the gap extremities. The proposed method uses a heading direction as a guidance input to the quadrotor, comprising an elliptic shaping function and a bearing angle bisector. The elliptical shaping profile ensures smooth quadrotor heading relative to the instantaneous bearing angle bisector, guaranteeing safe and lateral traversal through the gap. The guidance input has a simple structure characterized by its reliance on two bearing angles, contributing to its practical applicability. The quadrotor motion is shown asymptotically converge to the gap center line from all initial conditions around the gap. Combined with the tracking controller, the guidance commands are mapped into a 6-DOF quadrotor model through the point object kinematic equation of motion. The numerical simulation results demonstrate the performance of the guidance method in the presence of noisy bearing information and vehicle dynamic constraints. Moreover, the proposed approach is also shown to be robust with respect to various initial conditions and noisy bearing measurements, highlighting its relevance in real-world gap traversal scenarios.

A three-dimensional guidance problem for a window traversal is presented in Chapter 3. By utilizing bearing-only information of window extremities, the proposed guidance logic

governs the commanded flight path and heading angles of the vehicle. These commands incorporate an angular bisector component and an elliptical shaping function, enabling lateral traversal through the window. The shaping angles dynamically vary with respect to the bearing angle bisector, ensuring safe clearance from the window boundaries during the traversal journey. The quadrotor motion asymptotically converges to the line which is normal to the window plane and passes through its centroid. The proposed guidance commands, which are based solely on the three-dimensional bearing angle information of window extremities, are simple, expressed in closed-form, and easy to compute. A comparison with the state-of-the-art methods highlights that, in contrast to either complete prior information of the gap or its depth information, the proposed methods require only the relative bearing information of the gap extremities. The simulation results highlight the effectiveness of the proposed guidance method considering several initial conditions, dynamic limits on attitude angles, and noisy bearing measurements. Additionally, Monte-Carlo studies, which incorporate normally distributed noise in the bearing information, emphasize the robustness of the proposed method. The guidance commands proposed in Chapters 2 and 3 are angular inputs and accordingly they do not inherently impose any speed or acceleration requirements on the vehicle. This makes the methods readily applicable to other vehicles like fixed-wing UAVs and marine vehicles. Moreover, the traversal trajectories are dynamically generated based on instantaneous bearing angles, enabling the flexibility of incorporating updated information as the flight progresses. This improves the robustness of the traversal process, reducing risk of collisions or deviation from the desired traversal path.

Chapter 4 introduces a lane changing guidance framework in an air corridor system containing a service lane and a traffic lane. The proposed lane changing guidance algorithm employs a three-phased guidance logic utilizing bearing information of immediate neighboring vehicles in the traffic lane. The discerning, longitudinal, and transit guidance phases facilitate safe maneuvering through the air corridor. The discerning phase determines the velocity of neighboring vehicles, while the longitudinal phase identifies a suitable gap, and finally, the transit phase directs the quadrotor to the desired gap. Using bearing information, the proposed sinusoidal function-based commanded velocity profiles enable progression through the

guidance phases while ensuring smooth and bounded velocity changes. Further, the quadrotor motion is shown to be asymptotically stable about their desired equilibrium points in each of the three phases. An exact closed-form expression for the time duration is presented for the longitudinal and transit phases, with an approximate time duration obtained analytically for the discerning phase. Accordingly, a desired time duration in each phase can be used as a tool for choosing the guidance gains. Simulation results validate the analytical findings and also present a robustness study under noisy bearing information. In the scenarios where the speed of the vehicles in the traffic lane is known apriori, the proposed method uses only the longitudinal and the transit phases. The proposed lane transit guidance algorithm does not require relative position information of neighboring vehicles and offers a simple and closed-form analytic guidance solution with deterministic performance characteristics.

In Chapter 5, an experiment framework setup is illustrated, which employs an indoor motion capture system and a Crazyflie quadrotor platform. Representative flight trials of the proposed guidance methods addressed in this thesis.

Potential future directions include developing quadrotor guidance methods for gap traversal in the presence of static or moving obstacles and extending the gap traversal scenario to a coordinated traversal of multiple quadrotors. Additionally, addressing three-dimensional lane changing scenarios within air corridor systems, involving multiple transit lanes, is another future work direction.

Bibliography

- [1] S. Bouabdallah, M. Becker, and R. Siegwart, “Autonomous miniature flying robots: Coming soon! - research, development, and results,” *IEEE Robotics Automation Magazine*, vol. 14, no. 3, pp. 88–98, 2007. [1](#)
- [2] S. Spedicato and G. Notarstefano, “Minimum-time trajectory generation for quadrotors in constrained environments,” *IEEE Transactions on Control Systems Technology*, vol. 26, no. 4, pp. 1335–1344, 2018. [1](#)
- [3] H.-Y. Lin and X.-Z. Peng, “Autonomous quadrotor navigation with vision based obstacle avoidance and path planning,” *IEEE Access*, vol. 9, pp. 102450–102459, 2021. [1](#)
- [4] B. Zhao, Y. Tang, C. Wu, and W. Du, “Vision-based tracking control of quadrotor with backstepping sliding mode control,” *IEEE Access*, vol. 6, pp. 72439–72448, 2018.
- [5] S. Jin, J. Zhang, L. Shen, and T. Li, “On-board vision autonomous landing techniques for quadrotor: A survey,” in *2016 35th Chinese Control Conference (CCC)*, pp. 10284–10289, 2016.
- [6] ICRA, “2023 ICRA drone racing competition.” <https://uzh-rpg.github.io/drone-racing-competition>, 2023. [Online]. [1](#)
- [7] Y. Ma, S. Soatto, J. Kosecka, and S. S. Sastry, *An Invitation to 3-D Vision: From Images to Geometric Models*. SpringerVerlag, 2003. [1](#)
- [8] P. Zarchan, “Tactical and strategic missile guidance. 6th ed,” *Progress in Astronautics and Aeronautics*, vol. 157, pp. 107–134, 01 2002. [2](#)

- [9] F. W. Nesline and P. Zarchan, "Line-of-sight reconstruction for faster homing guidance," *Journal of Guidance, Control, and Dynamics*, vol. 8, no. 1, pp. 3–8, 1985.
- [10] P. Zarchan, "Proportional navigation and weaving targets," *Journal of Guidance, Control, and Dynamics*, vol. 18, no. 5, pp. 969–974, 1995.
- [11] A. Ratnoo, "Nonswitching guidance law for trajectory shaping control," *Journal of Guidance, Control, and Dynamics*, vol. 40, no. 10, pp. 2721–2728, 2017.
- [12] K. S. Erer, R. Tekin, and M. K. Özgören, "Biased proportional navigation with exponentially decaying error for impact angle control and path following," in *2016 24th Mediterranean Conference on Control and Automation (MED)*, pp. 238–243, 2016. [2](#)
- [13] M. Clark, Z. Kern, and R. J. Prazenica, "A vision-based proportional navigation guidance law for uas sense and avoid," in *AIAA Guidance, Navigation, and Control Conference*, AIAA 2015-0074, Jan. 2015. [2](#)
- [14] M. Clark and R. J. Prazenica, "Proportional navigation based guidance laws for uav obstacle avoidance in complex urban environments," in *AIAA Information Systems-AIAA Infotech @ Aerospace*, AIAA paper-2017-0672, Jan. 2017. [2](#), [11](#)
- [15] M. H. Trinh, K.-K. Oh, and H.-S. Ahn, "Control of a mobile agent using only bearing measurements in triangular region," in *the 2014 Seventh IEEE Symposium on Computational Intelligence for Security and Defense Applications (CISDA)*, pp. 1–5, 2014. [2](#)
- [16] M. Trinh, G.-H. Ko, V. Pham, K.-K. Oh, and H.-S. Ahn, "Guidance using bearing-only measurements with three beacons in the plane," *Control Engineering Practice*, vol. 51, pp. 81–91, 06 2016. [2](#)
- [17] S. Suresh and A. Ratnoo, "Wall-following guidance using multiple sequential line-of-sight information," *Journal of Guidance, Control, and Dynamics*, vol. 43, no. 5, pp. 1009–1019, 2020. [2](#)

- [18] J. Erskine, R. Balderas-Hill, I. Fantoni, and A. Chriette, "Model predictive control for dynamic quadrotor bearing formations," in *2021 IEEE International Conference on Robotics and Automation (ICRA)*, pp. 124–130, 2021. [2](#)
- [19] Q. Lin, Z. Miao, Y. Wang, J. Lin, and H. Zhong, "Differentiator-based formation control of quadrotors with bearing-only measurements," in *2022 37th Youth Academic Annual Conference of Chinese Association of Automation (YAC)*, pp. 121–126, 2022. [2](#)
- [20] J. Li, Z. Ning, S. He, C.-H. Lee, and S. Zhao, "Three-dimensional bearing-only target following via observability-enhanced helical guidance," *IEEE Transactions on Robotics*, vol. 39, no. 2, pp. 1509–1526, 2023. [2](#)
- [21] D. Mellinger, N. Michael, and V. Kumar, "Trajectory generation and control for precise aggressive maneuvers with quadrotors," *The International Journal of Robotics Research*, vol. 31, no. 5, pp. 664–674, 2012. [3](#), [20](#), [22](#), [51](#), [74](#)
- [22] D. Mellinger and V. Kumar, "Minimum snap trajectory generation and control for quadrotors," in *2011 IEEE International Conference on Robotics and Automation*, pp. 2520–2525, 2011. [3](#), [51](#), [88](#)
- [23] S. Upadhyay, A. Richards, and T. Richardson, "Generation of window-traversing flyable trajectories using logistic curve*," in *2020 International Conference on Unmanned Aircraft Systems (ICUAS)*, pp. 59–65, 2020. [3](#), [51](#)
- [24] S. Upadhyay, T. Richardson, and A. Richards, "Generation of dynamically feasible window traversing quadrotor trajectories using logistic curve," *Journal of Intelligent & Robotic Systems*, vol. 105, no. 1, p. 16, 2022. [3](#)
- [25] G. Loianno, C. Brunner, G. McGrath, and V. Kumar, "Estimation, control, and planning for aggressive flight with a small quadrotor with a single camera and imu," *IEEE Robotics and Automation Letters*, vol. 2, no. 2, pp. 404–411, 2017. [3](#)
- [26] D. Falanga, E. Mueggler, M. Faessler, and D. Scaramuzza, "Aggressive quadrotor flight through narrow gaps with onboard sensing and computing using active vision," in *2017*

- IEEE International Conference on Robotics and Automation (ICRA)*, pp. 5774–5781, 2017. [3](#), [4](#), [11](#), [51](#)
- [27] D. Guo and K. K. Leang, “Image-based estimation, planning, and control for high-speed flying through multiple openings,” *The International Journal of Robotics Research*, vol. 39, no. 9, pp. 1122–1137, 2020. [4](#), [51](#)
- [28] K. Mueller, M. Fennel, and G. F. Trommer, “Model predictive control for vision-based quadrotor guidance,” in *2020 IEEE/ION Position, Location and Navigation Symposium (PLANS)*, pp. 50–61, 2020. [4](#)
- [29] K. Mueller, J. Atman, and G. Trommer, “Combination of wide baseline image matching and tracking for autonomous uav approaches to a window,” *Gyroscope and Navigation*, vol. 10, pp. 206–215, 2019. [4](#)
- [30] E. Kaufmann, M. Gehrig, P. Foehn, R. Ranftl, A. Dosovitskiy, V. Koltun, and D. Scaramuzza, “Beauty and the beast: Optimal methods meet learning for drone racing,” in *2019 International Conference on Robotics and Automation (ICRA)*, pp. 690–696, 2019. [4](#)
- [31] S. Jung, S. Hwang, H. Shin, and D. H. Shim, “Perception, guidance, and navigation for indoor autonomous drone racing using deep learning,” *IEEE Robotics and Automation Letters*, vol. 3, no. 3, pp. 2539–2544, 2018. [3](#), [4](#)
- [32] A. Bauranov and J. Rakas, “Designing airspace for urban air mobility: A review of concepts and approaches,” *Progress in Aerospace Sciences*, vol. 125, p. 100726, 2021. [5](#)
- [33] L. A. Tony, A. Ratnoo, and D. Ghose, “Corridrone: Corridors for drones, an adaptive on-demand multi-lane design and testbed,” *arXiv preprint arXiv:2012.01019*, 2020. [5](#)
- [34] L. A. Tony, A. Ratnoo, and D. Ghose, “Lane geometry, compliance levels, and adaptive geo-fencing in corridrone architecture for urban mobility,” in *2021 International Conference on Unmanned Aircraft Systems (ICUAS)*, pp. 1611–1617, 2021.

- [35] D. D. Nguyen and D. Rohacs, "Air traffic management of drones integrated into the smart cities," *32nd Congress of the International Council of Aeronautical Science*, vol. 1, no. 2, p. 3, 2022.
- [36] V. R. Challa, M. Gupta, A. Ratnoo, and D. Ghose, "Multiple lane uav corridor planning for urban mobility system applications," in *2021 International Conference on Unmanned Aircraft Systems (ICUAS)*, pp. 1003–1009, 2021. [5](#)
- [37] M. N. Stevens and E. M. Atkins, "Geofencing in immediate reaches airspace for unmanned aircraft system traffic management," in *2018 AIAA Information Systems-AIAA Infotech@Aerospace*, p. 2140, 2018. [5](#)
- [38] D. Bevly, X. Cao, M. Gordon, G. Ozbilgin, D. Kari, B. Nelson, J. Woodruff, M. Barth, C. Murray, A. Kurt, K. Redmill, and U. Ozguner, "Lane change and merge maneuvers for connected and automated vehicles: A survey," *IEEE Transactions on Intelligent Vehicles*, vol. 1, no. 1, pp. 105–120, 2016. [5](#)
- [39] J. Chen, P. Zhao, T. Mei, and H. Liang, "Lane change path planning based on piecewise bezier curve for autonomous vehicle," in *Proceedings of 2013 IEEE International Conference on Vehicular Electronics and Safety*, pp. 17–22, 2013. [5](#)
- [40] H. Li, Y. Luo, and J. Wu, "Collision-free path planning for intelligent vehicles based on bézier curve," *IEEE Access*, vol. 7, pp. 123334–123340, 2019. [5](#)
- [41] S. Upadhyay and A. Ratnoo, "A point-to-ray framework for generating smooth parallel parking maneuvers," *IEEE Robotics and Automation Letters*, vol. 3, no. 2, pp. 1268–1275, 2018. [5](#)
- [42] Y. R. Sharma and A. Ratnoo, "Designing safe lane-change maneuvers using an explicit path planner," in *2021 IEEE 17th International Conference on Automation Science and Engineering (CASE)*, pp. 1920–1926, 2021. [5](#)

- [43] M. Wang, Z. Wang, S. Paudel, and M. Schwager, "Safe distributed lane change maneuvers for multiple autonomous vehicles using buffered input cells," in *2018 IEEE International Conference on Robotics and Automation (ICRA)*, pp. 4678–4684, 2018. [5](#)
- [44] M. Durali, G. Javid, and A. Kasaiezadeh, "Collision avoidance maneuver for an autonomous vehicle," in *9th IEEE International Workshop on Advanced Motion Control*, pp. 249–254, 2006. [5](#)
- [45] W. Ben-Messaoud, M. Basset, J.-P. Lauffenburger, and R. Orjuela, "Smooth obstacle avoidance path planning for autonomous vehicles," in *2018 IEEE International Conference on Vehicular Electronics and Safety (ICVES)*, pp. 1–6, 2018. [5](#)
- [46] D. Wang, Q. Pan, J. Hu, C. Zhao, and Y. Guo, "Mpcc-based path following control for a quadrotor with collision avoidance guaranteed in constrained environments," in *2019 IEEE 28th International Symposium on Industrial Electronics (ISIE)*, pp. 581–586, 2019. [5](#)
- [47] S. R. Nagraire, L. A. Tony, A. Ratnoo, and D. Ghose, "Multi-lane uav traffic management with path and intersection planning," in *AIAA SCITECH 2022 Forum*, AIAA Paper 2022-1505, Jan. 2022. [5](#), [6](#)
- [48] S. R. Nagraire, A. Ratnoo, and D. Ghose, "Intersection planning for multilane unmanned aerial vehicle traffic management," *Journal of Aerospace Information Systems*, vol. 0, no. 0, pp. 1–18, 0. [5](#), [6](#)
- [49] S. Suzuki and K. be, "Topological structural analysis of digitized binary images by border following," *Computer Vision, Graphics, and Image Processing*, vol. 30, no. 1, pp. 32–46, 1985. [11](#)
- [50] R. W. Beard, "Quadrotor dynamics and control rev 0.1," Dept. Elect. Comput. Eng., Brigham Young Univ., Provo, UT, USA, Tech. Rep. 1325, Feb. 2008. [19](#)
- [51] J. F. Shepherd and K. Tumer, "Robust neuro-control for a micro quadrotor," in *Proceedings of the 12th Annual Conference on Genetic and Evolutionary Computation, GECCO '10*, (New York, NY, USA), p. 1131–1138, Association for Computing Machinery, 2010. [22](#)

- [52] A. Chakravarthy and D. Ghose, “Generalization of the collision cone approach for motion safety in 3-d environments,” *Autonomous Robots*, vol. 32, pp. 243–266, Apr 2012. [33](#)
- [53] A. Chakravarthy and D. Ghose, “Guidance for precision three-dimensional maneuvers through orifices using safe-passage cones,” *Journal of Guidance, Control, and Dynamics*, vol. 39, no. 6, pp. 1325–1341, 2016. [33](#)
- [54] G. Ellis, “Control system design guide. 4th ed.,” *Butterworth-Heinemann*, pp. 165–183, 2012. [78](#)
- [55] W. Giernacki, M. Skwierczyński, W. Witwicki, P. Wroński, and P. Koziński, “Crazyflie 2.0 quadrotor as a platform for research and education in robotics and control engineering,” in *2017 22nd International Conference on Methods and Models in Automation and Robotics (MMAR)*, pp. 37–42, 2017. [82](#)
- [56] G. Silano, E. Aucone, and L. Iannelli, “CrazyS: A software-in-the-loop platform for the crazyflie 2.0 nano-quadcopter,” in *2018 26th Mediterranean Conference on Control and Automation (MED)*, pp. 1–6, 2018.
- [57] F. Candan, A. Beke, and T. Kumbasar, “Design and deployment of fuzzy PID controllers to the nano quadcopter crazyflie 2.0,” in *2018 Innovations in Intelligent Systems and Applications (INISTA)*, pp. 1–6, 2018.
- [58] C. Budaciu, N. Botezatu, M. Kloetzer, and A. Burlacu, “On the evaluation of the crazyflie modular quadcopter system,” in *2019 24th IEEE International Conference on Emerging Technologies and Factory Automation (ETFA)*, pp. 1189–1195, 2019. [82](#)
- [59] Bitcraze, “Bitcraze Official Website.” Bitcraze, 2023. [83](#)
- [60] OptiTrack, “OptiTrack Official Website.” OptiTrack, 2023. [85](#)